GEOLOGICA ULTRAIECTINA

Mededeling van de
Faculteit Geowetenschappen
Universiteit Utrecht

No. 299

The upper mantle beneath the Gulf of California from surface wave dispersion

Xiaomei Zhang

The research described in this thesis was carried out at:
Faculty of Geosciences
Vening Meinesz Research School of Geodynamics
Utrecht University
Budapestlaan 4
3584 CD Utrecht
The Netherlands

http://www.geo.uu.nl/Research/Seismology/

Printed by Wöhrmann Print Service, Zutphen
ISBN: 978-90-5744-163-9

The upper mantle beneath the Gulf of California from surface wave dispersion

De bovenmantel onder de Golf van Californië door dispersiemetingen van oppervlaktegolven

(met een samenvatting in het Nederlands)

PROEFSCHRIFT

TER VERKRIJGING VAN DE GRAAD VAN DOCTOR
AAN DE UNIVERSITEIT UTRECHT
OP GEZAG VAN DE RECTOR MAGNIFICUS, PROF. DR. J.C. STOOF,
INGEVOLGE HET BESLUIT VAN HET COLLEGE VOOR PROMOTIES
IN HET OPENBAAR TE VERDEDIGEN
OP VRIJDAG 9 JANUARI 2009 DES MIDDAGS TE 12:45 UUR

DOOR

Xiaomei Zhang

geboren op 1 januari 1974, te Ningxia, China

Promotor:	Prof. Dr. J. Trampert
Co-promotor:	Dr. H. Paulssen

燁燁震電，不寧不令。

百川沸騰，山冢崒崩。

高岸爲谷，深谷爲陵。

节自《诗经·小雅》

Grandly flashes the lightning of the thunder,
There is a want of rest, a want of good.
The streams all bubble up and overflow.
The crags on the hill-tops fall down.
High banks become valleys;
Deep valleys become hills.

Book of Odes, 780 BC

Members of the dissertation committee:

Prof. Dr. A. Morelli
Sezione di Bologna
Istituto Nazionale di Geofisica e Vulcanologia, Italy

Prof. Dr. M. J. R. Wortel
Faculty of Geosciences
Utrecht University, The Netherlands

Prof. Dr. J. Ritsema
Division of Geological and Planetary Sciences
California Institute of Technology, USA

Prof. Dr. R. W. Clayton
Division of Geological and Planetary Sciences
California Institute of Technology, USA

Dr. J. Gaherty
Lamont-Doherty Earth Observatory
Columbia University, USA

Contents

Chapter 1

Introduction

This thesis is a study on upper mantle shear velocity structure beneath the Gulf of California. Surface wave interstation dispersion data were measured in the Gulf of California area and vicinity to obtain a 3 dimensional (3D) shear velocity structure of the upper mantle. This work has particular significance for understanding the tectonic evolution history in this region and the potential processes that control lithospheric rupture and the initiation of seafloor spreading in the Gulf of California.

1.1 Tectonic background

The Gulf of California (GofC), or Sea of Cortez, is an arm of the Pacific about 100–150 km wide between the Mexican mainland and the 1200-km-long peninsula of Baja California. The water body in the gulf conceals an active plate boundary system in the middle of the gulf on the seafloor. It holds en échelon basins connected by long transform faults, and links the San Andreas strike-slip fault system in California in the North to the oceanic spreading system of the East Pacific Rise in the South. Together, the San Andreas strike-slip fault system, the GofC and the East Pacific Rise form the Pacific-North American plate boundary.

The young and active plate boundary development in the GofC is a result of tectonic interaction between the Pacific, Farallon and North American plates (e.g., Atwater, 1970; Lonsdale, 1991; Atwater and Stock, 1998). Prior to 30 million years ago (Ma), the Farallon plate, a huge oceanic plate, named after the Farallon Islands offshore California, existed between the Pacific and North American plates. The Farallon plate moved away from the Pacific plate at the Pacific-Farallon spreading ridge on its western border. Meanwhile, at its eastern border,

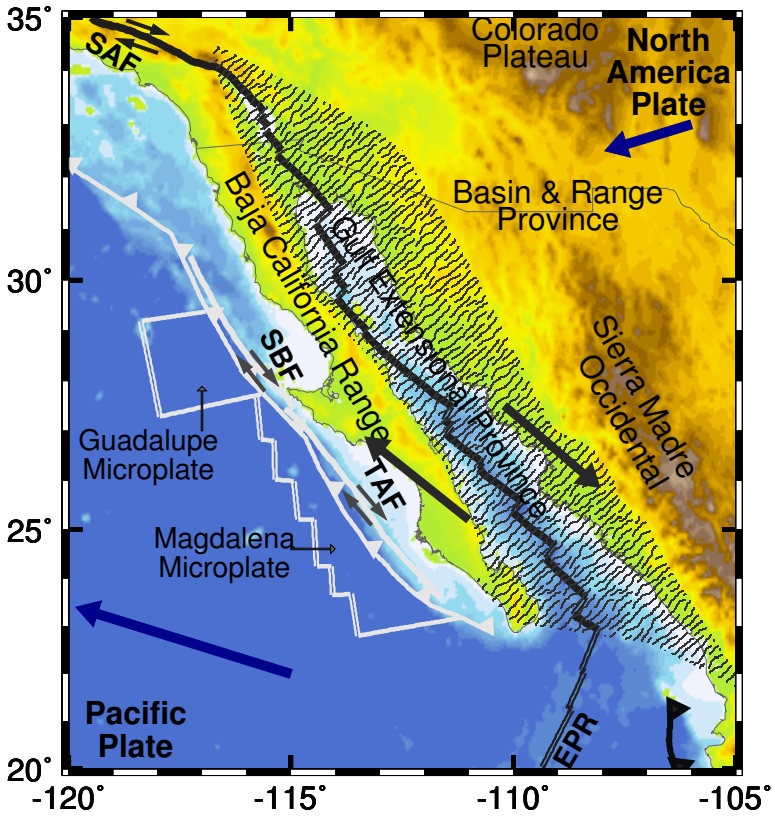

Figure 1.1.1: Tectonic map of the Gulf of California region. The main tectonic provinces are Baja California Range, Gulf Extensional Province (hatched), Basin and Range Province, Sierra Madre Occidental and Colorado Plateau. Present-day plate boundaries shown as dark lines. Inactive plate boundaries shown as white lines. SAF−San Andreas Fault; EPR−East Pacific Rise; SBF−San Benito Fault; TAF−Tosco Abreojos Fault. Thick arrows indicate plate motions (absolute plate motion in blue, relative plate motion in black) predicted by global plate motion model HS3-NUVEL1A (Gripp and Gordon, 2002).

it subducted under the North American plate at the western edge of the continent. The half-spreading rate at the Pacific-Farallon spreading ridge could not keep pace with the Farallon-North American subduction rate. Therefore, the Pacific-Farallon spreading ridge eventually reached the trench at the subduction zone at ca. 28 Ma. As a consequence, the Pacific plate made direct contact with the North American plate and two triple junctions formed: a transform-transform-trench triple junction, the Mendocino triple junction, which migrated to the Northwest, and a

ridge-transform-trench triple junction, the Rivera triple junction, which moved to the Southeast. Between the two triple junctions, the character of the plate boundary changed from Farallon-North American oblique subduction to Pacific-North American transcurrent motion with an extensional component taken up by the North-American continent (e.g., Lonsdale, 1991; Furlong, 1993; Nicholson et al., 1994; Bohannon and Parsons, 1995). A slab window, an area without slab between these two triple junctions, was formed beneath western North America (Dickinson and Snyder, 1979a; Severinghaus and Atwater, 1990; Atwater and Stock, 1998).

With time the Rivera triple junction migrated southward and the intervening Farallon plate continuously fragmented into various microplates. Two of these microplates, the Guadalupe and the Magdalena, have been identified offshore west Baja Peninsula (Figure 1.1.1). Their subduction beneath Baja California ceased ca. 12 Ma. The Pacific-North American plate motion was then largely accommodated along the right-lateral San Benito and Tosco-Abreojos fault zones parallel to the fossil trench. The extensional component of the motion was taken up by back-arc extension, forming a proto-gulf between two more rigid blocks, the Baja California Range to the west and the Sierra Madre Occidental to the east. Over time the relative plate motion was increasingly accommodated by strike-slip motion and extension in the proto-gulf area. Thus, it was to become the Gulf Extensional Province. At approximately 6 Ma, most of the Pacific-North American transform motion along the San Benito and Tosco-Abreojos faults ended, moved inland, and was accommodated in the proto-gulf area along transform faults and pull-apart basins (e.g., Lonsdale, 1991; Oskin and Stock, 2003). Consequently, oceanic spreading started to develop, the GofC started to open, and the Baja peninsula was captured by the Pacific plate. At present, approximately 90% of the Pacific-North American plate motion (51 mm/yr) is taken up by the Northwest extension in the gulf (Plattner et al., 2007).

The GofC is currently extending by rifting. As a transition between the East Pacific Rise and the San Andreas transform fault system, the plate boundary in the GofC changes character from an oceanic-type spreading centre and transform fault system in the South to a region of diffuse continental extensional deformation in the North (Nagy and Stock, 2000; González-Fernández et al., 2005; Lizarralde et al., 2007). It is still unclear what causes the differences in the style of rifting between the southern part and the northern part. These variations cannot be explained by variations in the amount of deformation: the South and North have experienced roughly the same amount ($\sim$300 km) of oblique Northwest-Southeast extension since the opening of the gulf at about 6 Ma (Persaud et al., 2003). Moreover, seismic refraction experiments have revealed that basins in the south-

ern and central gulf vary from wide to narrow rifts over small distances (∼200 km) (Lizarralde et al., 2007). Both the North - South variation and the style of rifting change in the southern and central gulf, make the GofC an especially interesting region for studying the evolution of a rift.

The magmatism in Baja California and the GofC reflects the tectonic history of the region as well. The Baja Peninsular Range, which was formed approximately between 24 and 11 Ma as a subduction-related calc-alkaline volcanic arc. It forms a large part of the current Baja California peninsula. The cessation of Guadalupe and Magdalena microplate subduction at 12 Ma is reflected in the changes of magmatism in Baja. The calc-alkaline arc volcanism in central and southern Baja California changed to other types of volcanism in various volcanic fields. A few unusual magma types started to appear in the former arc volcanic fields, such as: adakites, derived from partial melting of subducted oceanic crust, magnesian andesites, from a mantle metasomatized by slab-derived melts, and tholeiitic basalts without a strong subduction signature. Tholeiitic magmas have been erupting in the GofC since the initiation of rifting at ca. 12 Ma. The geochemical signature in these volcanic rocks ranges from a typical intraplate setting (similar to ocean island basalts and continental flood basalts) to those typical of mature oceanic rifting (mid-ocean ridge basalts). The type of volcanic rock depends on its location and the stage of rifting at the time of eruption (Sawlan, 1991; Conly et al., 2005; Bellon et al., 2006; Pallares et al., 2007).

The geology and magmatism provide evidence for a complex tectonic history. However, without the knowledge of the mantle, we can not reconstruct the tectonic evolution in time and space.

1.2 The NARS-Baja project

Previous global and regional studies on upper mantle structure have shown noticeably lower than average shear wave velocities in the upper 250 km of the mantle beneath the GofC area (e.g., Lebedev and van der Hilst, 2008; Merrer et al., 2007; van der Lee and Frederiksen, 2005; Godey et al., 2003; Grand, 1994; Walck, 1984). However, because the resolution of these tomographic images ($\sim$ 1000km) is insufficient, we need higher resolution ($\sim$ 100km) upper mantle images to better understand the tectonics.

The poor resolution in the previous tomographic studies was due to a lack of seismic stations in this region. The permanent seismic networks in the area are primarily located in southern California and southern Mexico. The NARS-Baja project, which was established in 2002, bridges this station gap (Figure 1.2.1)

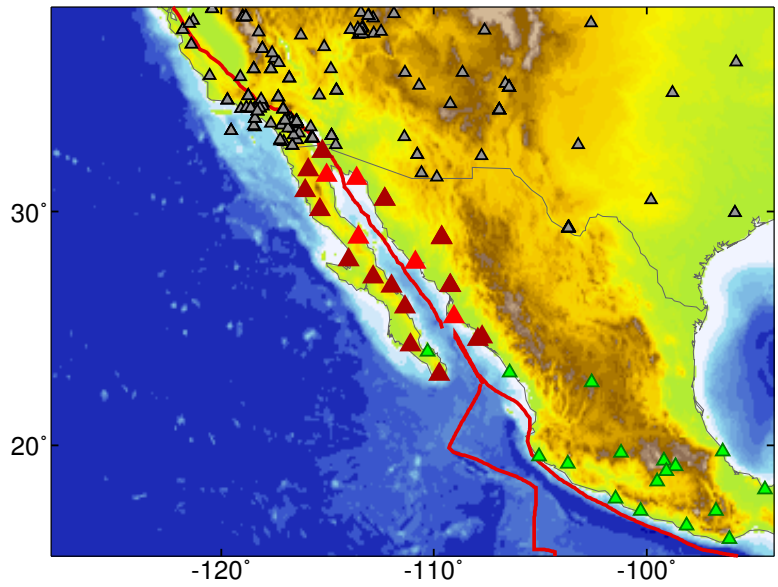

Figure 1.2.1: The GofC and the NARS-Baja project. The NARS-Baja stations are depicted by red triangles. The U.S. stations are in gray. The Mexico stations are in green. The plate boundaries are shown as red lines (adopted from Trampert et al. (2003)).

and provides a new dataset and a unique opportunity to determine some basic lithospheric and asthenospheric properties on a regional scale around the entire Gulf (Trampert et al., 2003). The NARS-Baja project is a collaboration between Utrecht University, CICESE (Centro de Investigación Científica y de Educación Superior de Ensenada, Mexico) and Caltech (California Institute of Technology, U.S.). It is a 19-station broadband seismic deployment in Baja and along the Sonora and Sinaloa coasts.

NARS-Baja array is a joined project involving two networks. NARS, the Network of Autonomously Recording Seismographs (NR), is a mobile seismic network (contributes 14 mobile, broadband stations) operated by the seismology group of the Department of Earth Sciences, Utrecht University, The Netherlands. RESBAN, the Red Sísmica de Banda Ancha network (RB), contributes 5 broadband stations operated by the Mexican institute CICESE located at Ensenada. The NARS-Baja experiment provided a broad station coverage in the GofC region for a 6-year period. The broadband seismic data are freely available from the IRIS Data Management Centre in Seattle and the SCEC Data Centre at Caltech. NARS-Baja data allows us to make models of the crust and mantle with an unprecedented resolution. The models will provide new constraints on the nature of this young

plate boundary.

1.3 Previous studies with NARS-Baja data

Understanding the evolution of the GofC requires knowledge of the underlying mantle. Mantle temperature and composition control crustal extension through their effects both on flow in the mantle and crust and on magmatism. Seismic studies revealed anomalously low mantle shear velocities down to 250 km depth in the entire GofC area. Lack of seismic stations in the area, however, has precluded resolution at the scale comparable to that of the observed variations in the style of rifting and magmatism.

A few studies have already benefited from the data of the NARS-Baja project. Persaud et al. (2007) have mapped the crustal thickness under the NARS-Baja stations through a receiver function study. They revealed that the crustal thickness under the NARS-Baja stations ranges from 21 to 37 km with an approximately W−E thinning trend along the Baja California peninsula. López-Pineda et al. (2007) have given 3 transects of the crustal shear wave structure by studying short period ($10 \sim 40$ s) surface waves. The Moho depths under the NARS-Baja stations in this study, however, are often deeper than those from Persaud et al. (2007) and do not show the W-E thinning trend. Obrebski et al. (2006) and van Benthem et al. (2008) have studied anisotropy in the upper mantle by using SKS splitting measurements under the NARS-Baja network and a few Mexican stations. They found a North - South variation in the shear wave splitting parameters under stations on the Baja peninsula. The stations on the northern and the very southern tip of the peninsula have a roughly E-W fast direction, whereas small delay times and null measurements are dominant in the central and southern part of the peninsula. As on the Mexican mainland, most of the SKS fast directions show agreement with the absolute motion of the North American plate. Obrebski and Castro (2008) have presented anisotropic lithospheric models beneath 3 NARS stations from a receiver function analysis. They obtained different anisotropic models beneath station NE71, NE75 and NE81 (see Fig. 2.1.1) . Although a number of studies has been carried out using the NARS-Baja data, these studies did not achieve a detailed 3D mantle image. However, a detailed upper mantle structure is crucial for certain mantle related questions (e.g., Furlong, 1993). e.g. How does the slab window extend beneath the GofC? Is there still a slab remnant in the upper mantle? Is there any link between the North-South variation in style of rifting in the gulf and upper mantle velocity variation? In this work, we aimed to reconstruct a 3D radial anisotropic velocity model of the GofC by using both

Rayleigh and Love wave dispersion data. The constraints on flow can reveal the mantle structure and flow pattern and provide insight into the tectonic evolution.

1.4 Thesis overview

In this study we present a seismic shear wave velocity model of the upper mantle (0∼300km) beneath the GofC and surrounding regions from a surface wave study. The introductory chapter, Chapter 1, contains an overview of the tectonic history of the GofC, the NARS-Baja project and some previous studies in this region. The method and data used in this study were described in Chapter 2. The main result of this study can be found in Chapters 3–5. In Chapter 3, the fundamental mode Rayleigh wave phase velocity structure with azimuthal anisotropy obtained from NARS-Baja data is presented. In Chapter 4, we enlarged the study area and inverted the fundamental mode Rayleigh wave phase velocity structure for a 3D SV model. In Chapter 5, both Love and Rayleigh measurements are inverted to obtain a 3D shear velocity model with radial anisotropy. The last chapter, Chapter 6, contains a brief summary and the general conclusion of this study.

Chapter 2

Method and data

Seismic surface waves are well suited for exploring the upper mantle structure. Their speed of propagation is a function of frequency, because the penetration depth depends on frequency. Measuring dispersion gives us therefore information on the structure as a function of depth. In this chapter, the data set and methods used to obtain fundamental mode Rayleigh and Love phase velocity measurements, with their uncertainties, are explained. Furthermore, resolution related issues concerning the phase and shear wave velocity inversion are discussed.

2.1 Data

This study is based on interstation phase velocity measurements. For two stations located on the same great circle as the event, the phase difference between them is due mainly to the structure along the path. In order to explore the upper mantle structure in the GofC, interstation fundamental mode phase velocities were measured in the GofC area and its vicinity, and the data were subsequently inverted for shear velocity structure. Our main interest is to understand the links between the upper mantle structure and variations in the style of rifting in the gulf. The contribution of data from the NARS-Baja array was essential in this study. We used data from six other networks for the construction of the SV model in order to enlarge the research area. This was done for two reasons: firstly, we could test the robustness of our approach by comparing our results with other studies in Southern California, especially the ones using a different approach in imaging upper mantle structure; secondly, it allowed us to image the structure of the gulf in a larger regional context. The stations of the other broadband seismic networks are located in Southern California, Nevada, New Mexico and Texas in the

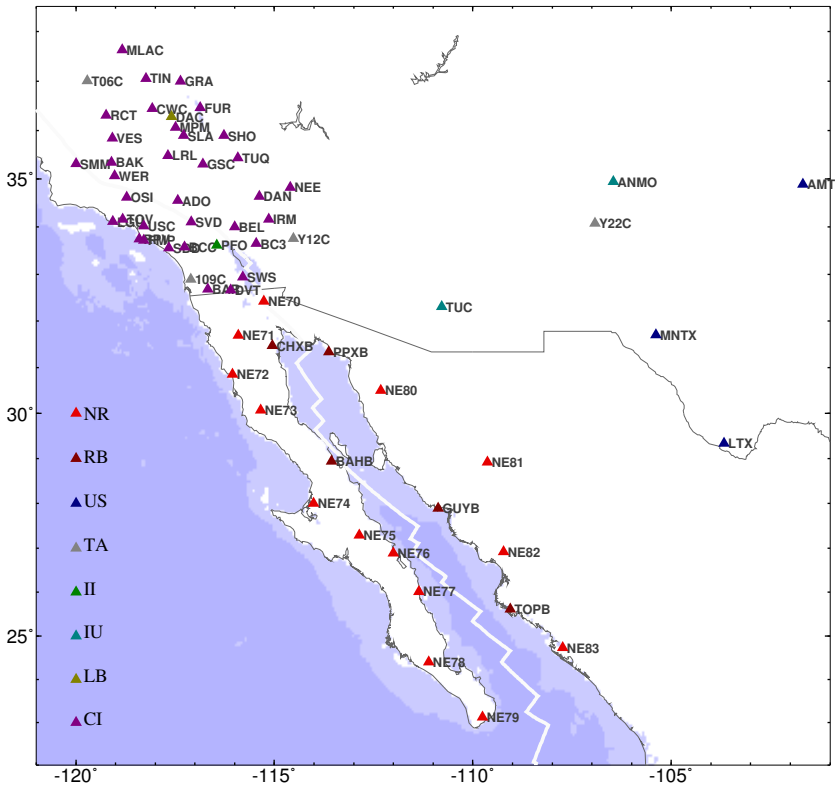

Figure 2.1.1: The stations used in this study.

USA (Figure 2.1.1). They are obtained from: (1) The Caltech Regional Seismic Network(CI) from California Institute of Technology; (2) IRIS/IDA Network(II) from University of California, Scripps Institute of Oceanography; (3) IRIS/USGS Network(IU) from USGS Albuquerque Seismological Laboratory; (4) Leo Brady Network (LB) from Sandia National Laboratory; (5) USArray Transportable Array (TA) from Earthscope Project; (6) US National Seismic Network (US) from ANSS Backbone of the USGS/NEIC and USGS/ASL and Earthscope Project of IRIS. The station information is listed in appendix A.

The NARS-Baja array (Figure 2.1.1) is within teleseismic distance of a large percentage of Earth's seismicity, that is to say, the circum-Pacific seismic belt provides abundant seismicity which provides a good azimuthal coverage required in our study. More than one thousand seismic events with minimum moment magnitude (Mw) of 5.0, occurring between April 2002 and the end of 2005, were used

in this study. From these, up to ten thousand vertical component seismograms recorded at 64 broadband stations in the vicinity of the GofC (Figure 2.1.1) contributed to the study of the SV model. More than two thousand transverse component seismograms recorded at the NARS-Baja array were used for the study of radial anisotropy and the SH model. More detailed information about the data distributions for each of the studies can be found in the following three chapters.

2.2 The two-station method

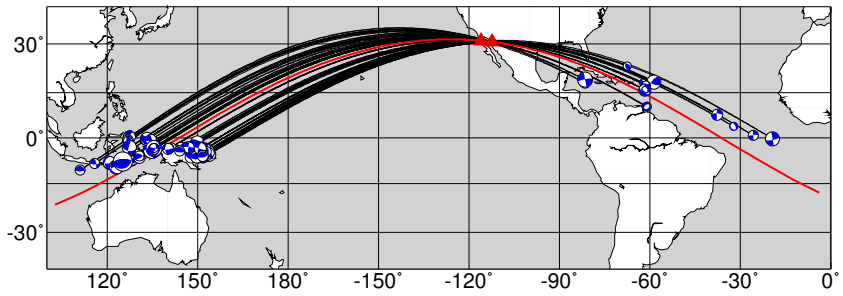

Figure 2.2.1: The events used for the phase velocity determination between stations NE72-NE80. Beach balls indicate the source mechanisms of the events. The red line indicates the great-circle connecting the two stations. Black lines depict the great-circle paths between the epicentres and these two stations.

The two-station method in the frequency domain was first introduced by Sato (1955). Since then it has been extensively used to determine surface wave dispersion curves (a review of early works can be found in Knopoff (1972)). From the cross-correlation function of two vertical (or transverse) component seismograms, excited by the same event recorded at two stations with the same back azimuth, one can find the phase velocity c at frequency ω

$$c(\omega) \quad = \quad \frac{\omega(\Delta_1 - \Delta_2)}{arctan\left\{\Im[\Phi(\omega)]/\Re[\Phi(\omega)]\right\} + 2n\pi}, \tag{2.2.1}$$

where $\Phi(\omega)$ is the cross-correlation function of the two seismograms at frequency ω, $\Re[\Phi(\omega)]$ and $\Im[\Phi(\omega)]$ are the real and imaginary components of $\Phi(\omega)$ respectively. Δ_1 and Δ_2 are the epicentral distances and the indices 1 and 2 refer to the two stations. Because of the $2\pi-$ambiguity of the arctan function, the phase velocity is estimated from an array of curves for different values of n, where n belongs to the ensemble of integers.

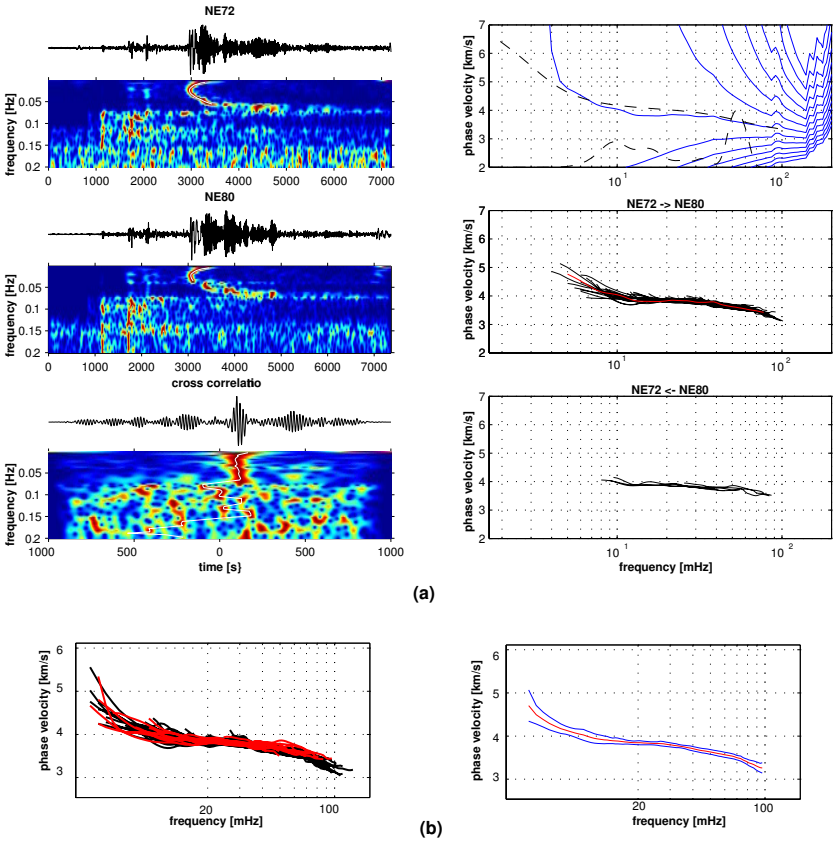

Figure 2.2.2: The determination of the fundamental mode Rayleigh wave phase velocity between the stations NE72 and NE80 by the two-station method. (a) Phase velocity determination per event: the left 3 panels show the waveforms at the two stations and their cross-correlation function in time and frequency domain calculated by the multiple filter technique (MFT). The solid white lines in the time-frequency representations are automatically determined group travel times. The upper right panel shows the phase velocity selection for this event: the solid blue lines indicate the array of phase velocity curves obtained from the cross-correlation function. The dashed curves in the upper right plot indicate the normalized amplitude spectrum of the cross-correlation function and the reference phase velocity for an initial model. The interactively selected phase velocity curve is shown in the middle right panel in red. The black lines in the middle right panel show phase velocity curves obtained from other events. The lower right panel shows phase velocities curves from the opposite propagation direction. (b) Left panel shows the ensemble of all picked phase velocity curves for this path, black lines depict the direction from NE72 to NE80, red lines depict the opposite direction. Right panel shows the mean phase velocity curve (in red) and its standard deviation (in blue) for this path.

In this study, we follow the approach of Meier et al. (2004), measuring phase velocities of fundamental Rayleigh and Love wave by cross-correlating vertical- and transverse-component seismograms from the two stations, respectively. Figure 2.2.1 and Figure 2.2.2 illustrate the determination of the phase velocity for the path between the stations NE72 and NE80 across the gulf. Figure 2.2.1 depicts the events used for the phase velocity determination between this station pair. Events are only considered if the angle between the great circle connecting the two stations and the great circle through the stations and the epicentre is smaller than 7°. The cross-correlation function is first filtered with a frequency-dependent Gaussian bandpass filter, and then it is windowed in the time domain with a frequency-dependent Gaussian window centred on the maximum amplitude of the cross-correlation function. The side lobes in the cross-correlation function, due to noise and the interaction between the fundamental mode and higher modes of the waveform, are then suppressed. The phase velocity $c(\omega)$ is calculated in the frequency domain from the cross-correlation function. Because of the $2\pi-$ambiguity of the arctan function, the phase of the cross-correlation is not unique. Therefore in the next step, the reliable part of the phase velocity curve (which is smooth and close to the reference value) is interactively selected in the frequency domain. This process is repeated for all the events. The final dispersion curve is obtained as the average of all the phase velocity curves; its error bars are $\pm$ one standard deviation of the ensemble of dispersion curves. The two-station method is very powerful for producing measurements in a broad period range, but it is time consuming.

2.3 The automated multimode inversion

The automated multimode inversion (AMI) by Lebedev et al. (2005) is adopted here to obtain additional interstation phase velocity measurements. The main reason for introducing this second method was that AMI is highly automated. It is fast and therefore gives us the ability to enlarge the research area.

AMI is a waveform inversion technique based on mode summation that fits those parts of the seismograms which have a high signal to noise ratio. Under the Jeffreys-Wentzel-Kramers-Brillouin (JWKB) approximation, a synthetic seismogram can be calculated as a sum of modes m in the frequency domain (e.g. Dahlen and Tromp, 1998):

$$s(\omega) \quad = \quad \sum_m A_m(\omega) exp[i\omega\Delta/c_m(\omega)], \tag{2.3.1}$$

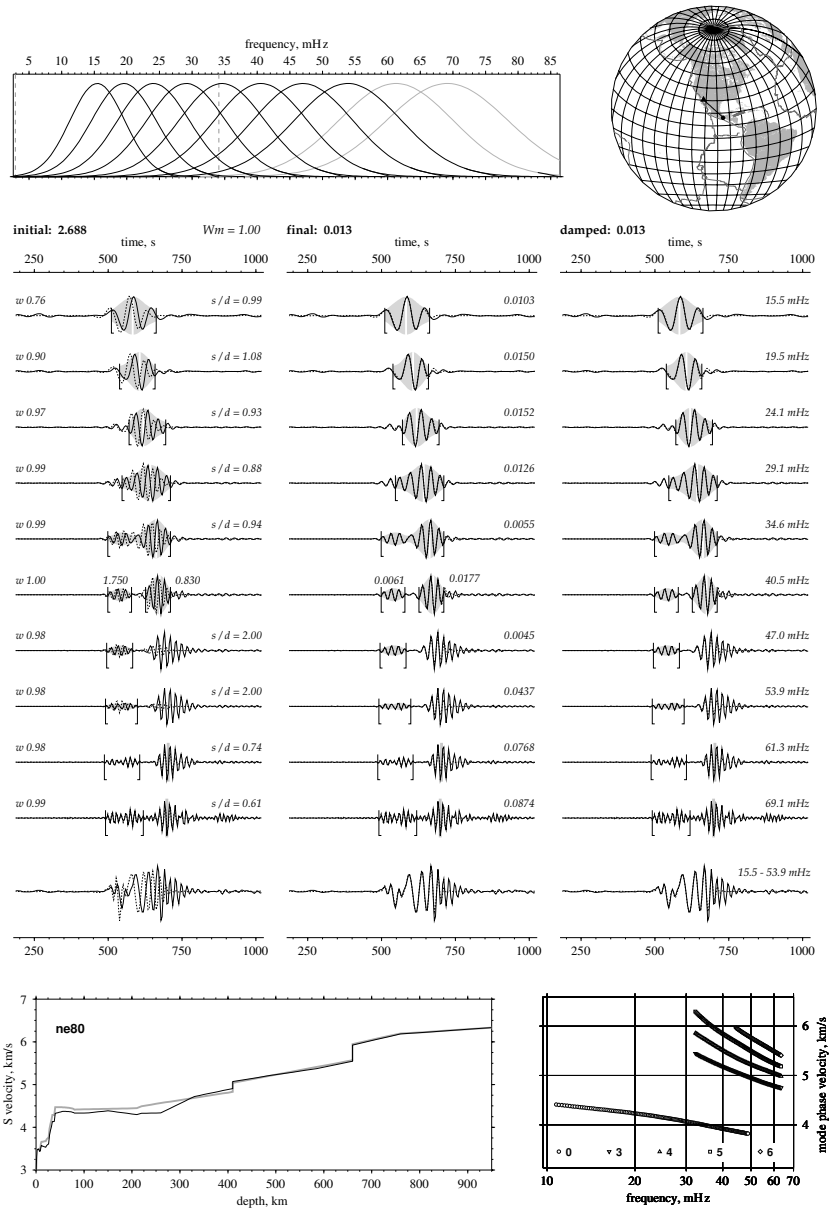
frequency, mHz
5 10 15 20 25 30 35 40 45 50 55 60 65 70 75 80 85
initial: 2.688
Wm = 1.00
final: 0.013
damped: 0.013
time, s
250 500 750 1000
w 0.76
s / d = 0.99
0.0103
15.5 mHz
w 0.90
s / d = 1.08
0.0150
19.5 mHz
w 0.97
s / d = 0.93
0.0152
24.1 mHz
w 0.99
s / d = 0.88
0.0126
29.1 mHz
w 0.99
s / d = 0.94
0.0055
34.6 mHz
w 1.00
1.750
0.830
0.0061
0.0177
40.5 mHz
w 0.98
s / d = 2.00
0.0045
47.0 mHz
w 0.98
s / d = 2.00
0.0437
53.9 mHz
w 0.98
s / d = 0.74
0.0768
61.3 mHz
w 0.99
s / d = 0.61
0.0874
69.1 mHz
15.5 - 53.9 mHz

ne80
S velocity, km/s
depth, km
0 100 200 300 400 500 600 700 800 900
3 4 5 6 7

mode phase velocity, km/s
frequency, mHz
10 20 30 40 50 60 70
4 5 6
0 3 4 5 6

Figure 2.3.1: An example of the waveform inversion procedure by AMI. The upper left panel shows the band-pass filters applied to this trace. The upper right panel shows the event and the NARS station that produced the recording. Waveform fits for a path-average 1-D model before the inversion (initial fit) and after the waveform inversion (final), and the fit predicted by the 1-D damped model. The centre frequencies of the filters are specified next to the waveforms in the first column. The recorded signal is drawn with a solid line, and the synthetics are drawn with a dashed line. Envelopes of the fitted data traces are shaded gray; the maxima of the fundamental mode envelopes are marked with white vertical lines. Half brackets denote the time windows selected for each filtered waveform. The values of the misfit in each window are shown next to the windows in the two columns on the right. The lower left panel shows the inverted 1D shear velocity model, the initial model is in gray and final model is black. The Love wave phase velocities are shown in the lower right panel.

where $A_m(\omega)$ is the complex amplitude of the modes, Δ is the source-receiver distance and $c_m(\omega)$ is the phase velocity of mode m. To first order,

$$s(\omega) = \sum_m A_m(\omega) exp[i\omega\Delta/(c_m^0(\omega) + \delta c_m(\omega))]. \tag{2.3.2}$$

where $c_m^0(\omega)$ is the phase velocity of the reference model and $\delta c_m(\omega)$ is the first order phase velocity perturbation defined as

$$\begin{aligned}\delta c_m(\omega) = \frac{1}{a}\int_0^a (&\frac{\partial c_m^0(\omega)}{\partial V_p(r)}\delta V_p(r) + \frac{\partial c_m^0(\omega)}{\partial V_s(r)}\delta V_s(r) \\ &+ \frac{\partial c_m^0(\omega)}{\partial \rho(r)}\delta\rho(r))dr,\end{aligned} \tag{2.3.3}$$

where a is the earth radius. If we scale the compressional wave velocity $V_p(r)$ and the density $\rho(r)$ to $V_s(r)$, then this expression is simplified as

$$\delta c_m(\omega) = \int_0^a k_m(r,\omega)\delta V_s(r)dr, \tag{2.3.4}$$

where $k_m(r,\omega)$ is the kernel, defined as

$$k_m(r,\omega) = \frac{1}{a}(\frac{\partial c_m^0(\omega)}{\partial V_s(r)} + \alpha(r)\frac{\partial c_m^0(\omega)}{\partial V_p(r)} + \beta(r)\frac{\partial c_m^0(\omega)}{\partial \rho(r)}). \tag{2.3.5}$$

$\alpha(r)$ and $\beta(r)$ are the known scaling factors. AMI parameterises the shear-velocity perturbations $\delta V_s(r)$ as a set of one-dimensional basis functions $h_i(r)$

(details can be found in Nolet (1990)):

$$\delta V_s(r) = \sum_{i=1}^{N} \gamma_i h_i(r), \tag{2.3.6}$$

where γ_i are the coefficients to be found in the waveform inversion. If we combine the equations above, then

$$\delta c_m(\omega) = \sum_{i=1}^{N} \gamma_i \int_0^a k_m(r,\omega) h_i(r) dr. \tag{2.3.7}$$

Now, we obtain a set of linear equations that links the phase velocity perturbations to the shear velocity perturbations. Lebedev et al. (2005) designed a set of time- and frequency-dependent weightings to fit different portions of high signal-to-noise ratio seismograms automatically. This allows a fully automated waveform inversion. Figure 2.3.1 illustrates the AMI waveform inversion procedure. The transverse component seismogram is recorded at station NE80 and excited by a Mw 5.8 earthquake located in Oaxaca, Mexico. Thanks to the relatively large event depth (78 km), not only the fundamental mode but also a few higher modes could be fitted in this case. The background (initial) model for the waveform inversion is built through a two step procedure: first it averages the crustal structure of crust2.0 (Bassin et al., 2000) between the event and the receiver, and then this average crustal model is embedded in the mantle model AK135 Kennett et al. (1995) as the 1-D initial velocity model. $h_i(r)$ is applied to this model and $k_m(r,\omega)$ is calculated form this initial model. The first 30 modes of the surface wave are summed to generate the synthetic waveforms. The synthetic and the original waveforms are compared under the automated time-frequency window selection. Eventually, a set of γ_i is found, which gives the best fit between the synthetic and original waveforms within the selected windows. Then we obtained the phase velocity perturbations of the different modes and the perturbations in shear wave velocity. However, only the fundamental mode phase velocities were used in this study.

In order to determine the interstation phase velocity, we used the same criteria as described in the previous section to select seismic events for interstation phase velocity measurements, that is to say, only the events recorded by stations that share the same great circle path (within 7 degrees). The interstation phase velocity is obtained from the average phase velocities to the two stations

$$c(\omega) = \frac{c_1(\omega)\Delta_1 - c_2(\omega)\Delta_2}{\Delta_1 - \Delta_2}, \tag{2.3.8}$$

where Δ_1 and Δ_2 are the source-receiver distances. The indices 1 and 2 refer to the two stations. In this study, only fundamental mode phase velocities were used.

2.4 Comparison of the two methods

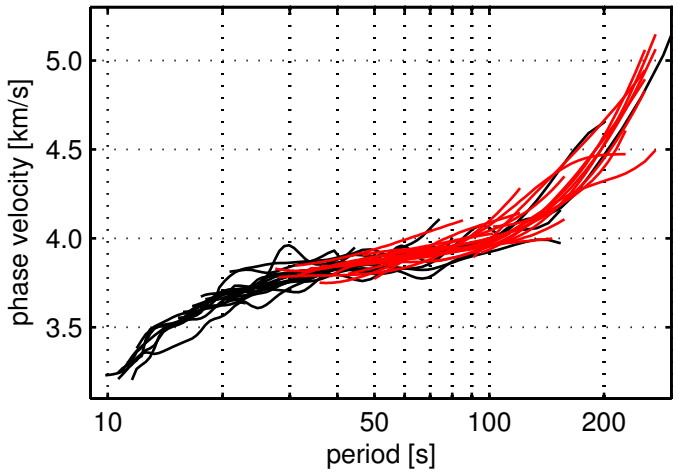

Figure 2.4.1: Phase velocity measurements for the path between station NE70 and station TOV. Red curves are phase velocity measurements obtained by AMI; black curves are phase velocity measurements obtained by the two-station method.

We found that the phase velocity curves obtained by the two methods are generally consistent. The cross-correlation measurements often extend to higher frequencies, whereas the AMI measurements yield lower frequency results. A representative example, which shows the agreement between the phase velocity measurements obtained by the two approaches, is shown in Figure 2.4.1. It also illustrates the difference in the frequency range of the measurements provided by the two different methods. Because the measurements are from same data, the difference is due to the method, not the data. From time-frequency analysis of the data, we found that for frequencies larger than approximately 50 mHz, the JWKB approximation of eq. 2.3.1 becomes inadequate in describing the propagation between the source and the receiver. This is because the scattering at lateral heterogeneities strongly influences the waveform at periods shorter than 20 s. Due to the stringent selection criteria in AMI the short period range is often discarded. In the case of the two-station cross-correlation method, two signals with a simi-

lar scattering pattern often still provide meaningful phase velocity estimations up to periods of approximately 10 s (Meier et al., 2004). At the other end of the spectrum, AMI, being based on mode summation, can separate the relatively long period fundamental mode from its higher mode contamination. AMI therefore generally retrieves longer period information than the two-station method.

We used cross-correlation measurements for paths across and around the gulf because their higher frequency content provides more constraints on the shallow structure, i.e. the crustal and uppermost mantle structure. AMI was used more extensively for the outer regions with paths to U.S. stations, so that the structure of the gulf could be interpreted in a broader regional setting.

2.5 Effects of wave propagation distortion

Our study is based on the assumption that surface waves propagate along the great-circle path. Therefore the interstation phase velocity samples the earth structure between the two stations. However, wave propagation distortion, due to heterogeneity outside the interstation path, such as off-great-circle propagation, multipathing and scattering, can cause biased estimates of the interstation phase velocities (e.g., Pedersen, 2006; Prindle and Tanimoto, 2006).

In this study, particularly for the paths along the strike of the coast, considerable differences were observed in the phase velocity measurements at short periods ($<$30 s). Figure 2.4.1 gives an example of how the biased data were identified and discarded in the phase velocity estimation procedure. For the path between station NE73 and NE78, 49 phase velocity curves were selected. However, there is a discrepancy between the phase velocity curves obtained for the two propagation directions. For the direction NE73 to NE78, that is to say, the wave-front propagating from NE73 to NE78, the fundamental mode Rayleigh wave phase velocity curves split at around 30 mHz towards the higher frequencies. We believe that this is the effect of the ocean-continent transition such as in those observed in southern California (e.g., Ji et al., 2005; Zhang et al., 2003). In this case, the phase velocity curves from the opposite direction, which are more consistent, are taken as reference. Therefore, the biased measurements were discarded in the second selection. Averaging a large number of interstation measurements reduces the standard deviation in the final estimation, and outliers were discarded in the final selection.

It is essential to have measurements from both propagating directions for each station pair, as well as a sufficient number of events. For each path, a minimum of 8 dispersion curves was required (which means at least 8 events per station

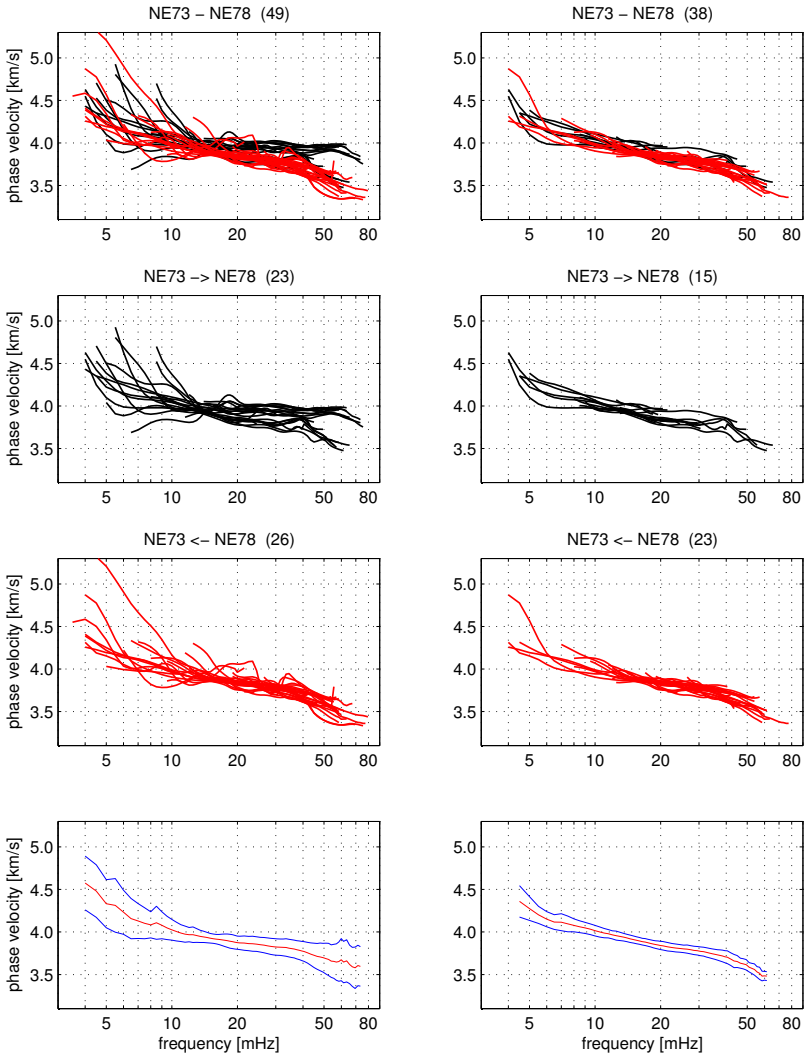

Figure 2.5.1: The off-great-circle phenomena observed in the phase velocity measurement for station pair NE73-NE80. The left panels show all phase velocity curves collected for this path. The right panels show the phase velocity collection eventually used in the mean phase velocity curve calculation. The mean phase velocity (in red) and its standard deviation (in blue) are shown in the bottom panels.

pair), though most paths have more than 20 individual interstation phase velocity measurements. The dispersion curves from different events often have a different frequency range. So, at the two ends of the frequency band, a minimum of 5 measurements was required to define the frequency band for the average dispersion curve of this interstation path.

2.6 Azimuthal anisotropy

Phase velocities vary as a function of horizontal direction (azimuth) in a plane-layered medium in the presence of general anisotropy. This phenomenon called azimuthal anisotropy. It is primarily due to the lattice preferred orientation of anisotropic minerals in the upper mantle and crust and is related to deformation history and mantle flow (Nicolas and Christensen, 1987). In the brittle upper crust, anisotropy can be caused by crack alignment due to the current tectonic stress (e.g., Meissner et al., 2006; Kaminski and Ribe, 2002; Crampin and Lovell, 1991). In a plane layered medium and in the presence of weak general anisotropy, phase velocities vary as a function of horizontal propagation direction, which can be described as (Smith and Dahlen, 1973):

$$\begin{aligned} dC(T,\psi) &= \delta C_{iso}(T) + \delta A_{2\psi}(T)\cos 2\psi + \delta B_{2\psi}(T)\sin 2\psi \\ &\quad +\delta A_{4\psi}(T)\cos 4\psi + \delta B_{4\psi}(T)\sin 4\psi \end{aligned} \tag{2.6.1}$$

where dC is the local phase velocity perturbation $C(T,\psi) - C_0(T)$, $C_0(T)$ is the reference phase velocity at the period T and ψ the azimuth of wave propagation. The coefficient δC_{iso} is the isotropic phase velocity perturbation and $\delta A_{2\psi}$, $\delta B_{2\psi}$, $\delta A_{4\psi}$ and $\delta B_{4\psi}$ parameterize azimuthal anisotropy. This equation can be rewritten as

$$\begin{aligned} dC(T,\psi) &= \delta C_{iso}(T) + \alpha_{2\psi}(T)\cos 2(\psi - \theta_{2\psi}(T)) \\ &\quad +\alpha_{4\psi}(T)\cos 4(\psi - \theta_{4\psi}(T)), \end{aligned} \tag{2.6.2}$$

where

$$\alpha_{2\psi}(T) = \sqrt{\delta A_{2\psi}^2(T) + \delta B_{2\psi}^2}(T), \quad \theta_{2\psi}(T) = \frac{1}{2}\arctan(\frac{\delta B_{2\psi}(T)}{\delta A_{2\psi}(T)});$$

so, when $\psi = \theta_{2\psi}(T)$ or $\pi + \theta_{2\psi}(T)$, then the 2ψ term reaches its maximum $\alpha_{2\psi}(T)$. Similarly, for the 4ψ terms

$$\alpha_{4\psi}(T) = \sqrt{\delta A_{4\psi}^2(T) + \delta B_{4\psi}^2}(T), \quad \theta_{4\psi}(T) = \frac{1}{4}\arctan(\frac{\delta B_{4\psi}(T)}{\delta A_{4\psi}(T)}).$$

when ψ = $\theta_{4\psi}(T)$, $\frac{1}{2}\pi + \theta_{4\psi}(T)$, $\pi + \theta_{4\psi}(T)$ or $\frac{3}{2}\pi + \theta_{4\psi}(T)$, then the 4ψ term reaches its maximum $\alpha_{4\psi}(T)$. Therefore, 2ψ terms have one fast propagation orientation, whereas 4ψ terms have two perpendicular fast propagation orientations.

2.7 Anisotropic phase velocity maps

In this study the interstation phase velocity measurements had sufficient azimuthal coverage to allow the construction of 2-D phase velocity maps that include the effects of azimuthal anisotropy. We followed the approach of Lebedev and van der Hilst (2008), using LSQR (Paige and Saunders, 1982) with smoothing and slight norm damping to a triangular model grid with a knot spacing of approximately 100 km. The inversion of a set of interstation phase velocity dispersion curves for a phase velocity map with azimuthal dependence, i.e. five parameters at each geographical grid point, is a linear inverse problem. At a given period, the interstation phase velocity perturbation for path i with an azimuth ψ is

$$\begin{aligned} d_i &= \sum_{j=1}^{m} K_{ij} dC_j \\ &= \sum_{j=1}^{m} K_{ij} (\delta C_{isoj} + \delta A_{2\psi j} \cos 2\psi + \delta B_{2\psi j} \sin 2\psi \\ &\qquad + \delta A_{4\psi j} \cos 4\psi + \delta B_{4\psi j} \sin 4\psi) \\ &= \sum_{j=1}^{m} K_{ij} (\delta C_{isoj} + \alpha_{2\psi j} \cos 2(\psi - \theta_{2\psi j}) \\ &\qquad + \alpha_{4\psi j} \cos 4(\psi - \theta_{4\psi j})) \end{aligned} \tag{2.7.1}$$

where K_{ij} is the weight of grid point j to path i which is determined by the relative position between the grid point and the path (Lebedev and van der Hilst, 2008); m is the number of grid points on the phase velocity map. If we combine the linear equations for all paths at this period, then we get a set of n linear equations, where n is the number of paths. Now the relationship between data (interstation phase velocity measurements) and model (five-term phase velocity perturbations on discrete spatial grid points) may be written in matrix form

$$\mathbf{d} = \mathbf{G}\mathbf{m} + \mathbf{e}, \tag{2.7.2}$$

where $\mathbf{b}$ is the data vector, and $\mathbf{e}$ is its error factor. In this study, We assume the errors in the interstation phase velocity measurements have Gaussian distribution.

$\mathbf{G}$ is a $n \times 5m$ matrix. the elements of $\mathbf{G}$ is defined from the forward formulation above as

$$G_{ij} = \begin{cases} K_{il} & j=l \\ K_{il}\cos 2\psi & j=m+l \\ K_{il}\sin 2\psi & j=2m+l \\ K_{il}\cos 4\psi & j=3m+l \\ K_{il}\sin 4\psi & j=4m+l \end{cases}, \; l=1,\ldots,m. \tag{2.7.3}$$

The model space is then described in 5 m size sub-spaces, where m is the number of grid points on the phase velocity map. So

$$\mathbf{m} = (\delta\mathbf{C_{iso}}, \quad \delta\mathbf{A_{2\psi}}, \quad \delta\mathbf{B_{2\psi}}, \quad \delta\mathbf{A_{4\psi}}, \quad \delta\mathbf{B_{4\psi}})^{\mathbf{T}}. \tag{2.7.4}$$

In this study, the inverse problem is solved using the LSQR method (Paige and Saunders, 1982) with lateral smoothing and slight norm damping as described in Lebedev and van der Hilst (2008). That is to say that to estimate $\mathbf{m}$ we choose to minimize the following penalty function:

$$(\mathbf{G(m)} - \mathbf{d})^{\mathbf{T}}\mathbf{C_e^{-1}}(\mathbf{G(m)} - \mathbf{d}) + \mathbf{m}^{\mathbf{T}}\mathbf{C_m^{-1}}\mathbf{m}, \tag{2.7.5}$$

where $\mathbf{C}_e$ is the data covariance matrix and $\mathbf{C}_m^{-1}$ is the inverse of the prior model covariance matrix. The prior model covariance matrix is the result of the regularization, i.e. the spatial smoothing and norm damping used in the inversion. It can be determined in the following way (Barmin et al., 2001):

$$\mathbf{C_m^{-1}} = \mathbf{F}^{\mathbf{T}}\mathbf{F} + \mathbf{H}^{\mathbf{T}}\mathbf{H}, \tag{2.7.6}$$

where the smoothing constraint is incorporated with $5m \times 5m$ block-diagonal matrix F as follows:

$$\mathbf{F} = \begin{pmatrix} \alpha_0\mathbf{F^0} & 0 & 0 & 0 & 0 \\ 0 & \alpha_{2\psi}\mathbf{F^0} & 0 & 0 & 0 \\ 0 & 0 & \alpha_{2\psi}\mathbf{F^0} & 0 & 0 \\ 0 & 0 & 0 & \alpha_{4\psi}\mathbf{F^0} & 0 \\ 0 & 0 & 0 & 0 & \alpha_{4\psi}\mathbf{F^0} \end{pmatrix}, \tag{2.7.7}$$

where α_0, $\alpha_{2\psi}$, $\alpha_{4\psi}$ are the smoothing factor for isotropic, 2ψ and 4ψ anisotropic terms respectively. The $m \times m$ matrix $\mathbf{F}^0 = (F_{ij})$ is:

$$F_{ij} = \begin{cases} 1/p_i & i \neq j \\ 1/p_i - 1 & i = j \end{cases}, \tag{2.7.8}$$

where p_i is the number of neighbors of the ith grid point (Lebedev and van der Hilst, 2008). The norm constrains is encoded within the diagonal matrix $\mathbf{H}$ as follows:

$$\mathbf{H} = \begin{pmatrix} \beta_0\mathbf{I} & 0 & 0 & 0 & 0 \\ 0 & \beta_{2\psi}\mathbf{I} & 0 & 0 & 0 \\ 0 & 0 & \beta_{2\psi}\mathbf{I} & 0 & 0 \\ 0 & 0 & 0 & \beta_{4\psi}\mathbf{I} & 0 \\ 0 & 0 & 0 & 0 & \beta_{4\psi}\mathbf{I} \end{pmatrix}, \tag{2.7.9}$$

where β_0, $\beta_{2\psi}$, $\beta_{4\psi}$ are the norm damping factor for isotropic, 2ψ and 4ψ anisotropic terms respectively, and $\mathbf{I}$ is a $m \times m$ identical matrix. With these definitions the inversion operator, $\mathbf{L}$, is defined as follows:

$$\mathbf{L} = (\mathbf{G^T C_e^{-1} G} + \mathbf{C_m^{-1}})^{-1}\mathbf{G^T C_e^{-1}} \tag{2.7.10}$$

The regularization of the inversion, i.e. the smoothing and damping, influences the results of the inversions. The choice, however, is made subjectively. Our choice is based upon several criteria. Firstly, a set of phase velocity maps at each period was inverted with different smoothing and damping factors. We chose only slight norm damping and smoothed the isotropic, 2ψ and 4ψ anisotropic terms independently, as discussed below.

As the smoothing factor for the isotropic term increased, the isotropic pattern started to stabilize. That is to say, the pattern did not change much anymore; only the amplitude of the pattern decreased with the increasing smoothing factor. The criterion used to choose the smoothing factor for the isotropic term, was that it must be one which provides these consistent patterns with the largest variance reduction.

The anisotropic terms require more smoothing due to the additional requirements on the azimuthal distribution of the paths. In order to find the stable pattern of the 2ψ term for the Rayleigh wave phase velocity maps of chapters 3 and 4, we applied a resolution test on each inversion result (with different smoothing and damping). In this resolution test, the input interstation phase velocities were calculated using models with the isotropic terms taken from the actual inverted phase velocity results. The 2ψ anisotropic terms were such that the anisotropy was of the same strength but with the fast-propagation directions perpendicular to those of the inverted phase velocity maps. This set of interstation phase velocities was again inverted to phase velocity maps with the same smoothing and damping factor. In these resolution tests, the recovered anisotropic fast directions started to become perpendicular to the original 2ψ anisotropic fast directions as

the smoothing factor increased. We took this, the two fast directions orthogonal, as a criterion in the selection of the smoothing factor for the 2ψ anisotropic term.

We calculated resolution matrices (see next section) to further investigate the resolution of the various terms. We found that the isotropic terms were recovered in a stable way and the 2ψ terms of the Rayleigh wave maps for regions with a good path coverage. The results of 4ψ terms, however, were not robust. We took the same smoothing factor for the 4ψ anisotropic terms as for the 2ψ anisotropic terms, since the criteria for choosing the smoothing factor for the 2ψ anisotropic terms were already quite severe.

2.8 Resolution and uncertainty analysis

The primary goal of a geophysical inverse problem is to estimate the unknown model parameters from a set of observations. It is important to characterize how reliable the resulting model parameters are through a resolution analysis. However, the estimated phase velocity map will not represent the true model, because LSQR (Paige and Saunders, 1982) is used with smoothing and slight norm damping, and there are errors in the data and there is a null space. If we call the true model $\mathbf{m_t}$, then the inverted model is

$$\mathbf{m} \;=\; \mathbf{R}\mathbf{m_t}, \tag{2.8.1}$$

where $\mathbf{R}$ is the resolution matrix. Consider the ith equation of the equation above, it gives

$$m_i \;=\; \sum_{j=1}^{m} R_{ij}(\mathbf{m_t})_j. \tag{2.8.2}$$

So, each estimated model component m_i is a weighted average of the entire true model space.

In this problem, the relation between estimated phase velocity perturbation and the true model can be written as

$$\begin{pmatrix} \delta\mathbf{C_{iso}} \\ \delta\mathbf{A_{2\psi}} \\ \delta\mathbf{B_{2\psi}} \\ \delta\mathbf{A_{4\psi}} \\ \delta\mathbf{B_{4\psi}} \end{pmatrix} \;=\; \mathbf{R} \begin{pmatrix} \delta\mathbf{C_{iso}}_{(t)} \\ \delta\mathbf{A_{2\psi}}_{(t)} \\ \delta\mathbf{B_{2\psi}}_{(t)} \\ \delta\mathbf{A_{4\psi}}_{(t)} \\ \delta\mathbf{B_{4\psi}}_{(t)} \end{pmatrix}. \tag{2.8.3}$$

Therefore, the *i*th equation will be

$$m_i = \sum_{j=1}^{5m} R_{ij}(\mathbf{m}_t)_j, \tag{2.8.4}$$

$$\begin{aligned} m_i = & \sum_{j=1}^{m} R_{ij}(\delta \mathbf{C}_{\mathbf{iso}(t)})_j \\ & + \sum_{j=1}^{m} R_{i(m+j)}(\delta \mathbf{A}_{\mathbf{2}\psi(t)})_j + \sum_{\mathbf{j=1}}^{\mathbf{m}} \mathbf{R}_{i(2m+j)}(\delta \mathbf{B}_{\mathbf{2}\psi(t)})_j \\ & + \sum_{j=1}^{m} R_{i(3m+j)}(\delta \mathbf{A}_{\mathbf{4}\psi(t)})_j + \sum_{\mathbf{j=1}}^{\mathbf{m}} \mathbf{R}_{i(4m+j)}(\delta \mathbf{B}_{\mathbf{4}\psi(t)})_j. \end{aligned} \tag{2.8.5}$$

The resolution matrix $\mathbf{R}$ is thus a $5m \times 5m$ matrix. In the perfect case that the estimated model equals the true model, the resolution matrix would be an identity matrix. In practice, in our case, the resolution matrix will be far from ideal, having nonzero off-diagonal elements. The LSQR method does not provide the resolution matrix directly, but it is possible to reconstruct it from the forward matrix $\mathbf{G}$ and its generalized inverse, the LSQR operator L (Trampert and Lévêque, 1990; Snieder and Trampert, 1999; Deschamps et al., 2008). In the LSQR method, the estimated model will be

$$\mathbf{m} = \mathbf{L}\mathbf{d}, \tag{2.8.6}$$

then,

$$\mathbf{m} = \mathbf{L}\mathbf{G}\mathbf{m}_t. \tag{2.8.7}$$

The jth column of the resolution matrix $\mathbf{R}$ is obtained from the jth column of the forward matrix $\mathbf{G}$,

$$\mathbf{R}_j = \mathbf{L}\mathbf{G}_j. \tag{2.8.8}$$

Figure 2.8.1 shows a resolution matrix for the 30 s phase velocity map of the fundamental mode Love wave in chapter 5. We illustrate the resolution matrix in 25 sub-matrices of size $m \times m$ which represent the geographical knots of our model. The diagonal sub-matrices indicate lateral trade-offs, that is, trade-offs between parameters representing a given term at different geographical locations. We call it smearing. These trade-offs are in large part due to smoothing. The off-diagonal matrices indicate trade-offs between model parameters of different types. We call it leakage. We can see the effect of both smearing and leakage. In this case

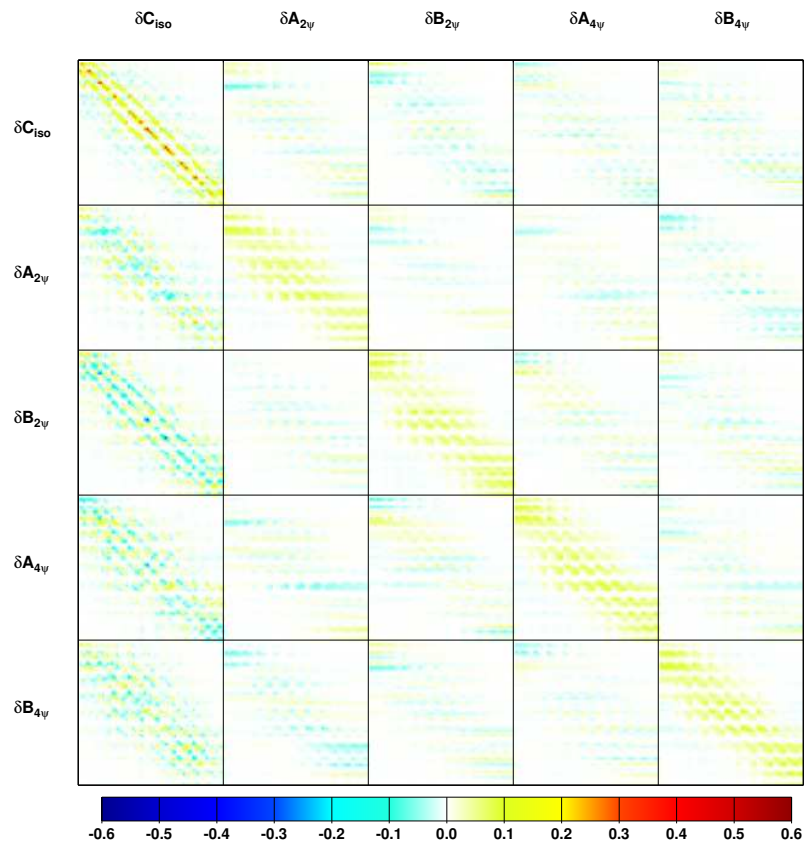

Figure 2.8.1: Resolution matrix for the 30 s Love wave phase velocity map of chapter 5. Each row/column of the matrix represents a parameter (here, 5 terms at 63 geographical locations, i.e. a total of 315 parameters). The matrix is illustrated in 25 sub-matrices of size 63×63 which represent the geographical knots of our model. The diagonal sub-matrices indicate lateral trade-offs, that is, trade-offs between parameters representing a given term at different geographical locations (smearing). The off-diagonal matrices indicate trade-offs between model parameters of different types (leakage).

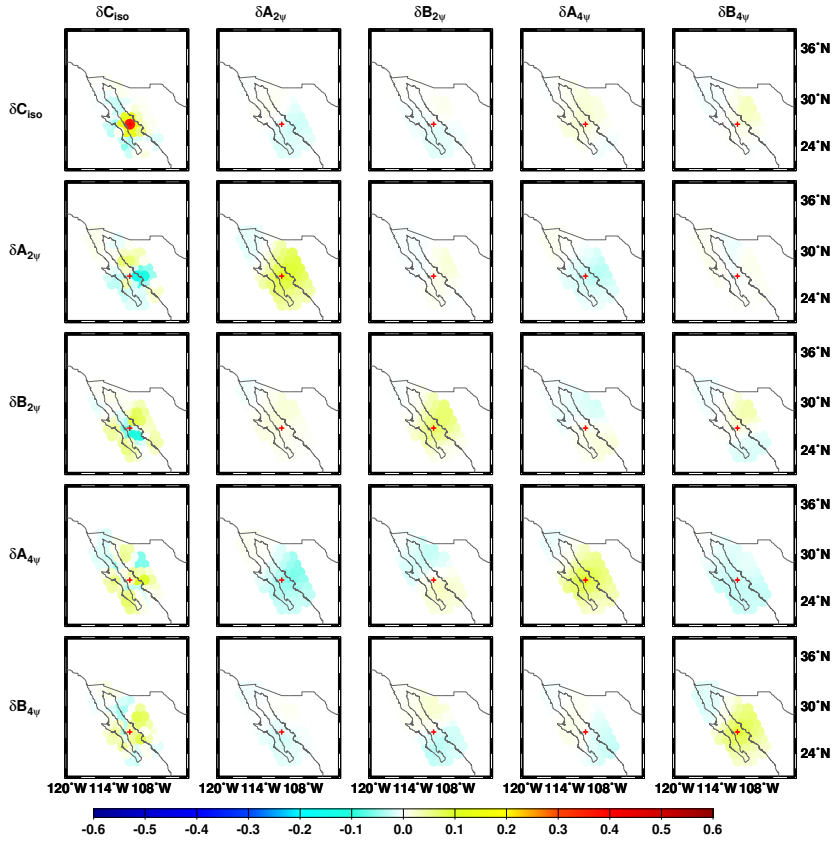

Figure 2.8.2: The resolution for one grid point in 30 s Love wave phase velocity map of chapter 5. The location of the grid point is indicated as a red cross. The colour indicates the value of the resolution matrix.

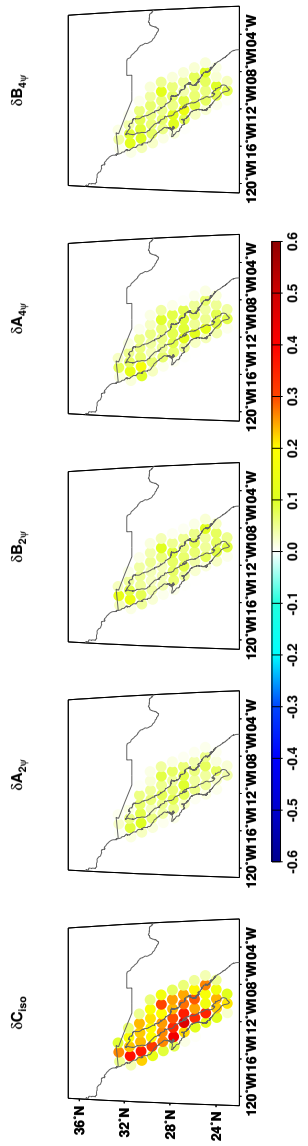

Figure 2.8.3: The geographical image of the diagonal elements of the resolution matrix, for the 30 s fundamental mode Love wave phase velocity map in chapter 5.

there is clear leakage from the isotropic terms into the 2ψ- and 4ψ-terms, which means that these anisotropic terms are not reliably determined. In Figure 2.8.2, we plotted the resolution matrix for one grid point geographically to visualize how this five-component phase velocity perturbation at a single grid point is estimated over the entire model space. We can interpret these $5m \times 5m$ panels as a $5m \times 5m$ matrix: each row of panels shows how the estimated component is weighted over the entire true model; the 5 diagonal panels indicate the smearing effect and the off-diagonal panels indicate the leakage. Smearing (the diagonal panels) is clear from the patterns of the isotropic and anisotropic terms, and is largely due to the imposed smoothness. Leakage (the off-diagonal panels) is clear from the first column: the isotropic term leaks into the anisotropic terms.

In Figure 2.8.3, we show the diagonal elements of the resolution matrix (Figure 2.8.1) geographically in order to get a grip on what we call the resolved area. In the end, we took a rather subjective criterion to define the resolved region of each phase velocity map. The region of good resolution was defined by the grid points for which the diagonal element of the isotropic term of the resolution matrix has a value larger than 0.10.

It is worth noticing that, as shown in Figure 2.8.2, the isotropic local anomalies ($<$150 km) will be averaged out in our models, even in the well resolved areas.

Another important issue in the inversion is to know the uncertainty of the estimated model. The uncertainty in the estimated model parameters comes from both the uncertainty in the data and the uncertainty in the model arising from indeterminacy of the original equations. The former is mapped into model space through the data contribution, the latter is propagated into model space through the prior model space constrains. The covariance matrix for the model parameters is (Tarantola, 1987; Gubbins, 2004):

$$\begin{aligned} \mathbf{C} &= (\mathbf{G^T C_e^{-1} G} + \mathbf{C_m^{-1}})^{-1} \\ \mathbf{C} &= (\mathbf{I} - \mathbf{R})\mathbf{C_m}. \end{aligned} \tag{2.8.9}$$

In order to evaluate the uncertainties of the phase velocity maps, we have calculated the posterior model covariance matrices. The square roots of the diagonal elements of the posterior model covariance matrices can be interpreted as the standard deviations of the estimated model parameters, i.e. the phase velocity perturbations at the grid points (Tarantola, 1987). The uncertainties of the isotropic phase velocity perturbations range from 0.7% (middle periods) to 1.3% (short and long periods), whereas they are around 0.4% for the anisotropic terms (in chapter 4). The differences are mainly due to the variations in path coverage and differences in smoothing. We noticed that the uncertainty in the anisotropic terms

is much smaller than the uncertainty in the isotropic terms, this is due mainly to the stronger smoothing factors used on the anisotropic terms. This illustrates the trade-off between resolution and uncertainty. The final model we chose is a balanced combination of these two terms.

2.9 Radial anisotropy

Radial anisotropy is one of the expressions of general anisotropy of the Earth's interior. Montagner and Nataf (1986) showed that Love and Rayleigh wave propagation can be described by linear combinations of 13 elastic constants, 5 of which are the azimuth-independent Love parameters (A, C, L, N, F) are representative of a transversely isotropic medium with a vertical axis of symmetry (Love, 1927).

The presence of transverse isotropy in the upper mantle causes a discrepancy in the shear velocities inferred from Love and Rayleigh waves. This phenomenon is called radial anisotropy (e.g. Anderson, 1961) or polarization anisotropy, because horizontally-propagating shear waves with a horizontal polarization have a different speed from those with a vertical polarization.

Radial anisotropy is often characterized by two parameters, $V_{SH} = \sqrt{N/\rho}$ (horizontally-polarized shear wave speed inferred from Love waves) and $V_{SV} = \sqrt{L/\rho}$ (vertically-polarized shear wave speed inferred from Rayleigh waves). More often, other parameters are used, such as the Voigt average of the S-velocity, defined as $V_{S(iso)} = \sqrt{(2V_{SV}^2 + V_{SH}^2)/3}$, and the strength of radial anisotropy ξ, defined as $\xi = \frac{V_{SH}^2}{V_{SV}^2}$ (Panning and Romanowicz, 2006). Radial anisotropy is often required for a correct interpretation of the retrieved S-velocity structure in tomographic studies, at least in the first 400 km of the upper mantle (Gung et al., 2003; Visser et al., 2008).

2.10 Inversion for S-wave velocity and radial anisotropy

For the local shear velocity inversion, we estimate, at each geographical location, the Love and Rayleigh phase velocity dispersion curves from the phase velocity maps. We assumed a 0.5% uncertainty for the phase velocty curves. Because Love and Rayleigh wave phase velocities are most sensitive to shear speed (see Fig. 2.10.1), so in the inversion, we invert the Rayleigh- and Love-wave dispersion curves simultaneously for average shear speed $V_{S(avg)} = (V_{SV} + V_{SH})/2$ and the amount of radial anisotropy $(V_{SH} - V_{SV})$. The compressional wave speed

V_P was assumed to be isotropic with its perturbation coupled to the $V_{S(avg)}$ as $\frac{dlnV_{S(avg)}}{dlnV_P} = 1.7$. The density is fixed in the inversion.

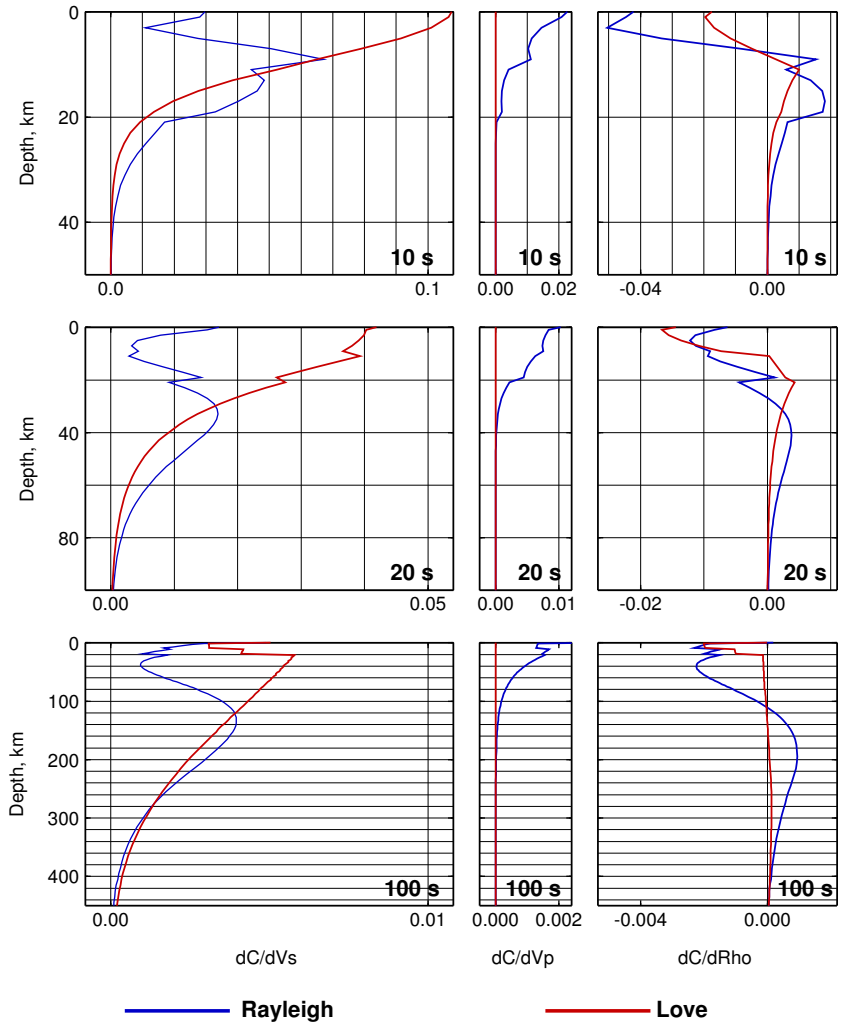

Figure 2.10.1: Depth sensitivity kernels for fundamental mode Love and Rayleigh phase velocity at three different periods.

The inversion is performed by a non-linear optimisation. Synthetic Love and Rayleigh wave phase velocities are recomputed from the perturbed velocity model after each iteration. The phase velocities are calculated by assuming isotropy, that is to say, when we calculated Love phase velocities, the shear speed is set equal to

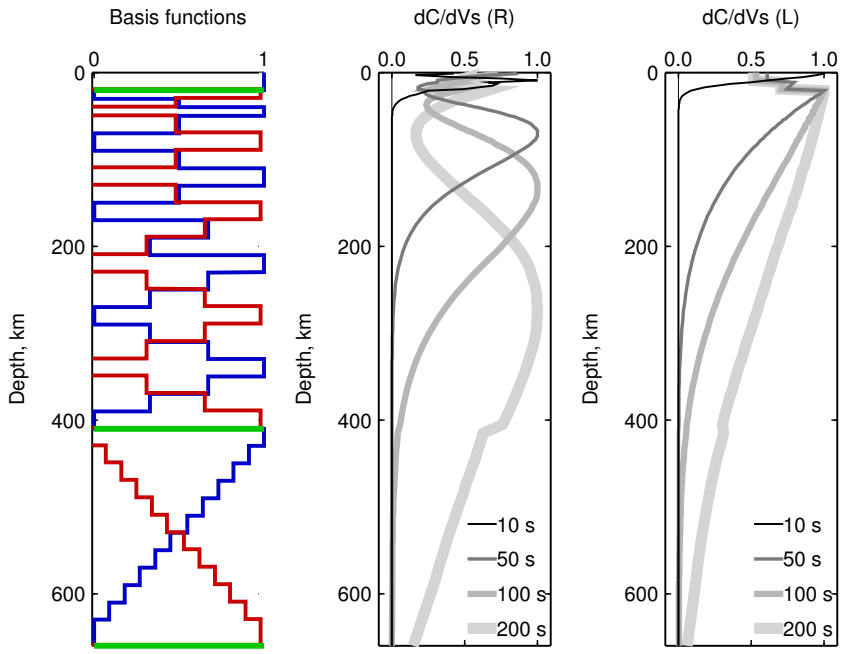

Figure 2.10.2: . Left: example of a set of basis functions spanning the crust and upper mantle used in the shear velocity inversion. The green lines indicate the discontinuities of which the depths can be perturbed. The blue and red lines are used to illustrate the boxcar and triangular basis functions used in the inversion. The basis functions are used to perturb both the average shear speed $V_{S(avg)} = (V_{SV} + V_{SH})/2$ and the amount of radial anisotropy $V_{SH} - V_{SV}$. Middle: Depth sensitivity kernels for fundamental mode Rayleigh phase velocity to shear wave speed at different periods, normalized at the maximum ratio. Right: Depth sensitivity kernels for fundamental mode Love phase velocity to shear wave speed at different periods, normalized at the maximum ratio.

V_{SH}, whereas for Rayleigh, the shear speed is set equal to V_{SV}. Fortunately, the difference between the fundamental mode phase velocities calculated for a radially anisotropic model and the corresponding isotropic model is negligible (Visser et al., 2008).

The starting models for the inversions were obtained from the reference model AK135 (Kennett et al., 1995) for the mantle structure, combined with a local crustal structure as described in chapter 4. We used 15 free parameters to expand shear speed variations down to a depth of 1000 km (see Fig. 2.10.2). Of the 15 parameters, one is boxcar in shape and spans the crust; 11 are triangular basis functions parameterising mantle structure, with denser sampling at shallower mantle depths; 3 more parameters allow depth perturbations of the Moho, 410-km

and 660-km discontinuities. The inverted Rayleigh phase velocity curve spans a period range of 9 to 250 s, whereas that of Love is 9 to 160 s. These period ranges represent a depth sensitivity down to the transition zone (see Fig. 2.10.2). Nevertheless, as the period increases, we have fewer interstation phase velocity measurements and a larger uncertainty. This results in poor resolution and more uncertainty in the inverted shear velocity structure at greater depth. Several sets of inversions were performed with mild and strong damping towards the average shear speed $V_{S(avg)}$ and the reference model. The results on radial anisotropy are presented in chapter 5.

Chapter 3

Surface wave tomography of the Gulf of California

Abstract. We measured interstation fundamental mode Rayleigh wave phase velocities using data from the NARS-Baja seismic network located around the Gulf of California. A region-average, shear velocity model and a set of azimuthally anisotropic phase velocity maps are obtained from these data. The average shear velocity structure shows a strong low-velocity zone underlying a thin lid and the data are suggestive of low velocities down into the transition zone. The phase velocity maps display signatures of sedimentary layers, crustal thickness variations, upwelling under the plate boundary, and the presence of the subducted Farallon microplate remnants beneath the Gulf. The upper mantle features inferred from this study provide new seismic evidence on the tectonic evolution of the region.

3.1 Introduction

In the Gulf of California the Pacific-North America plate boundary changes character from an oceanic-type spreading center and transform fault system in the south to a region of diffuse continental extensional deformation in the north (Nagy and Stock, 2000). The system is a result of tectonic interaction between the Pacific, Farallon and North America plates (e.g., Lonsdale, 1991; Nicholson et al.,

This chapter has been published as: X. Zhang, H. Paulssen S. Lebedev and T. Meier, Surface wave tomography of the Gulf of California, *Geophysical Research Lettters* **34**, L15305, doi:10.1029/2007GL030631, 2007

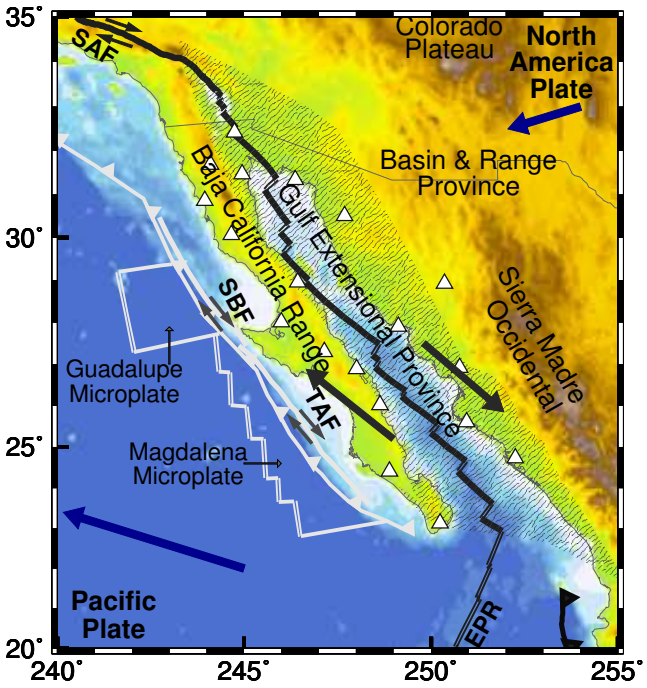

Figure 3.1.1: Tectonic map of the Gulf of California region. The NARS-Baja stations are depicted by white triangles. The main tectonic provinces are Baja California Range, Gulf Extensional Province (dotted), Basin and Range Province, Sierra Madre Occidental and Colorado Plateau. Present-day plate boundaries shown as dark lines. Inactive plate boundaries shown as white lines. SAF−San Andreas Fault; EPR−East Pacific Rise; SBF−San Benito Fault; TAF−Tosco Abreojos Fault. Thick arrows indicate plate motions (absolute plate motion in blue, relative plate motion in black) predicted by global plate motion model HS3-NUVEL1A (Gripp and Gordon, 2002).

1994; Bohannon and Parsons, 1995; Atwater and Stock, 1998). As the Pacific-Farallon spreading ridge reached the North American plate (ca. 28 Ma), the character of the plate boundary contact changed from Farallon-North America oblique subduction to Pacific-North America transcurrent motion with an extensional component taken up by the North American continent. With time the Rivera triple junction migrated southward and the intervening Farallon plate started to fragment into various microplates. Subduction of the Guadalupe and Magdalena microplates (Figure 3.1.1) beneath Baja California ceased ca. 12 Ma. The Pacific-North America plate motion was largely accommodated along the right-lateral San-Benito-Tosco-Abreojos fault zone west of Baja, but over time the relative

plate motion was increasingly accommodated by strike-slip motion and extension in the future gulf area. This was to become the Gulf Extensional Province, bordered west by the more rigid Baja California Range and east by the unextended block of the Sierra Madre Occidental. Around 6 Ma, almost all of the Pacific-North America plate motion was accommodated inside of the Gulf (e.g., Lonsdale, 1991; Oskin and Stock, 2003). Global and regional tomographic studies have revealed a pronounced low-velocity anomaly in the top 250 km of the mantle beneath the Gulf of California area (e.g., Lebedev and van der Hilst, 2008; van der Lee and Frederiksen, 2005; Godey et al., 2003). However, these tomographic images do not have sufficient resolution to interpret the tectonic process active in this region. The NARS-Baja stations deployed around the Gulf of California (Trampert et al., 2003) allow us to explore the upper mantle structure at a more detailed level. Here we present a set of azimuthally anisotropic, fundamental mode Rayleigh wave phase velocity maps and the results of a one-dimensional, shear velocity inversion of the phase velocity measurements averaged over the Gulf of California region. The results give us insight into the driving forces under this dynamic plate boundary system.

3.2 Data and interstation phase velocity measurements

We adopted the method described by Meier et al. (2004) to measure the dispersion curves of fundamental mode Rayleigh waves along up to 139 interstation paths (see section 3.8: Auxiliary material). The phase velocity measurements were obtained from seismograms recorded by NARS-Baja stations between April 2002 and the end of 2004. The data set included 6075 vertical component seismograms of 543 strong events (moment magnitude $\geq$ 5.0) recorded at NARS-Baja stations. For each station pair, we cross-correlated the two vertical component seismograms excited by an event, whose epicenter is located along the great circle path ($\pm 7^{\circ}$) determined by this station pair. Frequency-dependent filtering and weighting are applied to the cross-correlation function before the reliable part of the phase velocity curve is interactively selected in the frequency domain. This process was repeated for all the events and the final dispersion curve is obtained as the average of all the phase velocity curves. Our interstation dispersion measurements have been averaged over 10–189 individual phase velocity curves.

Finite-frequency effects due to heterogeneity outside the interstation path, such as off great-circle propagation, multipathing and scattering (e.g., Prindle and Tanimoto, 2006; Zhang et al., 2003) can cause biased estimates of interstation phase velocities. These effects are reduced by the averaging process, but for some

station pairs systematic differences were observed between the measurements for the two opposite propagation directions at periods shorter than 30 s. This is suggestive of off great-circle propagation, particularly since these station pairs are oriented along the strike of the peninsula where a significant influence from the ocean-continent transition is expected for events from the north-west. We discarded these biased measurements recognized by their higher phase velocities to obtain more reliable estimates of the dispersion curves.

3.3 1-D Shear velocity model space search

The interstation phase velocity measurements of our data set span the period range of 9–250 s and are sensitive to shear velocity structure from the crust down to the mantle transition zone. We explored shear velocity models with corresponding phase velocity curves within one standard deviation from the average over all measured phase velocities. Detailed information about the model space search can be found in section 3.8 (Auxiliary material). Figure 3.3.1 shows the result of the model space sampling. A persistent feature is a strong low-velocity zone in the upper 200 km, in which the shear velocity can be up to 10% lower than in the global reference model AK135 (Kennett et al., 1995). The detailed character of the low-velocity zone of the average model is uncertain, as illustrated by the ensemble of gray curves in figure 3.3.1. Thus, we do not to interpret the low-velocity zone in terms of melt, water, and/or variations in grain size, although fluids or melt have been suggested by Goes and van der Lee (2002) for this region. Another noticeable feature is that the best fitting models have lower velocities in the transition zone than the reference model AK135. In the model space search, the transition-zone shear velocities reaches the reference value (AK135), but it is the upper limit of the possible models, and requires very low velocities in the upper 400 km. Thus the low average phase velocities in the period range of 100 to 250 s suggest that the shear velocity in the transition zone is substantially lower than the global average, which could imply the presence of a deep seated heat source affecting processes at shallower levels.

3.4 Phase velocity maps with azimuthal anisotropy

Our data yields sufficient coverage to map both isotropic and anisotropic phase velocity variations. In a plane layered medium and in the presence of weak general anisotropy, phase velocities vary as a function of horizontal propagation direc-

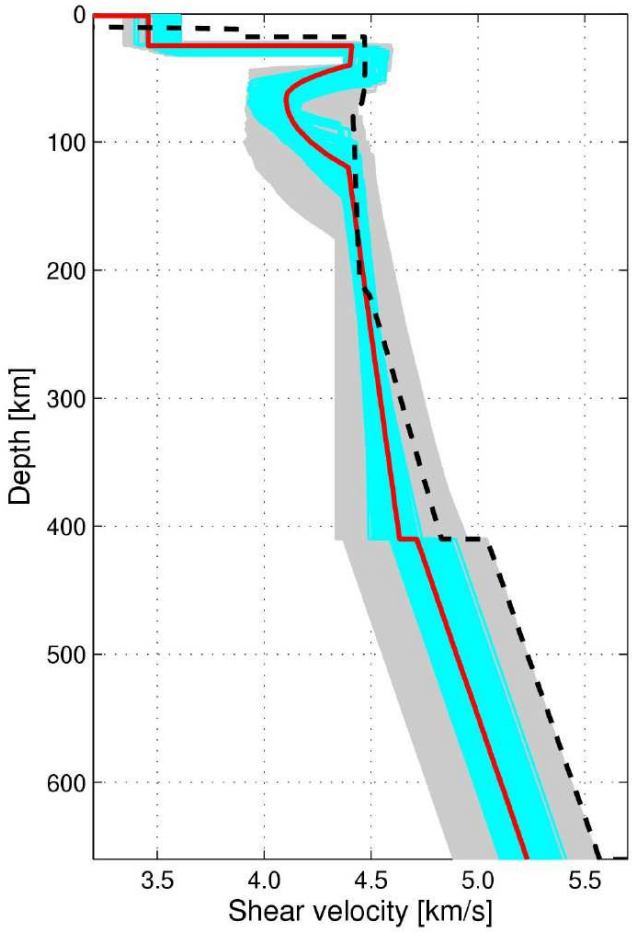

Figure 3.3.1: 1-D model space search results. The gray lines show all models whose phase velocity curve is within one standard deviation away from the mean of all interstation phase velocity measurements. The cyan lines represent the 1000 best fitting models. The best fitting model is shown in red. Model AK135 is shown with a dashed black line.

tion (Smith and Dahlen, 1973):

$$\begin{aligned}\frac{dc}{c}(T,\Psi) &= \alpha_0(T) + \alpha_1(T)\cos 2\Psi + \alpha_2(T)\sin 2\Psi \\ &\quad +\alpha_3(T)\cos 4\Psi + \alpha_4(T)\sin 4\Psi\end{aligned} \tag{3.4.1}$$

where dc/c is the local relative phase velocity perturbation, T the period and Ψ the azimuth of wave propagation. The coefficient α_0 is the isotropic phase velocity perturbation; α_1, α_2, α_3 and α_4 parameterize azimuthal anisotropy.

We constructed phase velocity maps for the period range of 10–100 s (for ray coverage see section 3.8). The inversion, which includes the isotropic as well as the 2Ψ and 4Ψ terms, is performed with LSQR (Paige and Saunders, 1982) with smoothing and (slight) norm damping as described by Lebedev and van der Hilst (2008). The triangular model grid has knot spacing of around 100 km. We calculated resolution matrices and show the results only for the well-sampled areas—defined as those with grid points whose diagonal element of the isotropic term of the resolution matrix has a value larger than 0.10. Analysis of the resolution ma-

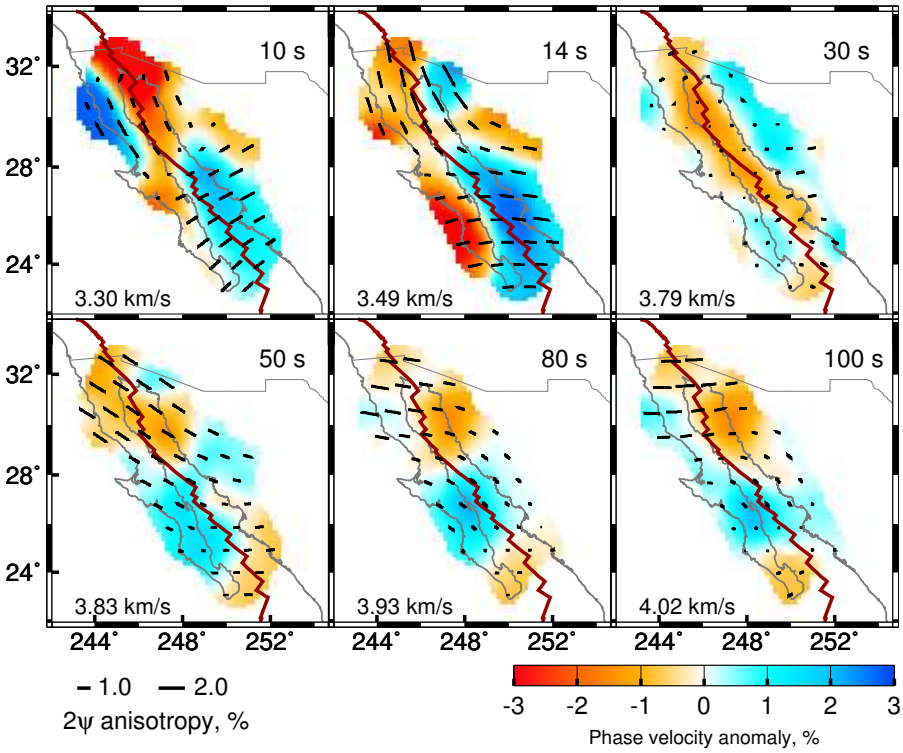

Figure 3.4.1: Tomographic images of Rayleigh wave phase velocities at different periods. The period is shown in the upper right corner and the reference phase velocity is in the lower left corner of each phase map. The colors indicate the isotropic anomalies and the black bars indicate the fast-propagation directions and the strength of the azimuthal anisotropy. The purple line marks the location of the plate boundary.

trices showed that leakage between the isotropic and anisotropic terms is small. This is confirmed by resolution tests with synthetic input data containing no anisotropy, but the inversion allowing for anisotropy. Furthermore, the measured data requires anisotropy as inferred from a statistically significant increase in variance reduction. The isotropic coefficients are better resolved than the 2Ψ and 4Ψ terms which require more smoothing. Thus, the resolution lengths of the isotropic coefficients are approximately 100–200 km, whereas they are 200–400 km for the anisotropic coefficients. A resolution test which illustrates the robustness of the results is shown in section 3.8. Figure 3.4.1 presents the results of the inversion only for the isotropic and the 2Ψ terms. We have allowed for 4Ψ heterogeneity but verified that our main results and conclusions—concerning isotropic and "2Ψ" structure—are robust with respect to the amount of the 4Ψ signal allowed in the models by the regularization.

3.5 Interpretation and discussion

Phase velocity maps are commonly inverted for shear velocity structure to allow a direct interpretation of the structural features. Such an inversion requires an accurate crustal model in order to obtain reliable estimates of the mantle structure. The crustal structure in this area is, however, very complex and insufficiently known to currently warrant a 3-D shear velocity inversion. We therefore interpret the phase velocity maps. Overall, these maps show a difference between the northern part of the gulf and south of roughly $29°$N. This is first observed for the maps at periods of 10 and 14 s. In the northern part, effects of a thick layer of low-velocity sediments (González-Fernández et al., 2005) are visible for short period phase velocities (10 s). Variations in crustal thickness dominate at 14 s. The crust beneath the southern part of the Gulf of California is oceanic and thinner than beneath the northern part. The large contribution of the high mantle velocities beneath the thin oceanic crust explains the relatively high phase velocities at periods of 10 and 14 s in the southern part of the area. These high phase velocities extend onto the western part of the Mexican mainland, indicating that its crust is thinner than beneath the Baja California peninsula. The area of high phase velocities at the 14 s matches the Gulf Extensional Province (e.g., Stock and Hodges, 1989) in figure 3.1.1, confirming the crustal thinning as inferred from geological data. The sharp transition along the eastern margin of the Baja California peninsula marks the western boundary of the Gulf Extensional Province. The low phase velocity anomalies on the Mexican mainland at $30°$N can be explained by a thick crust (40 km), according to a receiver function study using NARS-Baja data by Persaud

et al. (2003).

The fast anisotropic directions in the 10-14 s period phase velocity maps are approximately NNW-SSE in the northern part of the gulf and Baja California. This direction is roughly parallel to the plate boundary which has a transtensional character in this region of diffuse continental deformation (Nagy and Stock, 2000). In contrast, in the southern part of the Gulf the fast-propagation directions are NE-SW to E-W, close to being perpendicular to the plate boundary. This direction corresponds to the direction of opening of the Gulf, which is similar to the direction of past subduction. At a period of 30 s (max. sensitivity at a depth interval around 50 km), low velocities are found directly beneath the plate boundary over the entire length of the gulf. These low anomalies could be caused by melt and/or fluids feeding the ridge system in the gulf. Noticeably, the azimuthal anisotropy becomes smaller in amplitude at this period, which, speculatively, could be related to local upwelling beneath the plate boundary reducing the horizontal component of flow. The north-south contrast is seen again in the phase velocity maps in the 50-80 s period range (max. sensitivity $\sim$50-150 km). Relatively high phase velocities (although still lower than the global average) are observed at latitudes roughly 24°–28°N. We suggest that these high phase velocity anomalies are associated with remnants of the stalled Guadalupe and Magdalena microplates (Nicholson et al., 1994; Bohannon and Parsons, 1995, see also figure 3.1.1) which ceased to subduct 12 Ma ago. Although these young slab remnants must be very warm, possibly near the solidus, they can still be identified by their higher velocity compared to their surroundings. The low velocities beneath northern Baja California, on the other hand, match the area of the suggested "slab window" (Dickinson and Snyder, 1979b; Severinghaus and Atwater, 1990; Atwater and Stock, 1998), and may be attributed to shallow asthenospheric material in this region. In summary, the phase velocity maps at 30 to 100 s suggest that the upwelling of low velocity asthenospheric material occurs around the northern and southern edge of the microplate remnants under Baja California, to fill the region of melt directly beneath the ridge under the gulf.

The fast-propagation anisotropic directions in northern Baja California change from NW-SE at 50 s to nearly E-W at 100 s. This E-W direction agrees with the fast directions inferred from SKS splitting measurements in southern California (e.g., Polet and Kanamori, 2002) as well as those in northern Baja California (Obrebski et al., 2006), with the exception of the station NE70 which is located at the plate boundary and has an approximately NW-SE direction. At long periods (80–100 s), the fast anisotropic directions in the southern part are not well resolved due to the poor azimuthal ray path coverage and relatively long

wavelengths considered.

3.6 Conclusions

Data of NARS-Baja network allow the determination of high-resolution anisotropic Rayleigh wave phase-velocity maps between 10-100 s. These detailed phase-velocity maps provide new insight into the geodynamics of the Gulf of California region. The fast anisotropic directions of phase velocities with crustal sensitivity (10-14 s) change from predominantly plate-boundary parallel in the north to plate-boundary perpendicular in the south. The transition occurs where the plate boundary changes character from a region of diffuse transtensional continental deformation to a system of oceanic-type spreading centers and transform faults (Nagy and Stock, 2000). The low-velocity anomaly directly beneath the plate boundary and small values for azimuthal anisotropy in the 30 s phase velocity map suggest ridge associated upwelling beneath the gulf. The maps at longer periods (50-100 s) suggest that the low-velocity material flows from below, around the relatively high velocity anomaly corresponding to the location of Guadalupe and Magdalena slab remnants. If this interpretation is correct, it could imply that the slab is effectively attached to the Baja California peninsula and remains in place, possibly extending across the Gulf (see figure 3.4.1, 100s). The region of low velocities in the north matches the area of the proposed slab window beneath northern Baja California.

An intriguing question is whether there is a deep seated (>300 km) source of low-velocity mantle material that feeds the low-velocity features imaged in our phase velocity maps. The results of the model space search show considerable uncertainty in the transition zone, but the phase velocity measurements do favor a low-velocity transition zone. If confirmed by additional data, this could explain the overall low velocities of the region as well the origin of the upwelling beneath the Gulf of California.

3.7 Acknowledgments

We thank the people who initiated and supported the NARS-Baja project: Jeannot Trampert, Arie van Wettum (Utrecht University), Jeroen Ritsema, Robert Clayton (Caltech), Raul Castro, Cecilio Rebollar and Arturo Perez-Vertti (CICESE). Funding for this project was provided by Utrecht University and the Dutch National Science Foundation (grant number NWO-GOA-750.396.01) We thank Jim Gaherty and an anonymous reviewer for their careful reviews.

3.8 Auxiliary material

The auxiliary material contains three figures. The first one show the ray path coverage for the Gulf of California. The second one is a detailed description of the 1-D model space search. The third one is an example of a resolution test. We illustrate the resolution by inverting a synthetic data set created from a model, whose isotropic coefficients are our real inversion result and its 2ψ-anisotropic coefficients are perpendicular to the real inversion result.

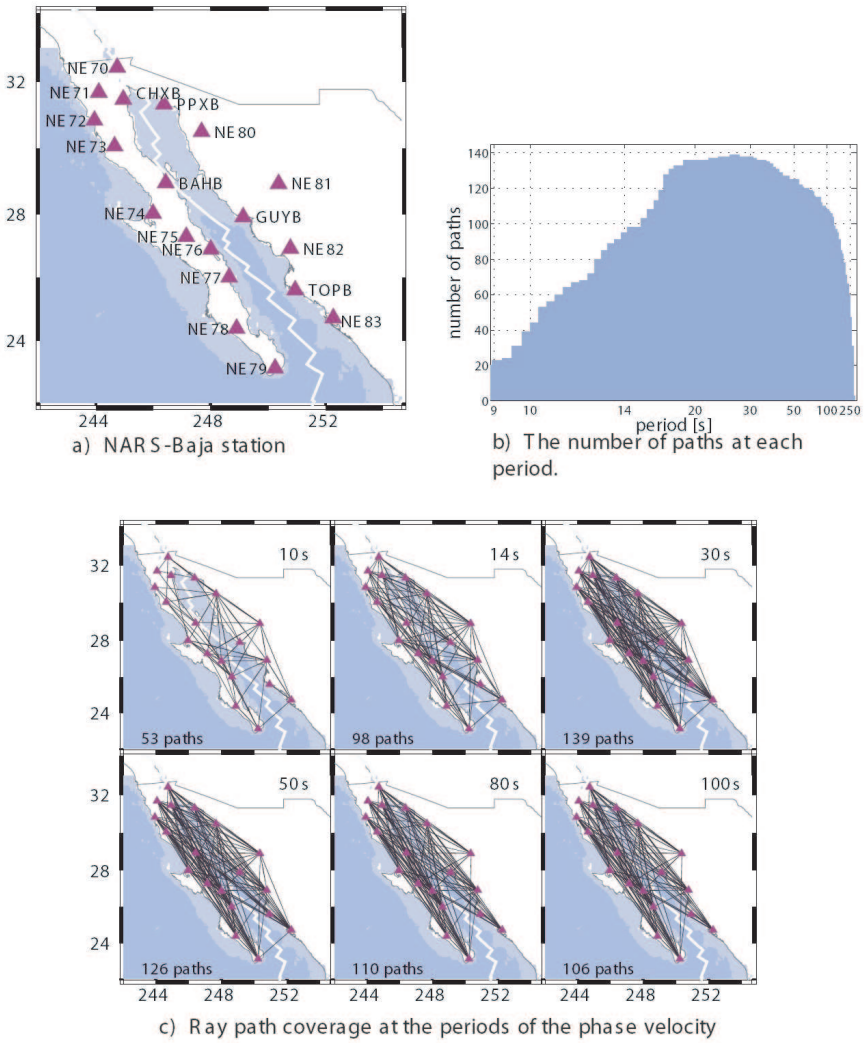

Figure 3.8.1: Ray path coverage for the Gulf of California.

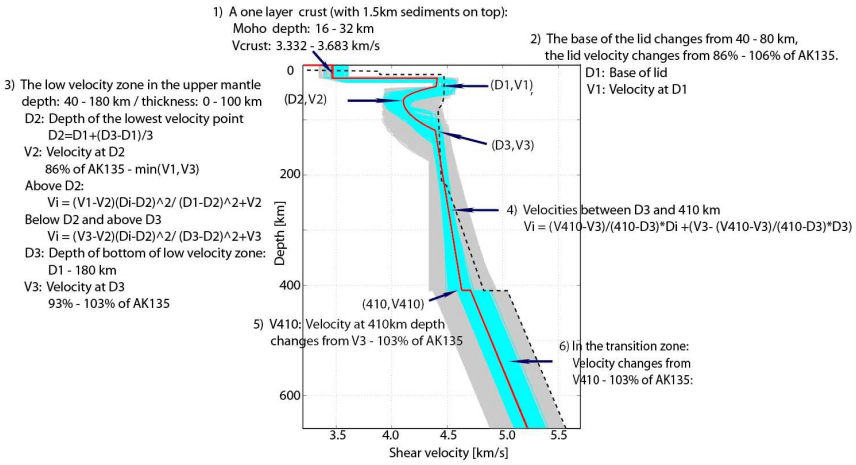

a) The detailed description of the model space parameterization. The gray lines show all models, whose phase velocity curve is within one standard deviation from the mean of the interstation phase velocity measurements. The cyan lines represent the 1000 best fitting models. The best fitting model shown in red. Model AK135 is shown with the black dashed line.

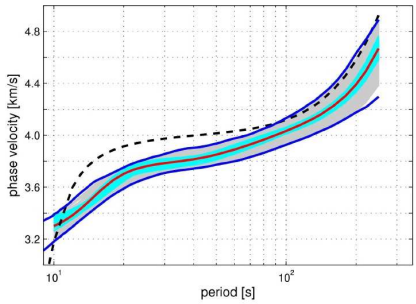

b) Fundamental mode Rayleigh wave phase velocity curves obtained by the 1-D model space search. The blue lines show the one-standard deviation of the phase velocity measurements in this study. The gray lines show all phase velocity curves which fit within the one standard deviation curves.The cyan lines represent the 1000 best fitting curves and the best fitting curve is in red. The phase velocity curve of model AK135 is given by the black dashed line.

Figure 3.8.2: Model space search parameterization

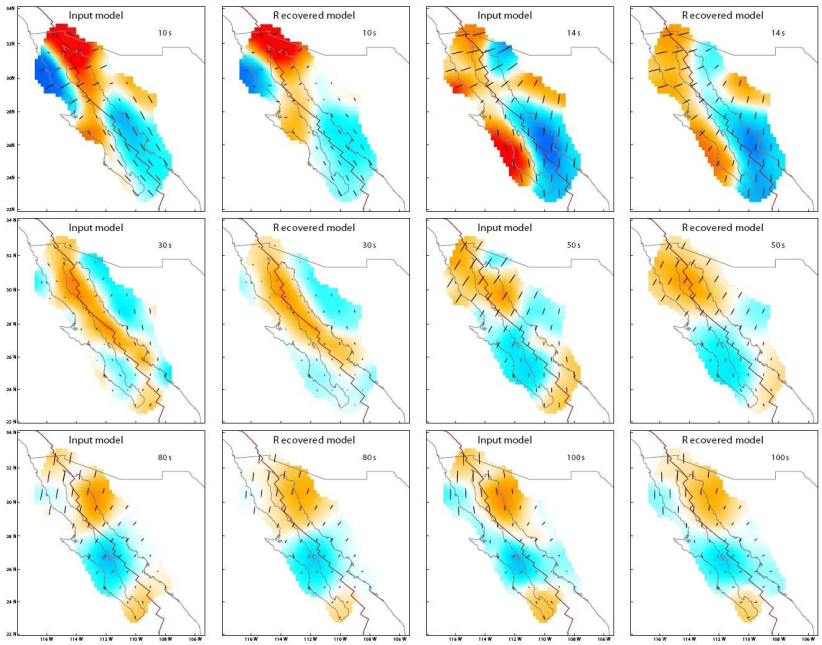

Figure 3.8.3: Resolution test

Chapter 4

3D shear velocity structure beneath the Gulf of California from Rayleigh wave dispersion

Abstract. Active extension in the Gulf of California is characterized by the transition from continental rifting to seafloor spreading. Puzzling variations in the patterns of both tectonics and magmatism are observed along the length of the gulf and are likely to be related to mantle heterogeneity. Regional-scale mantle structure, however, has been difficult to constrain due to the lack of broadband seismic stations in the region. In this study we utilized new data from the deployment of the NARS-Baja array and other networks, and computed a three-dimensional shear-speed model of the upper mantle beneath the region. Applying a combination of cross-correlation analysis and multimode waveform inversion, we measured interstation Rayleigh-wave dispersion for 450 pairs of stations in a broad period range of 9–250 s. We computed phase velocity maps and then inverted the phase-velocity data for shear-speed structure. Our results suggest that the location of the transition from seafloor spreading (South) to continental rifting (North) in the Gulf of California, as well as differences in volcanism across Baja California and the gulf, can be explained by heterogeneity in the upper mantle, in particular by the presence of a slab remnant beneath the south-central part and an absence of such a slab remnant beneath the northern part of the gulf.

This chapter has been submitted for publication by X. Zhang, H. Paulssen S. Lebedev and T. Meier to *Earth and Planetary Science Letters*.

4.1 Introduction

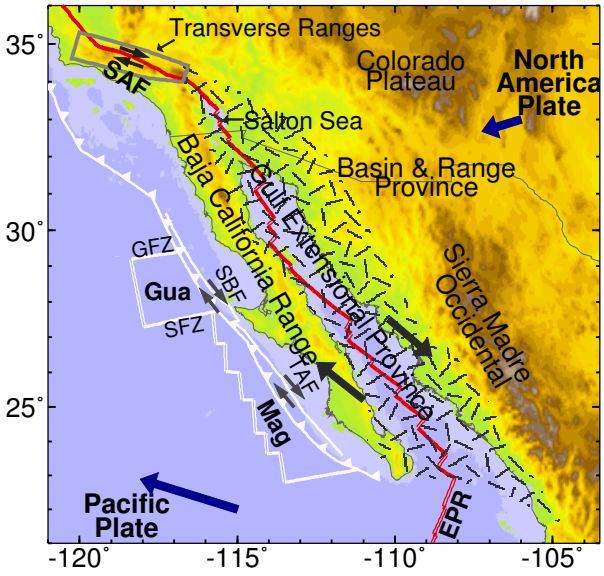

Figure 4.1.1: Tectonic map of the Gulf of California region. The main tectonic provinces are Baja California Range, Gulf Extensional Province (hatched), Transverse Ranges (marked by gray box), Basin and Range Province, Sierra Madre Occidental and Colorado Plateau. Present-day plate boundary is shown as a red line. Inactive plate boundaries are shown as white lines. SAF−San Andreas Fault; EPR−East Pacific Rise; SBF−San Benito Fault; TAF−Tosco Abreojos Fault; GFZ−Guadalupe Fracture Zone; SFZ−Shirley Fracture Zone; Gua−Guadalupe microplate; Mag−Magdalena microplate. Thick arrows indicate plate motions (absolute plate motion in blue, relative plate motion in black) predicted by global plate motion model HS3-NUVEL1A (Gripp and Gordon, 2002).

The Gulf of California, which forms a part of the Pacific-North American plate boundary, is currently extending by means of active rifting. It links the East Pacific Rise and the San Andreas transform fault system, and accommodates a transition from oceanic spreading to continental extension. Because the two types of rifting are juxtaposed, it is one of the few regions where we can investigate the evolution of a rift. It is unclear what causes the differences in the style of rifting between the southern part of the gulf, characterized by oceanic spreading centers and transform faulting (Lonsdale, 1989; Lizarralde et al., 2007), and its northern part, where diffuse continental deformation is occurring (Nagy and Stock, 2000; Oskin and Stock, 2003; González-Fernández et al., 2005). These variations

cannot be explained by variations in the amount of deformation: the South and North have experienced roughly the same amount ($\sim$300 km) of oblique Northwest $-$ Southeast extension since the opening of the gulf at about 6 Ma (Persaud et al., 2003). Moreover, seismic refraction experiments have revealed that basins in the southern and central gulf vary from wide to narrow rifts over small distances ($\sim$200 km) (Lizarralde et al., 2007).

The formation of the Gulf of California is associated with the cessation of subduction of the Farallon plate beneath the North American continent, which occurred approximately 12 Myr ago at the latitudes of central Baja California (Mammerickx and Klitgord, 1982; Lonsdale, 1991; Michaud et al., 2006). When the subduction of the (Farallon-derived) Guadalupe and Magdalena microplates beneath Baja California ceased, the spreading at the mid-ocean ridge segments separating these microplates from the Pacific Plate also ended (Lonsdale, 1991; Stock and Lee, 1994). The Farallon-North American convergence then gave way to Pacific-North American transform motion, accommodated along the San Benito and Tosco-Abreojos faults close to the former trench (Fig. 4.1.1). The extensional component of the new Pacific-North American plate motion was taken up in the back-arc region, east of the Baja Peninsular Range and west of the Sierra Madre Occidental batholiths. This region, known as the Gulf Extensional Province, underwent east-northeast extension from 12 Ma to 6 Ma forming a so-called 'proto-gulf' (Karig and Jensky, 1972; Stock and Hodges, 1989; Henry and Aranda-Gomez, 2000). At approximately 6 Ma, much of the Pacific-North American transform motion along the San Benito and Tosco-Abreojos faults ended, moved inland, and was taken up in the gulf area along transform faults and pull-apart basins (Lonsdale, 1991; Oskin and Stock, 2003). Approximately 90% of the present Pacific-North American plate motion (of 51 mm/yr) is taken up by the northwest extension in the gulf (Plattner et al., 2007).

The magmatism in Baja California and the Gulf of California is closely linked to the tectonic history of the region. The Baja Peninsular Range, a subduction-related calc-alkaline volcanic arc, was formed approximately between 24 and 11 Ma, along a large part of what is currently the Baja California peninsula (Gastil et al., 1979; Hausback, 1984; Sawlan and Smith, 1984). This volcanism was progressively extinguished due to the southward migration of the Pacific-Farallon-North American triple junction, the migration changing the convergent plate boundary into a transform one (e.g., Sawlan, 1991). A slab window, an area without slab beneath the continent, was formed beneath the northern part of Baja California (Dickinson and Snyder, 1979a; Severinghaus and Atwater, 1990; Atwater and Stock, 1998). At 12 Ma, when the Guadalupe and Magdalena microplates

stopped subducting, a change occurred in the magmatism. The calc-alkaline form in central and southern Baja California gave way to other types of magmatism in various volcanic fields. The magmas produced include adakites derived from partial melting of subducted oceanic crust, magnesian andesites from a mantle metasomatized by slab-derived melts, and tholeiitic basalts without a (clear) subduction signature (e.g. Aguillón-Robles et al., 2001; Benoit et al., 2002; Calmus et al., 2003; Conly et al., 2005; Pallares et al., 2007). Tholeiitic lavas have been erupting in the Gulf of California since the initiation of rifting at ca. 12 Ma. Their geochemical signature ranges from tholeiites, typical of an intraplate setting (similar to ocean island basalts and continental flood basalts), to those typical of mature oceanic rifting (mid-ocean ridge basalts) depending on their location and on the stage of rifting at the time of eruption (Sawlan, 1991).

Understanding the evolution of the Gulf of California requires knowledge of processes in the mantle. Mantle temperature and composition control crustal extension through their effects both on flow in the mantle and crust and on magmatism. Seismic studies to date revealed anomalously low mantle shear velocities down to 250 km depth in the entire Gulf of California area (e.g. Lebedev and van der Hilst, 2008; Nettles and Dziewonski, 2008; van der Lee and Frederiksen, 2005). Lack of seismic stations in the area, however, has precluded resolution at the scale comparable to that of the observed variations in the style of rifting and magmatism.

In 2002, the NARS-Baja network of 19 broadband seismic stations was deployed along the perimeter of the Gulf of California (Trampert et al., 2003). Zhang et al. (2007) used the data from this network to measure Rayleigh wave phase velocities and computed azimuthally anisotropic phase-velocity maps for a broad period range. In this study we expand the study area so as to image the structure of the gulf in a larger regional context and invert the phase-velocity maps for three-dimensional shear-velocity structure. Recent results on the crustal structure (Persaud et al., 2007; Lizarralde et al., 2007) provide essential information and are incorporated into the inversion. Our most important result is the finding of a relatively high shear-velocity anomaly in the mantle beneath the central part of the Gulf of California, which we interpret to be a remnant of the subducted Guadalupe slab.

4.2 Method and data

We constrain the shear-velocity structure beneath the Gulf of California with surface-wave dispersion measurements. The interstation fundamental mode Ray-

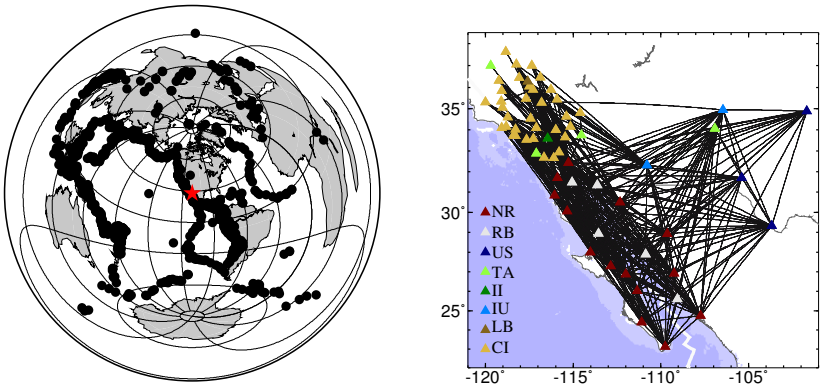

Figure 4.2.1: Events and path distribution. Left: Event distribution. Right: Stations and ray path coverage. NR − NARS, the Network of Autonomously Recording Seismographs, Utrecht University, The Netherlands; RB − RESBAN, the Red Sísmica de Banda Ancha network, CICESE, Mexico; US − National Seismic Network, ANSS Backbone of the USGS/NEIC and USGS/ASL and Earthscope Project of IRIS, USA; TA − USArray Transportable Array, from Earthscope Project, USA; II − IRIS/IDA Network, University of California, Scripps Institute of Oceanography, USA; IU − IRIS/USGS Network, USGS Albuquerque Seismological Laboratory, USA; LB − Leo Brady Network, Sandia National Laboratory, USA; CI − The Caltech Regional Seismic Network, California Institute of Technology, USA.

leigh wave phase velocities were measured using the data recorded at stations of the NARS-Baja network and other stations in the vicinity of the gulf (see Fig. 4.2.1). The phase velocity curves were obtained by two approaches: a cross-correlation implementation of the two-station method as described by Meier et al. (2004) and the automated multimode inversion (AMI) (Lebedev et al., 2005). The two-station method relies on the cross-correlation of vertical component seismograms for events that are located within 7 degrees of the great circle between the two stations. The method involves frequency-dependent filtering and weighting; the phase velocity curve is interactively selected in the frequency domain. The advantage of the method is that it enables measurements at relatively high frequencies (periods down to 10 s and shorter). AMI is a waveform inversion technique that uses mode summation to generate synthetic seismograms and fits the parts of seismograms that are free from noise and scattered waves. Because it is a multi-mode waveform fitting technique, it can separate the relatively long-period fundamental mode from higher mode contamination. The interstation phase velocities are obtained from the dispersion curves of events recorded by stations that share the same great circle path (within 7 degrees). This method is fully automated

and fast, but it usually does not yield the higher frequency parts of the curves due to scattering and stringent selection criteria. We found that the phase velocity curves obtained with the two methods are generally consistent; cross-correlation measurements often extend to higher frequencies, whereas AMI measurements yield lower frequency results. We used cross-correlation measurements for paths across and around the gulf because their higher frequency content provides more constraints on the shallow structure, i.e. the crustal and uppermost mantle structure. AMI was used more extensively for the outer regions with paths to U.S. stations, so that the structure of the gulf could be interpreted in a broader regional setting. The final dispersion curves for each station pair were obtained as averages over many phase velocity curves measured using signal from different events, usually in a number of source regions, recorded at both stations.

The interstation approach is based on the assumption that surface waves propagate along the great-circle path so that the phase velocity curve is representative of the structure between the two stations. However, finite-frequency effects, such as off great-circle propagation, multipathing, and scattering (Prindle and Tanimoto, 2006; Pedersen, 2006), can cause biased estimates of the phase velocities, especially at short periods. This effect is reduced by averaging over phase velocity curves measured using signal from a large number of events. In addition, we checked that the measurements using surface waves arriving from the two opposite propagation directions were in agreement and then discarded biased measurements. For some station pairs systematic differences were observed between the measurements for the two opposite propagation directions at periods shorter than 30 s. We discarded the biased measurements, which are recognized by their higher apparent phase velocities, to obtain more reliable estimates of the dispersion curves (Pedersen, 2006; Zhang et al., 2007).

We analyzed Rayleigh wave data of earthquakes between April 2002 and the end of 2005 with moment magnitudes larger than 5. In total, 11566 vertical component seismograms from 1192 events, recorded at 64 broadband stations, were used for the measurement of 450 interstation phase velocity curves. Fig. 4.2.1 shows the distribution of the events as well as the locations of the stations, together with the path distribution. A representative example, which shows the agreement between the phase velocity measurements obtained by the two approaches, is shown in Fig. 4.2.2. It also illustrates the difference in frequency ranges of the measurements provided by the two different methods. The final phase velocity curves were obtained as the average of at least 8 individual curves with a minimum of 5 measurements per period. For most paths we had more than 20 phase velocity measurements averaged into robust dispersion curves. The

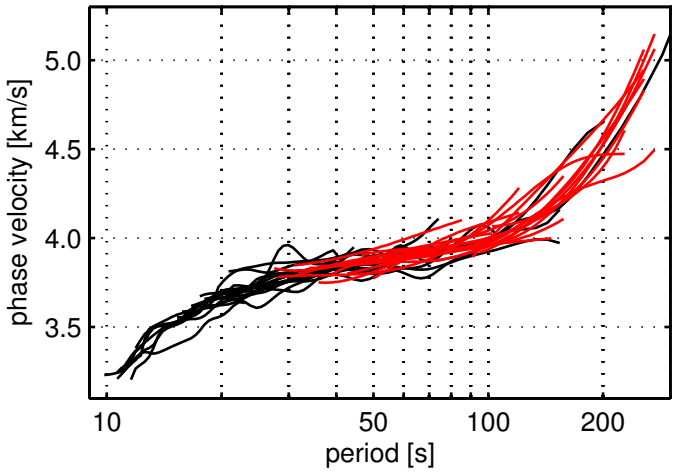

Figure 4.2.2: Phase velocity measurements for the path between station NE70 and station TOV. Red curves are phase velocity measurements obtained by AMI; black curves are phase velocity measurements obtained by the two-station method.

measurements provide sufficient azimuthal coverage to allow the construction of phase velocity maps that include azimuthal anisotropy. Smith and Dahlen (1973) showed that the phase velocity in a layered weak anisotropic medium depends on the propagation direction as

$$\frac{dc}{c}(T,\Psi) = \alpha_0(T)+\alpha_1(T)\cos 2\Psi+\alpha_2(T)\sin 2\Psi+\alpha_3(T)\cos 4\Psi+\alpha_4(T)\sin 4\Psi, \tag{4.2.1}$$

where dc/c is the relative phase velocity perturbation, T the period and Ψ the azimuth of wave propagation. The coefficient α_0 is the isotropic phase velocity perturbation; α_1, α_2, α_3 and α_4 parameterize azimuthal anisotropy. Adopting an approach similar to that of Lebedev and van der Hilst (2008), we inverted our dispersion curves for the isotropic phase velocity perturbations and the four anisotropy coefficients at the knots of a triangular grid with a nearly-uniform spacing of around 100 km and used LSQR (Paige and Saunders, 1982) with smoothing and slight norm damping to compute phase velocity maps at 32 periods, ranging from 9 to 250 s. We found that the isotropic component of the model can be resolved with a higher resolution compared to the anisotropic component, as is usual in anisotropic tomographic inversions (e.g. Lebedev and van der Hilst, 2008). At the shortest ($\leq$13 s) and longest ($\geq$ 100 s) periods the effective smoothing strength

was greater because of the sparser path coverage at these periods.

Fig. 4.2.3 shows the phase-velocity maps including the 2Ψ anisotropy. We have

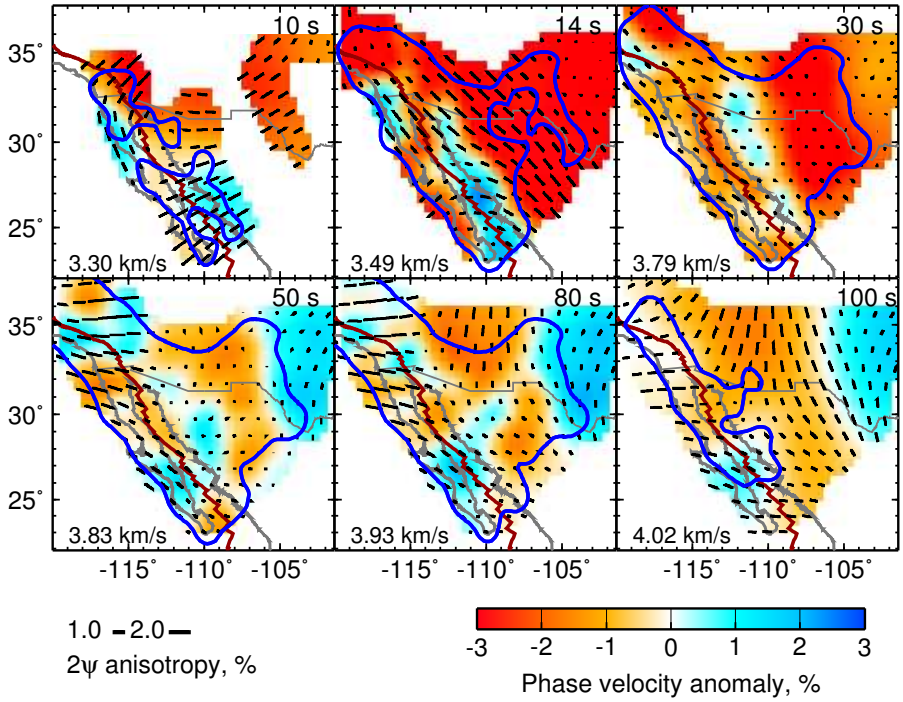

Figure 4.2.3: Rayleigh wave phase velocities anomaly maps. The period is shown in the upper right corner and the reference phase velocity is in the lower left corner of each phase map. The colors indicate the isotropic anomalies and the black bars indicate the fast-propagation directions and the strength of the 2Ψ azimuthal anisotropy. The red line marks the location of the plate boundary. The blue contours delineate the regions of high resolution (see text) in each map.

allowed for 4Ψ heterogeneity in inversions as well but found that the resulting 4Ψ-anisotropy patterns are not robust. We have verified, however, that the isotropic and 2Ψ structure that we retrieve is robust with respect to the amount of the 4Ψ signal allowed in the models by the regularization. The isotropic and 2Ψ structure changed very little with 4Ψ signal strength changing in the range from zero to as high as that of the 2Ψ signal. Having calculated resolution matrices, we defined the well-resolved parts of the region as those containing the grid points with its diagonal elements of the isotropic term of the resolution matrix above 0.1 (Zhang et al., 2007). We also performed several resolution tests to verify the robustness

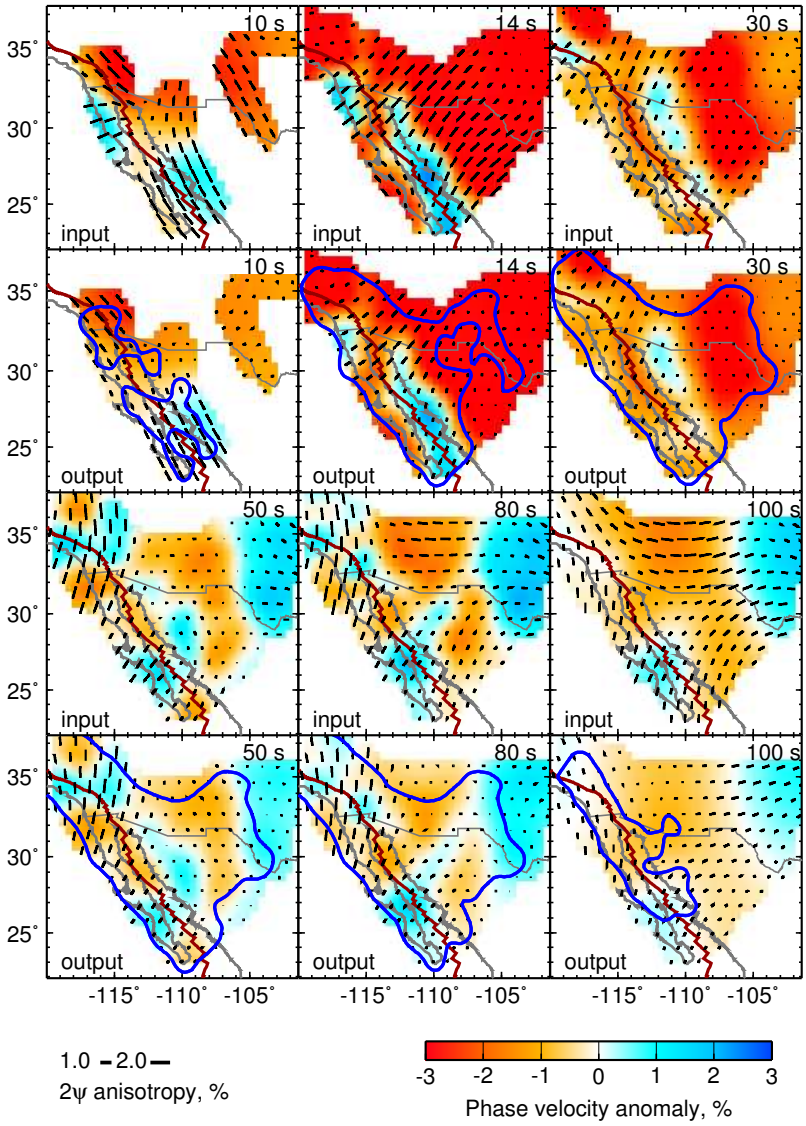

Figure 4.2.4: A resolution test. The resolution test was performed by inverting a synthetic data set created from a model with isotropic coefficients taken from the real inversion result and 2Ψ-anisotropic coefficients such that the anisotropy was with the same strength but with fast-propagation directions perpendicular to those of the inversion result. The blue contours delineate the regions of high resolution (see text) in the original phase velocity maps.

of our results. Fig. 4.2.4 presents one of such tests. The input interstation phase velocities were calculated using models with isotropic terms taken from the actual phase velocity results as in Fig. 4.2.4, and 2Ψ anisotropic terms were such that the anisotropy was of the same strength but with a fast-propagation directions perpendicular to those in the actual phase velocity maps. Fig. 4.2.4 shows that the isotropic structure is reliably recovered and is not affected by the 2Ψ structure. The 2Ψ anisotropic terms are also recovered, except in peripheral regions with poor ray coverage. The accurate recovery of the anisotropic structure in this rigorous test confirms that our azimuthal path coverage is sufficient to constrain phase-velocity heterogeneity in the region of the study. The resolution length for the isotropic structure is estimated at 150–200 km in the best resolved area around the gulf. In order to evaluate the uncertainties of the phase velocity maps, we have calculated the posterior model covariance matrices. The square roots of the diagonal elements of the posterior model covariance matrices can be interpreted as the standard deviations of the estimated model parameters, i.e. the phase velocity perturbations at the grid points (Tarantola, 1987). The uncertainties of the isotropic phase velocity perturbations range from 0.7% (middle periods) to 1.3% (short and long periods). The differences are mainly due to the variations in path coverage and differences in smoothing.

The phase velocity maps of this study are very similar to the phase velocity maps of Zhang et al. (2007) in the region of overlap. The isotropic phase velocity structure of the two studies is nearly identical, although the current study covers a larger area. Slight changes in the anisotropic structure are observed along the peripheral regions of the first study; they are due to the enhanced path coverage in this study.

Having mapped anisotropic heterogeneity, we can isolate the isotropic phase-speed variations that are related to thermal and compositional structure of the mantle. We now invert the isotropic phase velocities for shear-speed structure. For this, the local phase velocity curve is estimated at each of the 182 points of the 100 km spaced geographical grid. These curves are then inverted for 1-D shear-velocity models using a non-linear gradient search method. The 1-D profiles are combined into a 3-D shear-velocity structure. The starting models for the inversions were obtained from the reference model AK135 (Kennett et al., 1995) for the mantle structure, combined with a local crustal structure. We used various sources to infer the local crustal shear velocity and the Moho depth: the Southern California velocity model SCEC-CVM-H (Süss, M. Peter and Shaw, John H., 2003), receiver function studies (Zhu and Kanamori, 2000; Lewis et al., 2001; Persaud et al., 2007), seismic refraction studies (González-Fernández et al.,

2005; Lizarralde et al., 2007), and the global crustal model CRUST 2.0 (Bassin et al., 2000). Locations with various types of constraints on crustal structure are shown in Fig. 4.2.5, together with the resulting map of the crustal thickness that was used in the starting models.

We used 15 free parameters to expand shear speed variations down to 1000 km depth. Of the 15 parameters, one is a boxcar in shape and spans the crustal depth range; 11 are triangular basis functions parameterising mantle structure, with denser sampling at shallower mantle depths; 3 more parameters allow depth perturbations of the Moho, 410-km and 660-km discontinuities. Our phase velocity data have some sensitivity below 300 km, but as the period increases the uncertainty of the measurements increases and the depth resolution decreases. Therefore, we only show the upper 300 km of the model.

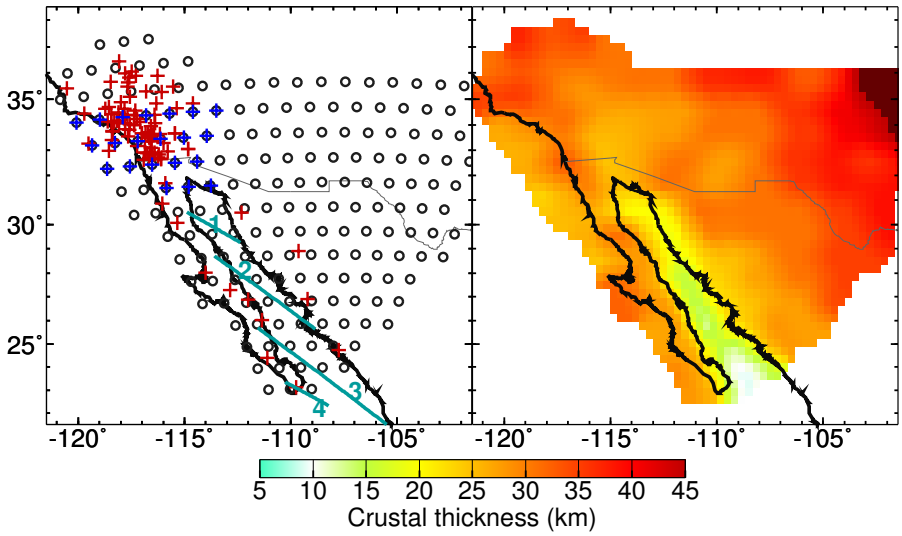

Figure 4.2.5: Construction of the initial crustal model. In the frame on the left, the black circles indicate the grid used to parameterize the inversion; the blue lines indicate seismic reflection lines (González-Fernández et al., 2005; Lizarralde et al., 2007); the red crosses indicate the locations with receiver function data (Zhu and Kanamori, 2000; Lewis et al., 2001; Persaud et al., 2007); the blue crosses indicate the area covered by the SCEC-CVM-H model (Süss, M. Peter and Shaw, John H., 2003). The frame on the right shows the crustal thickness in our initial crustal model based on this data. Where no other information is available, Crust2.0 (Bassin et al., 2000) is adopted.

4.3 Results and interpretation

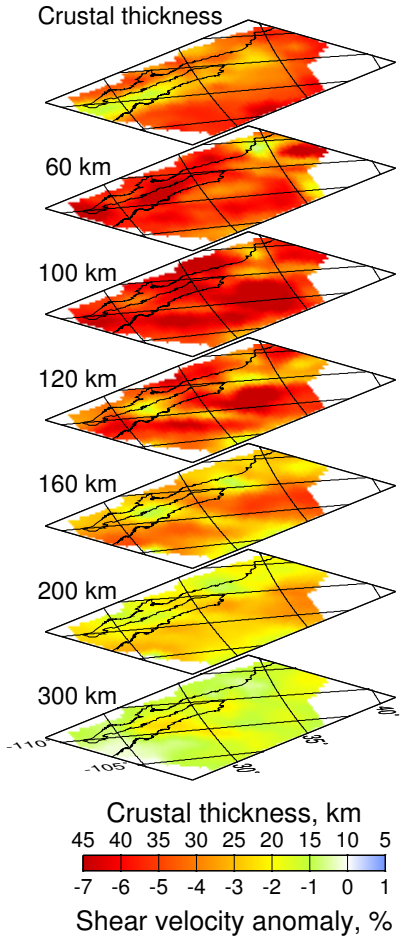

Figure 4.3.1: Maps of the crustal thickness (upper panel), and the shear velocity anomalies relative to the global reference model AK135 (Kennett et al., 1995) at depths of 60, 100, 120, 160, 200, and 300 km.

The results of the inversion are shown by the crustal thickness and the upper mantle shear-speed anomalies relative to the global reference model AK135 (Fig. 4.3.1). Seismic velocities in the upper mantle are much lower than global averages, especially at mantle depths down to 150-200 km. This has been seen previously in tomographic models that included the area (e.g. Lebedev and van der

Hilst, 2008; Nettles and Dziewonski, 2008; van der Lee and Frederiksen, 2005; Godey et al., 2003). The low velocities point to the presence of fluids and/or melt (Goes and van der Lee, 2002). This can be due to the dehydration and/or partial melting from subducted lithosphere, decompression melting because of the opening of a slab window, or partial melting because of high temperatures. Recognizing the existence of very low shear velocities region-wide, we concentrate in the following on the lateral variations within the region.

A striking feature that we identify in this study is a relatively high velocity anomaly beneath the south-central part of the Gulf of California at depths between roughly 120 and 160 km (Fig. 4.3.1). We illustrate the difference in shear velocity beneath the northern and southern gulf more closely by comparing two selected grid points in these areas. Fig. 4.3.2 shows their locations, phase velocity curves and 1-D velocity structures. Note that the phase velocity curves do not overlap within the error bars in the 60-90 s period range. The shear velocity structure for the northern grid point shows a thin lid overlying a pronounced low velocity layer. Except for the thin lid this velocity structure is very similar to the average shear velocity structure beneath southern California obtained by Yang and Forsyth (2006). The shear velocity structure for the southern grid point does not show a clear lid and has significantly higher velocities in the 100-200 km depth range. The absence of the lid may be related to the fact that this grid point is located right above the active rift. More important however are the relatively high velocities in the 100-200 km depth range (albeit smaller than AK135). These velocities are not only several percent higher than those of the northern grid point, but also compared to the shear velocities beneath the East Pacific Rise (Webb and Forsyth, 1998).

Errors in the crustal thickness may affect the inferred velocity structure. However, the Moho depth in the gulf is well constrained from seismic refraction experiments (see Fig.4.2.5). Since we further allow the crustal thickness to vary in the inversion, we believe that the estimated velocity structure is not significantly affected by Moho depth uncertainties, and certainly not at depths larger than 100 km.

We interpret the high velocity anomaly in the 120-160 km depth range beneath the south-central gulf as a remnant slab fragment, for two reasons: (1) it is a relatively high shear-velocity anomaly in an area of former microplate subduction, and (2) volcanism in the region, above the anomaly, shows a clear slab signature (Pallares et al., 2007; Bellon et al., 2006; Conly et al., 2005). The crucial point for the tectonic interpretation of this feature is the origin of the slab. Although its current location is just east of the unsubducted portion of the Mag-

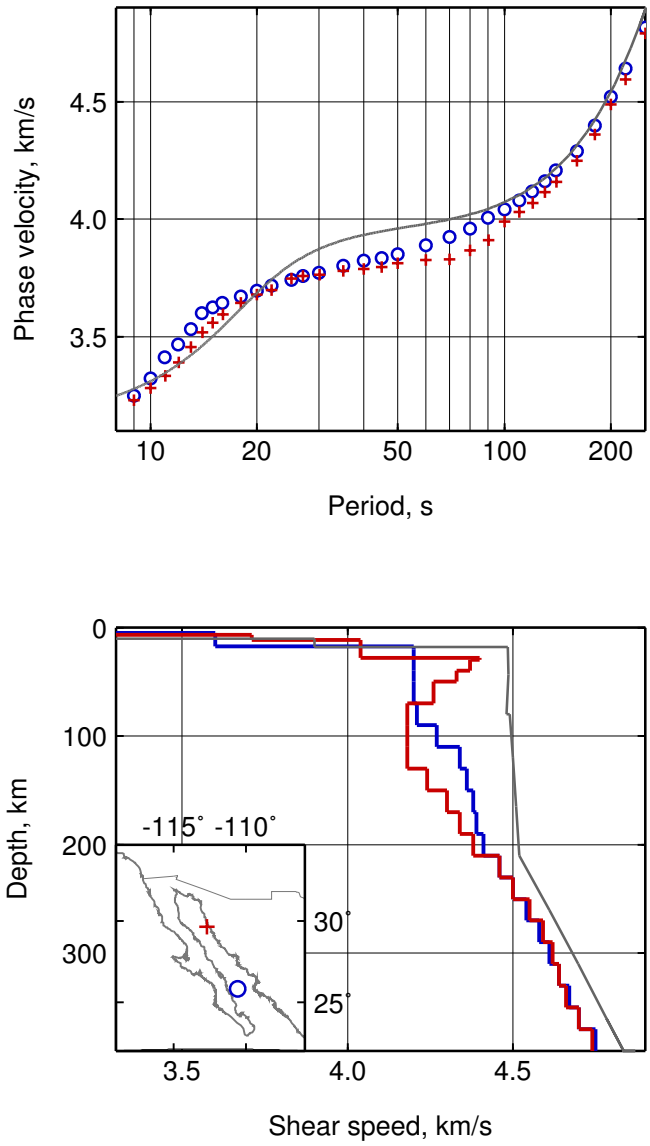

Figure 4.3.2: Phase velocity curves (upper panel) and the inverted shear velocity structures (lower panel) at two grid points. The locations of the two grid points are depicted in the lower left corner of the lower panel. The gray lines are for global reference model AK135 (Kennett et al., 1995).

dalena microplate we attribute this anomaly to the Guadalupe microplate. The part of the latter that last subducted comprised older and, therefore, colder oceanic lithosphere and can be expected to be more visible in the shear-speed image. The North-South extent of the anomaly matches the width of the Guadalupe plate between the Guadalupe and Shirley fracture zones (Fig. 4.1.1). Moreover, according to plate-tectonic reconstructions, at the time when the Guadalupe microplate ceased to subduct its location relative to Baja California was where we currently find the high velocity anomaly (Lonsdale, 1991; Stock and Lee, 1994).

Our conclusion that the anomaly is a remnant of the Guadalupe slab has important consequences. It implies that in the last 12 Ma this slab remnant has not moved noticeably relative to the overlying Baja California, whereas the unsubducted part of the Guadalupe microplate moved together with the Pacific plate roughly 300 km to the northwest (Spencer and Normark, 1989; Oskin and Stock, 2003) to its present location (Fig. 4.1.1). We propose that the Guadalupe slab broke off at depth beneath the current location of the Gulf of California, i.e. at the eastern margin of the relative high velocity anomaly. Because of the removal of the slab pull force, subduction stopped and spreading ceased. The western part of the Guadalupe oceanic plate was effectively captured by the Pacific Plate, and the Guadalupe-North American relative movement became the same as the Pacific-North American movement, of a predominantly strike-slip character. This new Pacific-North American transcurrent motion was taken up by San Benito and Tosco-Abreojos transform faults that developed next to the (inactive) trench. These faults must have cut through the subducted remnant of Guadalupe lithosphere that was now stalled in the uppermost mantle beneath Baja California, leaving the remnant completely detached from its origin.

Our interpretation of the origin of this shear-velocity anomaly and the tectonic reconstruction are further supported by the analysis of magmatism in Baja California and the gulf. Much of the volcanism in Baja California since 12 Ma occurred in fields at latitudes between 26° and 27.5°N. Some of the lavas have been associated with partial melting of oceanic crust (adakites), others with a mantle metasomatized by slab-derived aqueous fluids (andesites), and others yet were identified as tholeiitic basalts similar to mid-ocean ridge basalts (MORBs) or ocean island basalts (OIBs) (e.g., Sawlan, 1991; Conly et al., 2005; Pallares et al., 2007). The adakites are best accounted for by melting at the edges of the slab remnant, whereas the andesites originate from the supra-slab mantle metasomatized by slab melts. The tholeiites, on the other hand, are produced in regions without a slab remnant. The limited lateral extend of the slab remnant explains the close proximity of these types of volcanism in central Baja California.

We note further, that our results show very low shear velocities in the central region of the gulf at depths of approximately 60 km. This is the location above the high-velocity anomaly, so that these low velocities are most likely associated to supra-slab mantle metasomatized by slab-derived aqueous fluids and melts. Based on volcanic evidence and tectonic reconstructions, various geometries of subducted slab fragments and asthenospheric slab windows have been proposed in previous studies (Pallares et al., 2007; Fletcher et al., 2007; Conly et al., 2005; Ferrari, 2004; Benoit et al., 2002). None of the scenarios, however, proposed a slab remnant that is localized in the central region of the Gulf as is found in our tomographic results.

Through its effect on magmatism, the remnant slab may also control the character of the rifting—reflected, in particular, in the thickness of the crust. The crust in our model is thinner in the southern part of the gulf than in the northern part, which is in agreement with previous studies (Lizarralde et al., 2007; González-Fernández et al., 2005). More importantly, we find a conspicuous geographical correspondence between the northernmost extent of the thin-crusted portion of the gulf and the northern boundary of the slab remnant (relatively high-velocity feature) in the central gulf. The variations in crustal thickness appear to correspond to the variations in volcanism, and the variations of both types may be related to the change from the presence of the slab remnant in the south-central part to its absence in the northern part of the gulf. The Guaymas basin (along refraction line 2 in Fig. 4.2.5), located above the relatively high velocity feature, is a narrow rift with very high magma production since the opening of the gulf (Lizarralde et al., 2007). This is anomalous because the primary style of rifting in the rest of the gulf is close to that of a wide rift with low melt generation (Lizarralde et al., 2007; González-Fernández et al., 2005). The more southerly Alarcon basin (along refraction line 3 in Fig. 4.2.5), for instance, experienced ca. 350 km of continental extension before seafloor spreading started 2-3 Myr ago, probably fed by the magmatic source from the East Pacific Rise (Lizarralde et al., 2007). The voluminous magmatism in the Guaymas basin since its opening (Batiza, 1978; Lizarralde et al., 2007) can be explained by the slab break-off and the presence of the stalled slab fragment which enriched the mantle. Furthermore, magmatic weakening of the lithosphere by the stalled slab fragment may have contributed and resulted in the sea-floor spreading in the central Gulf of California, occurring in contrast to the diffuse extension just to the North (González-Fernández et al., 2005; Lizarralde et al., 2007).

Our results also show other anomalies such as a thin crust in the Salton Sea area and relatively fast shear-velocity anomalies beneath the Transverse Ranges.

These features have been found in previous surface wave studies that focused on southern California (Yang and Forsyth, 2006; Prindle and Tanimoto, 2006). The thin crust of the Salton Sea is associated with lithospheric extension; it defines the northern part of the Gulf Extensional Province. The fast anomalies beneath the Transverse Ranges have been related to lithospheric down-welling.

4.4 Conclusion

The Gulf of California exhibits different stages of the transition from continental rifting to seafloor spreading. Its northern part is characterized by diffuse continental extension, whereas the southern part contains oceanic spreading centers and transform faults. We determined the crustal and upper mantle shear-speed structure using Rayleigh wave dispersion measurements. Measured phase-velocity curves were inverted for phase velocity maps which were then inverted for shear-speed structure. The high resolution of our tomography has been enabled by the newly available data, largely from the stations of the NARS-Baja network deployed around the gulf.

The shear-speed model shows a relatively fast anomaly in the upper mantle with overall low shear velocities. The anomaly, which is well-resolved in the central part of the gulf at depths approximately between 120 and 160 km, is interpreted as a remnant of the subducted Guadalupe plate, a Farallon-derived microplate. The current location of the anomaly implies that the slab fragment has been stalled beneath Baja California since 12 Ma, and strongly influenced the evolution of the gulf. Its presence, in particular, can account for the variability in the magmatism in central Baja California.

We attribute the location of the transition from continental extension (North) to oceanic spreading (South) in the Gulf of California to the location of the slab remnant, present beneath the central-southern part and absent beneath the northern part. It is therefore concluded that the complex tectonics related to the cessation of Farallon subduction has governed the evolution of the gulf.

4.5 Acknowledgments

We thank the people who supported the NARS-Baja project: Jeannot Trampert, Arie van Wettum (Utrecht University), Robert Clayton (Caltech), Raul Castro and Arturo Perez-Vertti (CICESE). Funding for this project was provided by the Utrecht University, the Dutch National Science Foundation (grant number NWO-GOA-750.396.01) and the U.S. National Science Foundation (grant number EAR-

0111650 of the MARGINS program). Maintenance of the CICESE broadband stations is partly funded by CONACYT project 37038-T. The data used in this research were partly obtained from the IRIS Data Management center. We'd like to thank the following networks: the Caltech Regional Seismic Network(CI) from California Institute of Technology; the IRIS/IDA Network(II) from University of California, Scripps Institute of Oceanography; the IRIS/USGS Network(IU) from USGS Albuquerque Seismological Laboratory; the Leo Brady Network (LB) from Sandia National Laboratory; the USArray Transportable Array (TA) from Earthscope Project; the US National Seismic Network (US) from ANSS Backbone of the USGS/NEIC and USGS/ASL and Earthscope Project of IRIS. We thank Helle Pedersen and an anonymous reviewer for their careful reviews. Their suggestions have improved this manuscript.

Chapter 5

3D radial anisotropic shear velocity structure beneath the Gulf of California

Abstract We inverted fundamental mode Love and Rayleigh wave dispersion data for a radially anisotropic shear wave velocity model for the Gulf of California. The inverted data set consists of 5292 vertical and 2077 transverse component high quality surface waveforms. They are recorded with the NARS-Baja broad-band seismic network which is deployed in the vicinity of the Gulf of California since 2002. Our results confirm the pronounced low shear velocities in the upper mantle found by previous global and regional studies, as well as the presence a relatively high velocity structure beneath the central-southern Gulf. The radial anisotropy $\xi = \frac{V_{SH}^2}{V_{SV}^2}$ in the shallow mantle ($\leq$ 100 km) shows a clear difference between the central-southern Gulf, above the high velocity anomaly, and the regions of the northern and southern Gulf. The region of low ξ beneath the northern Gulf can be interpreted as a region of less horizontal flow, or relatively more vertical flow, corresponding to a slab window in the mantle. The region with a higher ξ is associated with the region above a slab remnant. This interpretation would hold for A- and E-types of olivine fabrics which are supposedly the mostly likely deformation fabrics under these mantle conditions.

Key words: Gulf of California , radial anisotropy, surface waves, mantle flow, upper mantle

5.1 Introduction

Since the 1960's, evidence for radial anisotropy has been discovered by the incompatibility of Love and Rayleigh wave dispersion (e.g., Anderson, 1961; McEvilly, 1964; Schlue and Knopoff, 1978). It was included in the global 1-D reference Earth model PREM (Dziewonski and Anderson, 1981), and since then a large number of global and regional studies have mapped radial anisotropy (e.g., Gung et al., 2003; Beghein et al., 2006; Maggi et al., 2006; Panning and Romanowicz, 2006; Sebai et al., 2002; Marone et al., 2007; Visser et al., 2008). The source of anisotropy in the mantle is usually assumed to be the alignment (lattice preferred orientation or LPO) of intrinsically anisotropic minerals under strain in the mantle (e.g., Montagner, 1998; Karato, 1998; Karato et al., 2008). Because anisotropy is an indicator of mantle strain and flow, it is able to improve our understanding of the dynamics of the mantle.

The Gulf of California (GofC), as part of the Pacific - North American plate boundary, is the ideal place to investigate upper mantle dynamics in a continental rifting area by means of high resolution 3-D anisotropic tomography. In particular, geophysical questions such as the relation of upper mantle anisotropy to present day asthenospheric flow and/or past tectonic events, the nature and strength of the lithosphere/asthenosphere coupling and the driving mechanisms of rifting can be explored.

The plate boundary in the GofC is composed of en échelon basins connected by long transform faults. It links the San Andreas strike-slip fault system in California in the North to the oceanic spreading system of the East Pacific Rise in the South. Together, these three parts form the Pacific-North American plate boundary. The plate boundary development in the GofC is a result of tectonic interaction between the Pacific, Farallon and North American plates. At ca. 28 Ma, the Pacific-Farallon spreading ridge reached the trench at the subduction zone. As a consequence, the Pacific plate made direct contact with the North American plate and two triple junctions formed: a transform-transform-trench triple junction, the Mendocino triple junction which migrated to the Northwest, and a ridge-transform-trench triple junction, the Rivera triple junction, which moved to the Southeast (e.g., Lonsdale, 1991; Nicholson et al., 1994; Bohannon and Parsons, 1995; Atwater and Stock, 1998).

With time the Rivera triple junction migrated southward and the intervening Farallon plate fragmented into various microplates. Two of these, the Guadalupe and the Magdalena microplates, have been identified offshore west Baja Peninsula (Fig. 1.1.1). Their subduction beneath Baja California ceased ca. 12 Myr ago. The Pacific-North American plate motion was then largely accommodated along

the right-lateral San Benito and Tosco-Abreojos fault zones parallel to the fossil trench. The extensional component of the motion was taken up by back-arc extension, forming a proto-Gulf between two more rigid blocks, the Baja California Range to the west and the Sierra Madre Occidental to the east. Over time the relative plate motion was increasingly accommodated by strike-slip motion and extension in the proto-Gulf area. This area became the Gulf Extensional Province. At approximately 6 Ma, most of the Pacific-North American transform motion along the San Benito and Tosco-Abreojos faults ended, moved inland, and was accommodated in the proto-Gulf area along transform faults and pull-apart basins (e.g., Lonsdale, 1991; Oskin and Stock, 2003). Consequently, the GofC started to open. At present, approximately 90% of the Pacific-North American plate motion (of 51 mm/yr) is taken up by the Northwest extension in the Gulf (Plattner et al., 2007).

The GofC is currently extending by means of rifting. As a transition between the East Pacific Rise and the San Andreas transform fault system, the plate boundary in the GofC changes its character from an oceanic-type spreading centre and transform fault system in the South to a region of diffuse continental extensional deformation in the North (Nagy and Stock, 2000; González-Fernández et al., 2005; Lizarralde et al., 2007). In this study, we aimed to create a 3D radially anisotropic shear wave velocity model of the GofC by using Love and Rayleigh wave dispersion data. The constraints on the mantle structure and flow pattern provide insight into the tectonics.

5.2 Method and data

We constructed a radially anisotropic shear velocity model beneath the GofC by a three stage inversion. In the first stage, the phase velocities of the fundamental mode Love and Rayleigh waves were measured between the station pairs of the NARS-Baja network. In the second step the measured dispersion curves were inverted for 2-D phase velocity maps at different periods for the two wave-types. As a result, we estimate at each geographical location the local Love and Rayleigh wave phase velocity curves. In the third step, these dispersion curves were inverted for radially anisotropic 1-D shear velocity models, and the results were combined into a 3-D radially anisotropic shear-velocity structure.

5.2.1 Interstation phase velocity measurements

In the first stage, the phase velocities of the fundamental mode Love and Rayleigh wave were measured for paths between the stations of the NARS-Baja network

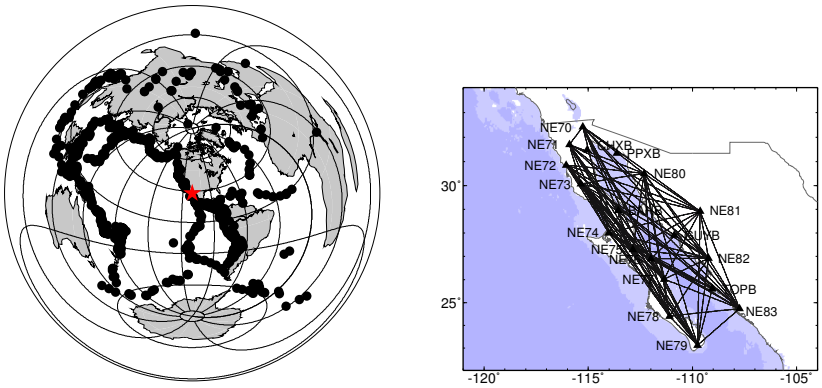

Figure 5.2.1: Events and path distribution. Left: Event distribution. Right: Stations and interstation path coverage.

across and around the Gulf (see Fig. 5.2.1). The interstation approach is based on the assumption that surface waves propagate along the great-circle path so that the dispersion curves are representative of the structure between the two stations. The two-station method in the frequency domain was introduced first by Sato (1955). Since then it has been extensively used to determine surface wave dispersion curves. A review of early works can be found in Knopoff (1972). From the cross-correlation function of two vertical (or transverse) component seismograms, excited by the same event recorded at two stations with the same back azimuth, one can find the phase velocity c at frequency ω

$$c(\omega) \quad = \quad \frac{\omega(\Delta_1 - \Delta_2)}{arctan\left\{\Im[\Phi(\omega)]/\Re[\Phi(\omega)]\right\} + 2n\pi}, \tag{5.2.1}$$

where $\Phi(\omega)$ is the cross-correlation function of the two seismograms at frequency ω, $\Re[\Phi(\omega)]$ and $\Im[\Phi(\omega)]$ are the real and imaginary components of $\Phi(\omega)$ respectively. Δ_1 and Δ_2 are the epicentral distances and the indices 1 and 2 refer to the two stations. Because of the $2\pi-$ambiguity of the arctan function, the phase velocity is estimated from an array of curves for different values of n, where n belongs to the ensemble of integers.

Following the approach of Meier et al. (2004), we measured phase velocities of fundamental mode Love waves by cross-correlating transverse-component displacement data from two stations. The displacement fields are excited by events located within 7 degrees of the great circle between the two stations. The method involves frequency-dependent filtering and weighting, and the phase velocity curve is interactively selected in the frequency domain. For each path, the final phase

velocity curve was obtained as the average of at least 8 individual curves with a minimum of 4 measurements per period. However, in most cases we had more than 20 phase velocity curves per path. The uncertainty was taken as $\pm$ one standard deviation from the average of the ensemble of curves.

The inverted data set consists of 2077 transverse component surface waveforms, excited by 461 earthquakes with moment magnitudes larger than 5. They were recorded at the 19 NARS-Baja stations around the GofC. In total, we obtained 92 interstation phase velocity dispersion curves of the fundamental mode Love wave. Fig. 5.2.1 shows the distribution of the events as well as the locations of the stations and path distribution. The Rayleigh wave dispersion curves for the same paths were taken from chapter 4. The Rayleigh wave data set includes 5292 vertical component waveforms of 858 earthquakes with a moment magnitude larger than 5. Fig 5.2.2 illustrates the number of paths at different periods of the interstation phase velocity measurements. Although the same paths were selected for the two data sets, the path distribution of the Love and Rayleigh wave measurements varies for the different periods. At longer periods, there are more Rayleigh than Love wave measurements. This is due to the greater difficulty in measuring Love waves at long periods and the higher noise level on the transverse component seismograms. The reduced Love wave path coverage at long periods limits the resolution of the shear velocity model at larger depths.

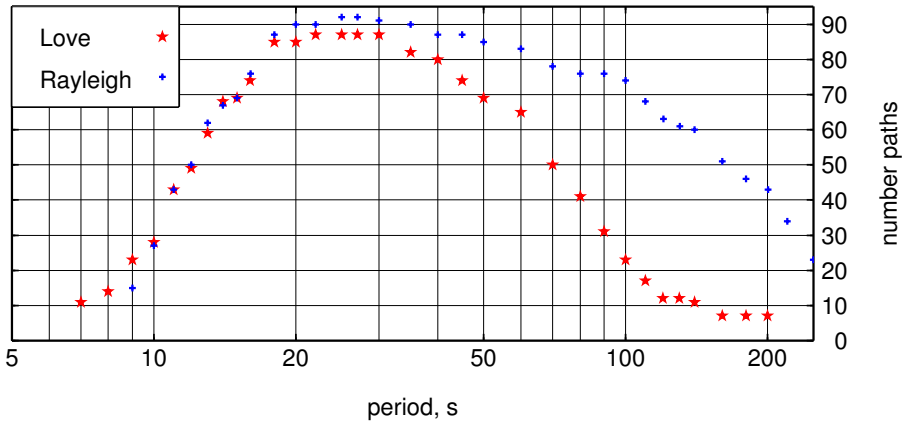

Figure 5.2.2: Number of Love and Rayleigh wave paths at different periods for the interstation phase velocity measurements

5.2.2 Love and Rayleigh phase velocity structures

In the second stage, the 92 interstation phase velocity measurements are inverted into a set of phase velocity maps that include azimuthal anisotropy. The inversion of a set of interstation phase velocity dispersion curves to phase velocity maps at individual periods is a linear problem. At a given period, the interstation phase velocity perturbation d for path i with a azimuth ψ is

$$\begin{aligned} d_i &= \sum_{j=1}^{m} K_{ij} dC_j \\ &= \sum_{j=1}^{m} K_{ij} (\delta C_{(iso)j} + \delta A_{(2\psi)j} \cos 2\psi + \delta B_{(2\psi)j} \sin 2\psi \\ &\qquad + \delta A_{(4\psi)j} \cos 4\psi + \delta B_{(4\psi)j} \sin 4\psi), \end{aligned} \tag{5.2.2}$$

where K_{ij} is the weight of grid point j to path i, determined by the relative position between the grid point and the path (Lebedev and van der Hilst, 2008), and m

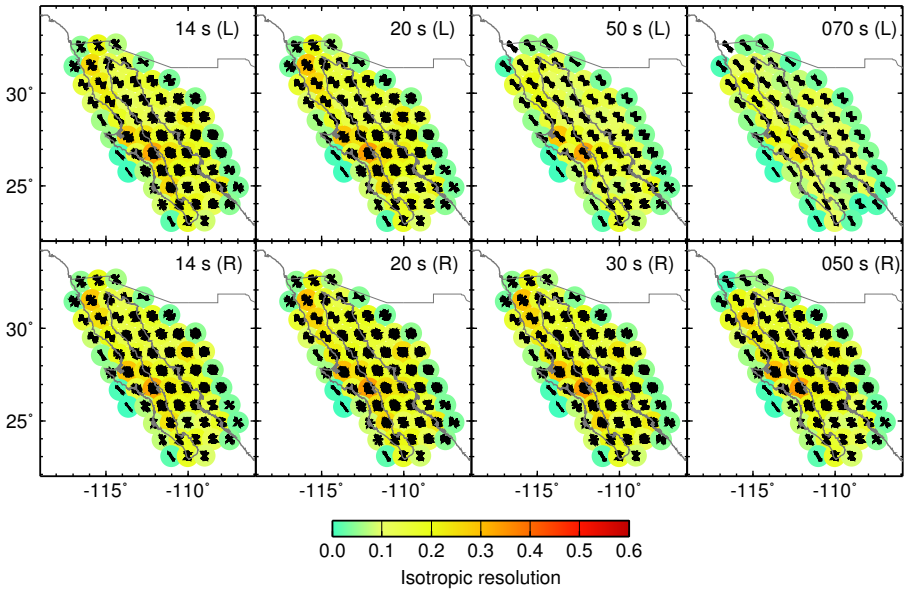

Figure 5.2.3: Resolution maps. The round dots indicate the grid points used to parameterize the inversion. The colour marks the strength of the diagonal elements of the isotropic term of the resolution matrix. The black bars indicate the azimuth distribution of the paths contributing to the phase velocity at each grid point.

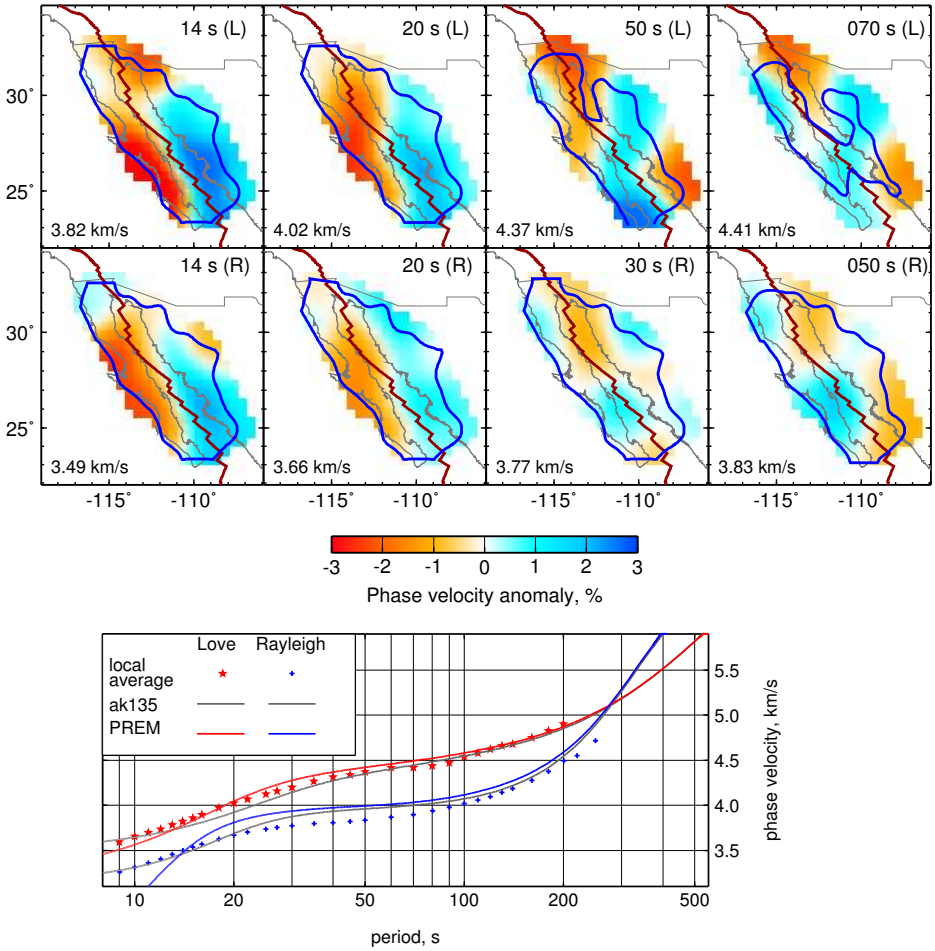

Figure 5.2.4: Phase velocity structure. Top: tomographic images of Love and Rayleigh wave phase velocities at different periods. The period is shown in the upper right corner and the reference phase velocity is in the lower left corner of each phase map. The colours indicate the isotropic anomalies. The purple line marks the location of the plate boundary. The solid blue lines delineate the regions of high resolution (with their diagonal elements of the isotropic term of the resolution matrix above 0.1). Bottom: the reference Love- and Rayleigh-phase velocities, i.e. the local average of the phase velocities at different periods. The Love and Rayleigh phase velocity curves of PREM and AK135 are shown for reference.

is the number of grid points on the phase velocity map. For each geographical grid point, the phase velocity perturbations are described by five parameters (Smith and Dahlen, 1973): the coefficient $\delta C_{(iso)j}$ is the isotropic phase velocity perturbation; $\delta A_{(2\psi)j}$, $\delta B_{(2\psi)j}$, $\delta A_{(4\psi)j}$ and $\delta B_{(4\psi)j}$ parameterize azimuthal anisotropy. In this study we adopted a similar approach to that of Lebedev and van der Hilst (2008) to solve this linear inversion problem. The five phase velocity perturbation coefficients, at the knots of a triangular grid with a nearly-uniform spacing of 100 km, were inverted by using LSQR (Paige and Saunders, 1982) with smoothing and slight norm damping.

The regularization of the inversion, i.e. the smoothing and damping, influences the results of the inversions. The choice of the smoothing and damping factors, however, is made subjectively. The same regularization was used for all periods to avoid lateral variations in the phase velocity maps caused by variations in damping and smoothing. We performed various resolution tests to analyze the robustness of the results. We found that the isotropic components of the Love and Rayleigh wave models were much better resolved than the anisotropic components. Especially for the Love waves at longer periods, due to the poorer azimuthal coverage, the anisotropic terms were poorly resolved. Fig. 5.2.3 gives an indication of the resolution of the final phase velocity maps. The resolution of the isotropic term is represented by the value of its diagonal element in the resolution matrix. The direction of the paths at each grid point is shown to illustrate the coverage for the anisotropic terms. Fig. 5.2.3 shows that, except in the peripheral regions with poor ray coverage, the isotropic structure is reliably resolved, whereas the azimuthal path distributions are in general not ideal. We further calculated resolution matrices for inversions with and without the anisotropic terms and found that the isotropic terms were scarcely affected by the inclusion of the anisotropic terms. The resolution length for the isotropic structure is estimated to be 150–200 km in the best resolved area, i.e. in the Gulf. Fig. 5.2.4 shows the Love- and Rayleigh-wave phase-velocity maps of the inversion.

5.2.3 Depth inversion

In the last and third stage of the inversion, the isotropic parts of the phase velocity models were used to construct a radially anisotropic shear-wave structure. For this, the local Love- and Rayleigh-wave phase velocity curves were estimated at each of the 63 points of the 100 km spaced geographical grid. These curves were then inverted for 1-D radially anisotropic shear-velocity models, within a 0.5% uncertainty, using a non-linear gradient search method. Eventually, the 1-D models were combined into a 3-D shear-velocity structure.

A transversely isotropic medium with a vertical axis of symmetry is described by density ρ and the five Love coefficients (A, C, F, L and N) (Love, 1927). However, from horizontally traveling Love waves we can only reliably estimate the horizontally polarized shear velocity ($V_{SH} = \sqrt{N/\rho}$), and from Rayleigh waves, the vertically polarized shear velocity ($V_{SV} = \sqrt{L/\rho}$).

Taking the isotropic terms of the phase velocities from the second stage, we performed a point-by-point depth inversion to constrain the radially anisotropic shear velocity structure. For each geographical grid point, we inverted Love- and Rayleigh-wave dispersion simultaneously for average shear wave speed $V_{S(avg)} = (V_{SH} + V_{SV})/2$ and the amount of radial anisotropy $V_{SH} - V_{SV}$. The inversion is performed by a non-linear optimisation; in each iteration, Love and Rayleigh wave phase velocities are recomputed from the perturbed shear velocity model. The compressional wave speed V_P was assumed to be isotropic with its perturbation coupled to $V_{S(avg)}$ as $\frac{dlnV_{S(avg)}}{dlnV_P} = 1.7$. The density was kept constant in the inversion.

Combining the velocity model AK135 (Kennett et al., 1995) in the mantle and a priori crustal model in the GofC region (see chapter 4), we built the 1-D starting models for each grid point. We used 15 free parameters to expand shear wave speed variations down to a depth of 1000 km (see Fig. 2.10.2). Of the 15 parameters, one is boxcar in shape and spans the crust; 11 are triangular basis functions parameterising mantle structure, with denser sampling at shallower mantle depths; 3 more parameters allow depth perturbations of the Moho, 410-km and 660-km discontinuities.

It is important to have a good estimate of the Moho depth and to allow the depth to vary, because an incorrect Moho depth can bias the crustal and uppermost mantle structure and result in improper estimates of radial anisotropy (Levshin and Ratnikova, 1984). The Moho depths of the starting models were generally well-constrained from a local velocity model (Süss, M. Peter and Shaw, John H., 2003), seismic refraction lines (González-Fernández et al., 2005; Lizarralde et al., 2007), receiver functions (Lewis et al., 2001; Persaud et al., 2007), as well as crustal model CRUST2.0 (Bassin et al., 2000). Details of the initial crustal model construction can be found in chapter 4 (Fig. 4.2.5).

For each grid point, there are more radially anisotropic shear velocity models which fit the Love and Rayleigh dispersion data within the 0.5% uncertainty. The model obtained from the inversion, i.e. the amplitude of the average shear wave speed and the amount of radial anisotropy, depends largely on the damping. We tested different amounts of damping. The final model presented here is conservative on radial anisotropy: the isotropic-average anomaly and the amount

of anisotropy are both damped towards zero, but the latter is damped three times stronger than the former. The amount of radial anisotropy was therefore forced to be small.

5.3 Radially anisotropic shear-velocity structure

We present the inverted radially anisotropic shear-velocity structure in Fig. 5.3.1 by two parameters, different from those used in the inversion. These are the perturbations in the isotropic S-velocity, defined as $V_{S(iso)} = \sqrt{(2V_{SV}^2 + V_{SH}^2)/3}$ and the anisotropic parameter ξ, defined as $\xi = \frac{V_{SH}^2}{V_{SV}^2}$ (Panning and Romanowicz, 2006). Since the period range of the Love wave phase velocity data (see Fig 5.2.2) is limited, providing a sensitivity mainly above 200 km, we only show the upper 200 km of the model.

The isotropic S-velocity structure is similar to the shear-velocity structure inferred from Rayleigh waves for the extended area in chapter 4. The GofC is characterized by overall very low velocities. The relatively high velocity anomaly beneath the central part of the GofC at depths between 80 and 160 km in chapter 4 can be identified in this model as well. It is interpreted as a slab remnant beneath central Baja California (see chapter 4).

The new aspect of the current study is the determination of radial anisotropy from the combination of Love and Rayleigh wave phase velocity data. In general, we find that ξ is greater than one in the mantle. $\xi \geq 1$ means that $V_{SH} \geq V_{SV}$. The amplitude of the radial anisotropy becomes less in this model at a depth of more than 100 km. Since this could be due to the decrease in the data coverage of Love waves at long periods, we decided to interpret the radially anisotropic model only in the upper 100 km. When we interpret our model of radial anisotropy, we have to keep in mind that it is a very conservative model due to the strong damping applied to the anisotropic part. The pattern is therefore more meaningful than the absolute values.

There are two major tendencies in our model. Firstly, at mantle depths down to 100 km, ξ generally increases with depth. Secondly, the radially anisotropic structure varies in the upper 100 km of the mantle along the strike of the Gulf; ξ is higher in the central-southern Gulf region, right above the high velocity anomaly in the isotropic shear velocity model, whereas it is less in the slabless northern part of the Gulf and at the mouth of the Gulf.

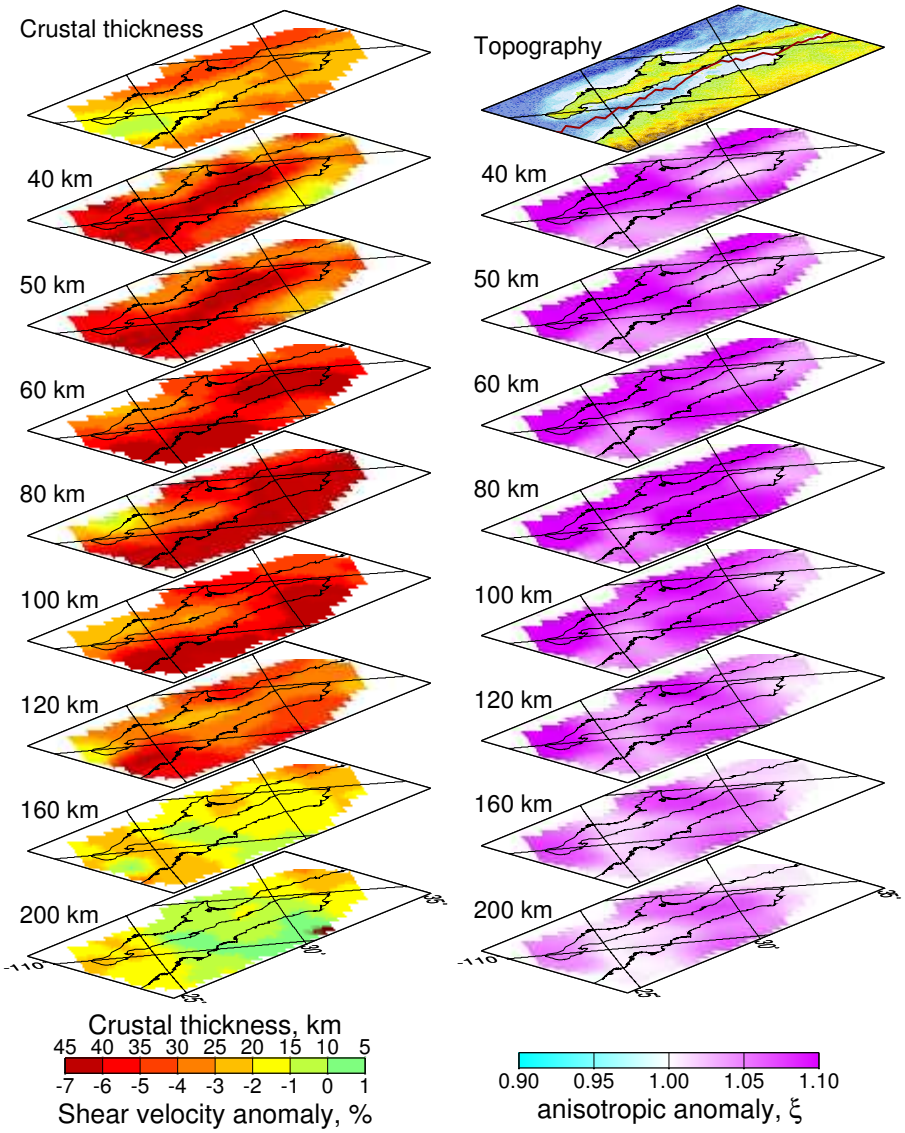

Figure 5.3.1: Anisotropic shear-velocity structure. The left panel shows maps of the crustal thickness (upper panel), and the isotropic shear-velocity anomalies relative to the global reference model AK135 (Kennett et al., 1995). The right panel shows the radially anisotropic structure ξ in the upper mantle and the topography of the region (upper panel)

5.4 Interpretation and discussion

Seismic anisotropy in the upper mantle is believed to be a reflection of the lattice-preferred orientation (LPO) of the mantle minerals (mainly olivine) (e.g., Estey and Douglas, 1986; Karato, 1998; Montagner, 1998). Therefore, it has often been used to infer the deformation geometry of the Earth's upper mantle (e.g., Montagner, 2002; Marone et al., 2007; Visser et al., 2008). Radial anisotropy with $\xi > 1$, i.e. $V_{SH} > V_{SV}$, is often interpreted as evidence of horizontal flow, whereas $\xi < 1$, i.e. $V_{SH} < V_{SV}$ is generally related to vertical flow. This is under the assumption that the fast axis of olivine aligns with the flow direction for A-type of olivine fabric (Nicolas and Christensen, 1987). However, recent studies on mineral physics and petrological observations have revealed that other types of olivine fabric can exist in the upper mantle. Therefore, the relationship between seismic anisotropy and LPO is more complex, as is shown in, e.g., Jung and Karato (2001) and Karato (2008). These studies show that the A-type fabric is only present in depleted water-poor regions like lithosphere, except in local high-stress regions where the D-type fabric will develop. In undepleted regions with a moderate to high water content, such as subduction zones, plumes or deep asthenosphere, other types of olivine fabrics (B-, C-, or E-type) can exist. With these, the relationship between anisotropy and the flow direction can be different from those of A-type. For an overview of the olivine fabrics and their relation to flow see Karato et al. (2008).

Our results indicate that the magnitude of $\xi > 1$, i.e. $V_{SH} > V_{SV}$, increases with depth in upper 100 km of the mantle. If only A-type LPO of olivine is present, this means that the horizontal alignment of the minerals would increase with depth. This could be explained by a gradual change in the flow direction with more horizontal flow at larger depth.

The magnitude of $\xi > 1$, i.e. $V_{SH} > V_{SV}$, also changes along the strike of the Gulf. ξ is higher in the central-southern Gulf region, right above the high velocity anomaly of the isotropic shear wave velocity model, whereas it is less in the slabless northern part and the mouth of the Gulf. The high velocity anomaly has been interpreted as a Farallon microplate slab remnant in chapter 4. If only A-type LPO of olivine is concerned, this could imply that there is stronger horizontal flow above the slab remnant than in the slabless area at same depth, or stated differently, that there is a larger component of vertical flow in the slabless mantle.

If other olivine fabrics exist in the upper mantle beneath the GofC, the interpretation could be different. However, B- or E-type fabrics would produce $\xi > 1$ for horizontal flow as well, with E-type giving a smaller amplitude. Therefore, the presence of B- and/or E-type fabrics would lead the same interpretation as above.

The C-type would lead a different interpretation. Nevertheless, the C-type fabric needs a high-water content and low-stress environment (Karato et al., 2008), which is not likely in the shallow upper mantle (Karato, 2008).

Additional information on the LPO can be obtained from azimuthal anisotropy. The Rayleigh wave phase velocity maps of chapter 4 (see Fig. 4.2.2) can be used for this purpose. In the Gulf region, at a period of 30 s, with a main sensitivity below the crust, the 2ψ Rayleigh wave azimuthal anisotropy is smaller than at periods of 50 and 80 s. This agrees with our interpretation of increasing horizontal flow at larger mantle depths.

SKS splitting studies of Obrebski et al. (2006) and van Benthem et al. (2008) show roughly E-W fast directions for the stations in the North and on the southern tip of the Baja California peninsula, whereas small delay times and null measurements are dominant in the central and southern part of the peninsula. The change in pattern seems related to the presence of the slab remnant and coincides with the change in the radially anisotropic structure revealed in our study. Indeed, van Benthem et al. (2008) suggested that their observations of low anisotropy may be caused by subducted microplate fragments. The splitting data, however, do not have much depth resolution (Sieminski et al., 2008). Using receiver functions, Obrebski and Castro (2008) interpreted a shallow mantle layer in their anisotropic model of the lithosphere beneath NE75 as either a subducted oceanic crust or a metamorphosed wedge. Our model would favour the interpretation of a metamorphosed wedge with mantle flow above the slab fragment which is found at larger depth.

5.5 Conclusion

Our model of radial anisotropy in the uppermost mantle (40-100 km) beneath the Gulf of California shows two tendencies: an average increase of ξ with increasing depth, and lateral variations of ξ. The former observation suggests that there is more vertical flow at shallow depths, pointing to an increase of ascending mantle material with decreasing depth beneath the rift zone. The second observation of lower ξ in the 40-100 km depth range beneath the northern Gulf points to stronger vertical flow beneath the northen part of the Gulf compared to the central-southern Gulf. This change in flow pattern can be associated to the presence of a slab window beneath the northern Gulf, and the presence of a slab remnant beneath the central-southern Gulf which acts as a barrier to the vertical ascent of mantle material.

Chapter 6

Synthesis and conclusions

In this final chapter, we first summarize our findings, and then propose a new tectonic scenario based on them. Lastly, we give suggestions for future work.

6.1 Summary

The NARS-Baja project is designed as a passive seismic experiment to explore the mantle beneath the Gulf of California region. This thesis presents the results on the upper mantle structure beneath the GofC from surface wave dispersion analysis. The study contains three aspects: the Rayleigh wave phase velocity structure with azimuthal anisotropy in the GofC region (chapter 3); the shear velocity model of GofC and its vicinity inferred from Rayleigh wave dispersion data (chapter 4); the radially anisotropic shear wave velocity model inferred from Love and Rayleigh wave dispersion (chapter 5).

The seismic models of the upper mantle beneath the GofC and surrounding regions show some interesting features. The average shear-velocity structure has a strong low-velocity zone ($3\% - 4\%$ lower than AK135) beneath a thin lid. The average phase velocity data are even suggestive of lower velocities than the global average down into the transition zone (chapter 3). The low velocities at asthenospheric depths are indicative of fluids and/or melt (Goes and van der Lee, 2002). There are several possible explanations for the presence of fluids or melts in the tectonically complex mantle of the Gulf of California as we will see. They can be caused by dehydration and/or partial melting of subducted lithosphere, by decompression melting in a region of an opening slab window, or just simply by partial melting due to high temperature.

An important feature of our seismic models is a relatively high shear-velocity

anomaly beneath the central-southern gulf extending from a depth of roughly 120 to 160 km (chapters 4 and 5). This anomaly is interpreted as a remnant of a subducted Farallon microplate fragment (see chapter 4). There is no evidence for such a slab remnant beneath the northern part of the gulf, in agreement with the tectonic interpretation of the region (REFERENCES). We therefore interprete this region as having a slab window, similar to the area at the mouth of the gulf.

Additional evidence on the upper mantle structure is obtained from anisotropy. An along-rift-axis variation is observed in the azimuthally anisotropic phase velocity maps of the fundamental mode Rayleigh waves of chapters 3 and 4, as well as in the radially anisotropic structure of chapter 5. In the upper 100 km of the mantle the parameter of radial anisotropy, $\xi = \frac{V_{SH}^2}{V_{SV}^2}$, is higher in the central-southern gulf region, compared the northern and southernmost region of the gulf. The region of higher ξ corresponds to the mantle above the slab remnant, whereas the regions of lower ξ correspond to the slabless areas at the same depth interval. The change in ξ can be related to a change in flow if we assume the lattice preferred orientation of olivine to be the dominant cause of the anisotropy. For the most likely types of olivine fabric at these conditions (A- and E-type) (Karato et al., 2008) it suggests that for the slabless areas there is less horizontal, or more vertical, flow compared to the mantle above the slab fragment. The Rayleigh wave phase velocity maps at 30 and 50 s, sensitive to a similar depth interval, substantiate the findings of radial anisotropy in the sense that larger values of 2ψ-(azimuthal) anisotropy are found for the region of the slab remnant.

6.2 Proposed scenario

The obtained upper mantle structure sheds light into the interior of this dynamic plate boundary developing area. The current stage of the mantle is a consequence of the local tectonic evolution. Combining the tectonic history of the region, including observations of a diversity in magmatism and variations in the style of rifting along the gulf, we propose a new tectonic interpretation of the region based on the mantle structure revealed in this study. It describes the tectonic evolution of the last 12 million years in the Gulf of California both spatially and temporally.

The formation of Gulf of California is associated with the rather abrupt cessation of subduction of Farallon microplates beneath Baja California at 12 Ma. Our seismic model suggests the presence of a slab fragment in the mantle. The presence of a slab beneath central Baja California was already proposed based on post-12 Ma volcanism with a slab signature (e.g Pallares et al., 2007; Conly et al., 2005). We attribute the relatively high shear-velocity anomaly beneath the central-

southern gulf to the Guadalupe microplate mainly because it subducted the oldest and coldest oceanic lithosphere. Furthermore, the North-South extend of the anomaly matches the North-South extend of the Guadalupe microplate of which the western, unsubducted part was identified from magnetic anomalies (SEE FIGURE 1.1.1). A third point strengthening our interpretation is that the location of the high velocity anomaly agrees with the location of the Guadalupe microplate relative to Baja California at 12 Ma from plate-tectonic reconstructions (Lonsdale, 1991; Stock and Lee, 1994). Our interpretation has important consequences as it implies that the Guadalupe slab remnant has not moved significantly relative to Baja California. Thus, our seismic model requires a tectonic reconstruction with a stalled Guadalupe slab remnant.

Our new tectonic interpretation of evolution the Gulf of California is based upon tectonic reconstructions, volcanic evidence, and our seismic interpretation of a stalled Guadalupe slab remnant. In our model, the development of the slab window beneath the North American lithosphere and pre-existing fracture zones in the subducting plate are essential in the tectonic evolution. We identify four subsequent stages that are illustrated in Fig. 6.2.1 and labeled I through IV in the following paragraphs.

I: Prior to 12.5 million years, eastward subduction of the Farallon plate fragments, associated with the Guadalupe and Magdalena microplates, was building a back-arc volcanic belt on Baja California. Meanwhile the Soledad Ridge had reached the trench; this means that, beneath the continent, the slab window was developing and approaching the Guadalupe Fracture Zone from the north.

At around 12.5 Ma, thermal erosion along the slab window reached the Guadalupe Fracture Zone from the north. Meanwhile, the northernmost segment of the Magdalena ridge encountered the trench as well. This led to a further opening of the asthenospheric window along the south boundary of the Guadalupe plate, the Shirley Fracture Zone. This caused the slab tearing. The Guadalupe slab became detached, from the main part of the subducted Farallon plate, along the two subducted fracture zones and broke off at depth. As a consequence of the slab pull removal, the Guadalupe ridge stopped spreading and the subduction of the Guadalupe microplate ceased. Since then, the Guadalupe microplate has been capture by the Pacific Plate.

From approximately 12 to 6 Ma: Thermal erosion progressed, at this stage, also along the near-coastal transform faults. Eventually, these faults must have cut through the subducting Guadalupe lithosphere, leaving the Guadalupe slab remnant beneath Baja California completely detached from its origin, the Farallon slab. The tearing continued near the transform faults, eventually setting the

Magdalena microplate free from the subducted parts. Since then it has been captured by the Pacific plate. The plate motion had been largely accommodated in the San Benito and Tosco-Abreojos transform faults, with an extensional component taken up in the back-arc region. The Guadalupe slab remnant became completely detached. The 'proto-gulf' was developing in the back-arc region.

Eventually, with the east pacific rise propagated into the proto-gulf at approximately 6 Ma, most of the Pacific-North America transform motion moved inland and accommodated itself in this proto-gulf area, along transform faults and pull-apart basins. Spreading started to develop in the modern Gulf of California. The gulf started to open, and the Baja peninsula started to move with the Pacific plate. At present, approximately 90% of the Pacific-North American plate motion (of 51 mm/yr) is taken up by the northwest extension in the gulf (Plattner et al., 2007).

Figure 6.2.1: Proposed scenario for the tectonic evolution of the Gulf of California. GM−Guadalupe Microplate; MM−Magdalena Microplate; GFZ−Guadalupe Fracture Zone; SFZ−Shirley Fracture Zone; MR−Soledad Ridge; MR−Magdalena Ridge. > 12.5 Ma: The Farallon slab associated with the Guadalupe and Magdalena microplates, indicated in red, was actively subducting beneath the North American continent. A slabless area, or slab window, started to develop in the north where Pacific-North American plate motion is taken up by transform faulting. The subducted Guadalupe and Shirley Fracture Zones are indicated by the grey dashed lines. Thermal erosion along the slab window weakened the northern part of the Guadalupe slab and initiated tearing. ~ 12.5 Ma: The Magdalena ridge encountered the trench. The Guadalupe slab became detached along the two subducted fracture zones and broke off at depth. The Guadalupe microplate stopped subducting and spreading ceased; it has been captured by the Pacific Plate since then, and its relative motion with the North American is accommodated by the San Benito and Tosco-Abreojos transform faults. Extension was taken up in the back-arc region. 12-6 Ma: Thermal erosion progressed, also along the near-coastal transform faults. The Guadalupe slab remnant became completely detached. The 'proto-gulf' started to develop in the back-arc region. The Pacific-North America transform motion moved into the Gulf at 6 Ma. The Gulf accommodated the new oblique northwest-southeast extension by wide transtensional rifts in most parts, but active spreading occurred in the Guaymas basin.

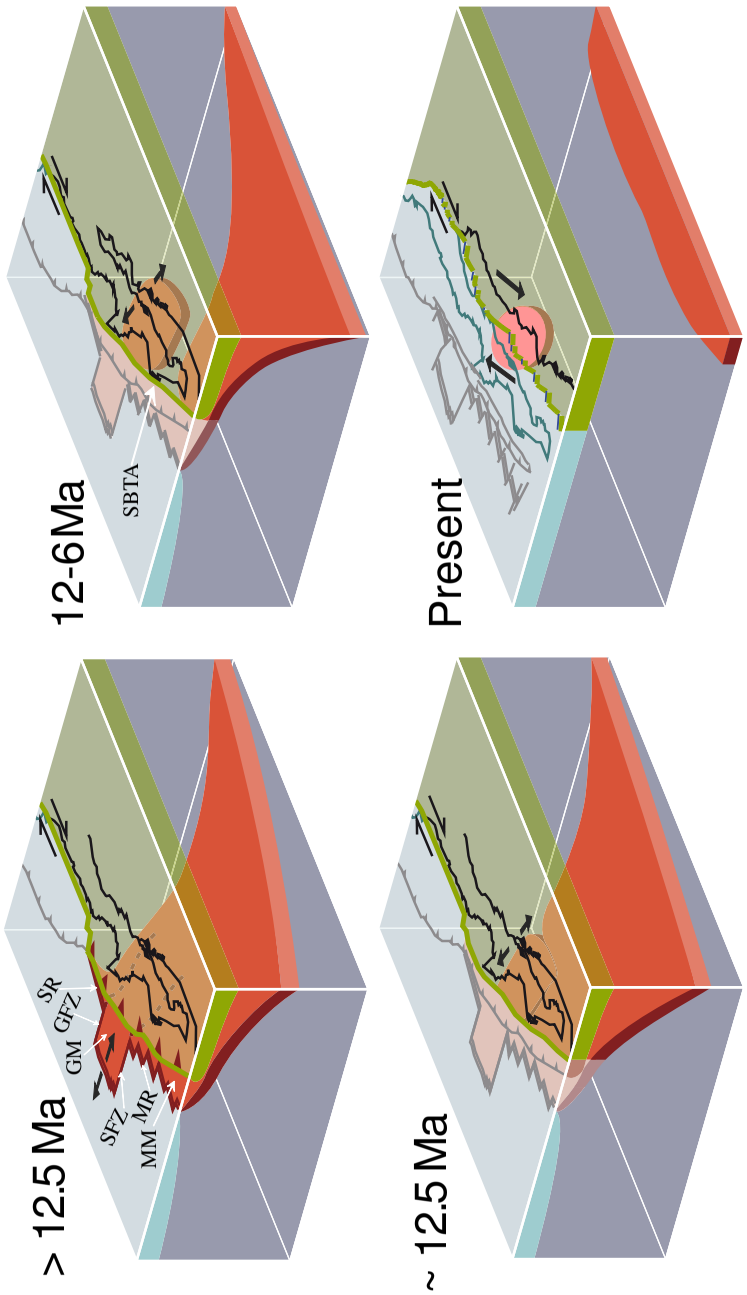
12-6Ma
SBTA
Present
> 12.5 Ma
SR
GFZ
GM
SFZ
MM
MR
~ 12.5 Ma

6.3 Concluding remarks and future work

Following the first ridge-trench collision, the Pacific-North America plate boundary has been localizing itself at the weakest point among the interacting plates. There were already weakened features in these plates, such as the pre-existing linear features in the slab (ridges, fracture zones), faults and extended back-arc basins in the overriding plate. The southward propagating slab window (induced by the first ridge-trench collision) has been continually meeting the fracture zones, together with some newly subducted ridges; the latter had produced secondary slab windows. One unexpected consequence of this, is the leaving behind of part of the Guadalupe slab and the opening up of the Gulf of California.

An intriguing question still left in this region is, whether there is a deep seated (>300 km) source of low-velocity mantle material that feeds the low-velocity features imaged in our phase velocity maps. The results of the model space search show considerable uncertainty in the transition zone, but the phase velocity measurements do favour a low-velocity or a thin transition zone. If confirmed by additional data, this could explain the overall low velocities of the region as well as the origin of the upwelling beneath the Gulf of California.

As we know, there are four Farallon fragments left in this region. In this work, we depict the possible fate of the Guadalupe and Magdalena microplates. But, what happened to the two northerly microplates in the mantle, the Arguello and the Monterey? Could pieces of slab remnants from them be left in the upper mantle as well?

In conclusion, the details of the subduction dynamics and the plate boundary relocation can be largely modulated by the already weakened features in the plates. The pre-existing linear features in the subducted plate, i.e. ridges and fracture zones, can determine the tearing and fracturing of the slab. Whereas, in the overriding plate, faults and extended back-arc basins can be essential to the plate motion relocation.

Samenvatting(Summary in Dutch)

De Golf van Californië, ookwel Zee van Cortés genoemd, is een zee van de Grote Oceaan die het schiereiland Baja-Californië van het Mexicaanse vasteland scheidt. Onder het water, op de zeebodem in het midden van de Golf, bevindt zich een actieve plaatgrens. Deze gaat in het noorden, in Californië, over in de plaatgrens van de San Andreas breuk waarlangs zijschuiving plaatvindt, en in het zuiden in de plaatgrens van de Oost-Pacifische Rug waarlangs spreiding plaatsvindt. De plaatgrens in de Golf van Californië verandert daarmee van karakter van enerzijds oceanische spreidingscentra en transformbreuken in het zuiden tot anderzijds een gebied van extensie in het noorden (Nagy and Stock, 2000; González-Fernández et al., 2005; Lizarralde et al., 2007). Het is nog onduidelijk wat de oorzaken zijn van de verschillen in rifting tussen het zuidelijk deel en het noordelijke deel.

Kennis van de bovenmantelstructuur is van belang voor een beter begrip van de tektonische evolutie van deze regio. Eerdere tomografische studies toonden lage S-snelheden aan in de bovenste 250 km van de mantel (e.g., Lebedev and van der Hilst, 2008; van der Lee and Frederiksen, 2005; Godey et al., 2003), maar de resolutie van deze tomografische resultaten is onvoldoende voor een gedetailleerd beeld van de bovenmantelstructuur. Dit komt omdat er geen seismologische registraties uit het gebied beschikbaar waren.

De 14 stations van het Netwerk van Autonoom Registrerende Seismografen, ookwel NARS genoemd, zijn van 2002 tot 2008 rondom de Golf van Californië geplaatst. Samen met 5 stations van het zg. RESBAN netwerk van het Centro de Investigación Científica y de Educación Superior de Ensenada vormden ze het NARS-Baja project. Met behulp van de gegevens van dit project is het voor het eerst de mogelijk om de bovenmantelstructuur onder deze regio in kaart te brengen.

Het doel van het onderzoek beschreven in dit proefschrift is het verkrijgen van een S-snelheidsmodel van de bovenste 300 km van de mantel. Het principe van de methode kan als volgt verklaard worden. Golven die na een aardbeving door de aarde reizen, geven informatie over het gesteente waar ze doorheen hebben gereisd. De oppervlaktegolven reizen langs het aardoppervlak en hebben de grootste amplitude op het seismogram, waarbij de laagfrequente oppervlaktegolven de diepe structuur bemonsteren en de hoogfrequente oppervlaktegolven gevoeliger zijn voor de ondiepe structuur. De frequentie-afhankelijke fasesnel-

heid, de snelheid waarmee de golven langs aardoppervlak reizen, geeft daarmee informatie over de structuur van de ondergrond. In dit proefschrift zijn frequentie-afhankelijke fasesnelheden gemeten tussen stations van het NARS-Baja project en andere seismologische netwerken in de regio. Deze metingen zijn gebruikt om fasesnelheidsstructuur te maken die vervolgens geïnverteerd zijn de S snelheidsmodel met de diepte. Zo zijn 3-dimensionale S-snelheidsmodellen van de bovenmantel verkregen.

De studie bestaat uit drie delen: de fasesnelheidsstructuur van Rayleigh oppervlaktegolven met azimuthale anisotropie in de Golf van Californië (hoofdstuk 3); een S-snelheidsmodel van de Golf van Californië en zijn omgeving (hoofdstuk 4); een radieel anisotroop S-snelheidsmodel afgeleid uit Love and Rayleigh oppervlaktegolfmetingen (hoofdstuk 5). Tenslotte wordt een synthese van de resultaten gegeven samen met een interpretatie van de tektonische evolutie van het gebied (hoofdstuk 6).

De seismische bovenmantelstructuur onder de Golf van Californië en omliggende regio's toont een aantal interessante aspecten. De gemiddelde S snelheidsstructuur heeft een sterke lage snelheidslaag ($3\% - 4\%$ lager dan referentiemodel AK135) onder een relatief dunne lithosfeer (hoofdstuk 3). De lage snelheden op asthenosferische diepten zijn indicatief voor vloeistoffen en / of smelten (Goes and van der Lee, 2002). De gemiddelde fasesnelheidscurve van het gebied wijst verder op lager dan mondiaal gemiddelde snelheden in de transitiezone (hoofdstuk 3). Een opvallend kenmerk van de 3-D seismische modellen is een relatief hoge S snelheidsanomalie onder de centraal-zuidelijke golf op een diepte van ongeveer 120 tot 160 km (hoofdstukken 4 en 5). Deze anomalie wordt geïnterpreteerd als een overblijfsel van een fragment van een ondergeschoven Farallon microplaat (zie hoofdstuk 4). De seismische modellen geven geen aanwijzing voor een dergelijk slab-overblijfsel onder het noordelijk deel van de golf, in overeenstemming met eerdere tektonische interpretaties van de regio. We interpreteren deze regio dan ook als een met een "slab-venster", net als het gebied aan de monding van de golf. Aanvullend bewijs voor de bovenmantelstructuur wordt verkregen uit anisotropie. De fasesnelheidskaarten van de Rayleigh-golven tonen een verandering van de richting van azimuthale anisotropie over de lengte-as van de golf (hoofdstukken 3 en 4) evenals een verandering van de radiële anisotropie (hoofdstuk 5).

De verkregen bovenmantelstructuur werpt licht op de evolutie van deze dynamische plaatgrens. We presenterem een nieuwe tektonische interpretatie van de evolutie van de Golf van Californië op basis van tektonische reconstructies, vulkanisme, en onze seismische interpretatie van een gestagneerd slabfragment. In ons

model zijn de ontwikkeling van het slab-venster onder in de noordelijke regio en bestaande breukzones in de onderschuivende plaat van essentieel belang geweest voor de tektonische evolutie.

Dankwoord (Acknowledgments)

The seismology group in Utrecht is very friendly and sociable, and I am very glad to have been part of it.

I am very grateful indeed to my supervisor Hanneke Paulssen; without your guidance and support, this thesis would not have been possible. I enjoyed all the scientific and social talks we shared, and it is my great luck to have had you as my supervisor. You have given me a great deal of support, joy and encouragement. It has been a real pleasure to work with you for 4 years. I thank my promoter Jeannot Trampert for all the support and guidance, especially for your comments and suggestions on my thesis. It has been fun to see your thoughts sparkle.

I would also like to thank Sergei Lebedev for all his support, although there were many depressing occasions when you told me that I had just rewritten part of your codes after a week of hard work. But without using your codes (or rewriting them clumsily), I would not have reached the end. Thank you also for the Perugia trip; I suspect that you have put me under your care in those days. Thanks also to Thomas Meier and Frederic Deschamps for providing some codes and for their attention to my work; also to Rinus Wortel and Rob Govers for their interest.

I am grateful for Arie van Wettum's excellent job on the NARs stations, to Jacqueline Landsheer for help on all the management issues, to Joop Hoofd and Theo van Zessen for help on computer questions. Without you all, I could not have finished this PhD project. I thank Henk van der Meer for coffee and cookies and for tolerating my irregular visits. *Het is altijd gezellig op de koffiepauze*. My thanks go to my office mate Ebru Dozdag, for all the food we shared and for taking me home when there was no train to Nijmegen; to Ilaria Mosca for the coffee, tea and the introduction to good Italian food; to Zhihong and Yanchun for all your support and friendship; to Anne Sieminski especially for the lunch time jogging; to Karin Visser for your help, especially for the information on the TNO job–your enthusiasm for the TNO definitely warmed me up to the idea. Thanks are due to all the people I have worked with in the last 4 years, Wouter Kimmen, Ueli Meier, Celine Tirel, Stefan Carpentier, Tim van Zon, Maisha Amaru, Thomas Geenen, Joost van Summeren , Roberta de Franco, Bahjat Alhammoud, Pasha Karami Arokhloo, Marzieh Baes, Gabriela Tanasescu, Steven van Benthem, Kabir Roy-Chowdhury, Wim Spakman and Paul Meijer.

And finally, my thanks go to all my in-laws in the de Jong family (though the word *in-law* is almost insulting in this case). All the help and friendship I have gotten from you has gone far beyond the word *in-law*. So thank you Gwyn, Sarah,

Rachel and Catharine; you have been always there when I needed help. I thank Peter for all his support and especially to my dear daughter Mary; without you both I would not have had the strength to pull through. Last words have to go to my parents and friends in China. *Xie xie da jia*.

Bibliography

Aguillón-Robles, A., Calmus, T., Benoit, M., Bellon, H., Maury, R., Cotten, J., Bourgois, J., and Michaud, F. (2001). Late Miocene adakites and Nb-enriched basalts from Vizcaino Peninsula, Mexico: indicators of East Pacific Rise subduction below southern Baja California? *Geology*, 29:531–534.

Anderson, D. (1961). Elastic wave propagation in layered anisotropic media. *J. Geophys. Res.*, 66:2953–2963.

Atwater, T. (1970). Implications of plate tectonics for the Cenozoic tectonic evolution of western North America. *GSA Bulletin*, 81:3513–3535.

Atwater, T. and Stock, J. M. (1998). Pacific-North America plate tectonics of the Neogene Southwestern United States: An Update. *Int. Geol. Rev.*, 40:375–402.

Barmin, M., Ritzwoller, M., and Levshin, A. (2001). A fast and reliable method for surface wave tomography. *Pure Appl. Geophys.*, 158(8):1351–1375.

Bassin, C., Laske, G., and Masters, G. (2000). The current limits of resolution for surface wave tomography in North America. *EOS Trans. AGU*, 81:F897.

Batiza, R. (1978). Geology, petrology, and geochemistry of Isla Tortuga, a recently formed tholeiitic island in the Gulf of California. *Geol. Soc. Am. Bull.*, 89:1309–1324.

Beghein, C., Trampert, J., and van Heijst, H. J. (2006). Radial anisotropy in seismic reference model of the mantle. *J. Geophys. Res.*, 111:B02303 doi:10.1029/2005JB003728.

Bellon, H., Aguillón-Robles, A., Calmus, T., Maury, R., Bourgois, J., and Cotten, J. (2006). La Purisima Volcanic Field, Baja California Sur, Mexico: Mid-Miocene to Recent volcanism in relation with subduction and asthenospheric window opening. *J. Volcanol. Geotherm. Res.*, 152:253–272.

Benoit, M., Aguillón-Robles, A., Calmus, T., Maury, R., Bellon, H., Cotten, J., Bourgois, J., and Michaud, F. (2002). Geochemical diversity of Late Miocene volcanism in southern Baja California, Mexico: implication of mantle and crustal sources during the opening of an asthenospheric window. *J. Geol.*, 110:627–648.

Bohannon, R. G. and Parsons, T. (1995). Tectonic implications of post-30 Ma Pacific and North American relative plate motions. *Geol. Soc. Am. Bull.*, 107:937–959.

Calmus, T., Aguilln-Robles, A., Maury, R., Bellon, H., Benoit, M., Cotten, J., Bourgois, J., and Michaud, F. (2003). Spatial and temporal evolution of basalts and magnesian andesites (bajaites) from Baja California, Mex́ico: the role of slab melts. *Lithos.*, 66:77–105.

Conly, A., Brenan, J., Bellon, H., and Scott, S. (2005). Arc to rift transitional volcanism in the Santa Rosala Region, Baja California Sur, Mexico. *J. Volcanol. Geotherm. Res.*, 142:303–341.

Crampin, S. and Lovell, J. H. (1991). A decade of shear-wave splitting in the Earth's crust: what does it mean? what

use can we make of it? and what should we do next? *Geophys. J. Int.*, 107:87–407.

Dahlen, F. A. and Tromp, J. (1998). *Theoretical global seismology*. Princeton University Press, Princeton, USA.

Deschamps, F., Lebedev, S., Meier, T., and Trampert, J. (2008). Azimuthal anisotropy of Rayleigh-wave phase velocities in the east-central United States. *Geophys. J. Int.*, 173:827–843 doi:10.1111/j.1365–246X.2008.03751.x.

Dickinson, W. and Snyder, W. (1979a). Geometry of subducted slabs related to San Andreas transform. *J. Geol.*, 87:609–627.

Dickinson, W. and Snyder, W. (1979b). Geometry of triple junctions related to San Andreas transform. *JGR*, 84:561–572.

Dziewonski, A. and Anderson, D. L. (1981). Preliminary Reference Earth model. *Phys. Earth Planet. Inter.*, 25:297–356.

Estey, L. H. and Douglas, B. J. (1986). Upper mantle anisotropy: A preliminary model. *JGR*, 91:11393–11406.

Ferrari, L. (2004). Slab detachment control on mafic volcanic pulses and mantle heterogeneity in central Mexico. *Geology*, 32:77–80.

Fletcher, J. M., Grove, M., Kimbrough, D., Lovera, O., and Gehrels, G. E. (2007). Ridge-trench interactions and the Neogene tectonic evolution of the Magdalena shelf and southern Gulf of California: Insights from detrital zircon U-Pb ages from the Magdalena fan and adjacent areas. *GSA Bulletin*, 119:1313–1336, doi 10.1130/B26067.1.

Furlong, K. P. (1993). Thermal-rheological evolution of the upper mantle and the development of the San Andreas Fault system. *Tectonophysics*, 223:149–164.

Gastil, G., Krummenacher, D., and Minch, J. (1979). The record of Cenozoic volcanism around the Gulf of California. *GSA Bulletin*, 90:839–857.

Godey, S., Snieder, R. K., Villaseñor, A., and Benz, H. M. (2003). Surface wave tomography of North America and the Caribbean using global and regional broad-band networks: phase velocity maps and limitations of ray theory. *Geophys. J. Int.*, 152:620–632.

Goes, S. and van der Lee, S. (2002). Thermal structure of the North American uppermost mantle inferred from seismic tomography. *J. Geophys. Res.*, 107:B32050, doi:10:1029/2000JB000049.

González-Fernández, A., Dañobeitia, J. J., Delgado-Argote, L. A., Michaud, F., Córdoba, D., and Bartolomé, R. (2005). Mode of extension and rifting history of upper Tiburón and upper Delfín basins, northern Gulf of California. *J. Geophys. Res.*, 110:B01313, doi:10.1029/2003JB002941.

Grand, S. P. (1994). Mantle shear structure beneath the americas and surrounding oceans. *J. Geophys. Res.*, 99(B6):11591–11621.

Gripp, A. E. and Gordon, R. G. (2002). Young tracks of hotspots and current plate velocities. *Geophys. J. Int.*, 150:321–361.

Gubbins, D. (2004). *Time Series Analysis and Inverse Theory for Geophysicists*. Cambridge Univ. Press, Cambride, UK.

Gung, Y., Panning, M., and Romanowicz, B. (2003). Global anisotropy and the thickness of continents. *Nature*, 422:707–711.

Hausback, B. P. (1984). Cenozoic volcanism and tectonic evolution of Baja Cali-

fornia Sur, Mexico. In Frizell, V. A., editor, *Geology of the Baja California Peninsula: Pacific section*, volume 39, pages 219–236. Soc. Eco. Pal. and Min., Los Angeles, California.

Henry, C. D. and Aranda-Gomez, J. J. (2000). Plate interactions control middlelate Miocene proto-Gulf and basin and range extension in the southern basin and range. *Tectonophysics*, 318:1–26.

Ji, C., Tsuboi, S., Komatitsch, D., and Tromp, J. (2005). Rayleigh Wave Multipathing along the West Coast of North America. *BSSA*, 95:2115–2124, doi: 10.1785/0120040180.

Jung, H. and Karato, S.-i. (2001). Water-induced fabric transitions in olivine. *Science*, 293:1460–1463.

Kaminski, E. and Ribe, N. M. (2002). Timescales for the evolution of seismic anisotropy in mantle flow. *Geochem. Geophys. Geosyst.*, 3(8):1051, doi:10.1029/2001GC000222.

Karato, S.-i. (1998). Some remarks on the origin of seismic anisotropy in the D" layer. *Earth Planets Space*, 50:1019–1028.

Karato, S.-i. (2008). Insights into the nature of plumeasthenosphere interaction from central Pacific geophysical anomalies. *Earth planet. Sci. Lett.*, 274:234–240.

Karato, S.-i., Jung, H., Katayama, I., and Skemer, P. (2008). Geodynamic Significance of Seismic Anisotropy of the Upper Mantle: New Insights from Laboratory Studies. *Annu. Rev. Earth Planet. Sci.*, 36:59–95.

Karig, D. E. and Jensky, W. (1972). The proto-Gulf of California. *Earth planet. Sci. Lett.*, 17:169–174.

Kennett, B. L. N., Engdahl, E. R., and Buland, R. (1995). Constraints on seismic velocities in the earth from travel times. *Geophys. J. Int.*, 122:108–124.

Knopoff, L. (1972). Observation and inversion of surface-wave dispersion. *Tectonophysics*, 13:497–519.

Lebedev, S., Nolet, G., Meier, T., and van der Hilst, R. D. (2005). Automated multimode inversion of surface and S waveforms. *Geophys. J. Int.*, 162:951–964, doi: 10.1111/j.1365–246X.2005.02708.x.

Lebedev, S. and van der Hilst, R. D. (2008). Global upper-mantle tomography with the automated multimode inversion of surface and S-wave forms. *Geophys. J. Int.*, 173:505–518, doi: 10.1111/j.1365–246X.2008.03721.x.

Levshin, A. and Ratnikova, L. (1984). Apparent anisotropy in inhomogeneous media. *Geophys. J. R. Astron. Soc.*, 76:65–69.

Lewis, J. L., Day, S. M., Magistrale, H., Castro, R. R., Astiz, L., Rebollar, C., Eakins, J., Vernon, F. L., and Brune, J. N. (2001). Crustal thickness of the Peninsular Ranges and Gulf Extensional Province in the Californias. *J. Geophys. Res.*, 106(B7):13599–13611.

Lizarralde, D., Axen, G. J., Brown, H. E., Fletcher, J. M., González-Fernández, A., Harding, A. J., Holbrook, W. S., Kent, G. M., Paramo, P., Suther, F., and Umhoefer, P. J. (2007). Variation in styles of rifting in the Gulf of California. *Nature*, 448:466–469, doi:10.1038/nature06035.

Lonsdale, P. (1989). Geology and tectonic history of the Gulf of California. In Hussong, D., Winterer, E. L., and Decker, R. W., editors, *The Eastern Pacific Ocean and Hawaii*, volume N of *The Geology of North America*, pages 499–521. Geological Society of Ame-

rica, Boulder, Colorado.

Lonsdale, P. (1991). Structural patterns of the Pacific floor offshore of peninsular California. In Dauphin, J. P. and Simoneit, B. R. T., editors, *The gulf and peninsular province of the California*, volume 47 of *AAPG Memoir*, pages 87–125.

López-Pineda, L., Rebollar, C. J., and Quintanar, L. (2007). Crustal thickness estimates for Baja California, Sonora and Sinaloa, Mexico, using disperse surface waves. *J. Geophys. Res.*, 112:B04308, doi:10.1029/2005JB003899.

Love, A. E. H. (1927). *A Treatise on the Theory of Elasticity*. Cambridge University Press, Cambridge, UK.

Maggi, A., Debayle, E., Priestley, K., and Barruol, G. (2006). tomography of the Pacific Ocean: a closer look at the lithospheric cooling signature. *Geophys. J. Int.*, 166:1384–1397.

Mammerickx, J. and Klitgord, K. D. (1982). Northern East Pacific rise: evolution from 25 ma B.P to the present. *J. Geophys. Res.*, 87:6751–6759.

Marone, F., Gung, Y., and Romanowicz, B. (2007). Three-dimensional radial anisotropic structure of the North American upper mantle from inversion of surface waveform data. *Geophys. J. Int.*, 171:206–222 doi: 10.1111/j.1365–246X.2007.03465.x.

McEvilly, T. (1964). Central US crust-upper mantle structure from Love and Rayleigh wave phase velocity inversion. *Bull. Seismol. Soc. Am.*, 54:1997–2015.

Meier, T., Dietrich, K., Stockhert, B., and Harjes, H. P. (2004). One–dimensional models of shear wave velocity for the eastern Mediterranean obtained from the inversion of Rayleigh wave phase velocities and tectonic implications. *Geophys. J. Int.*, 156:45–58.

Meissner, R., Rabbel, W., and Kern, H. (2006). Seismic lamination and anisotropy of the lower continental crust. *Tectonophysics*, 416:81–99.

Merrer, S., Cara, M., Rivera, L., and Ritsema, J. (2007). Upper mantle structure beneath continents: New constraints from multi-mode Rayleigh wave data in western North America and southern Africa. *Geophys. Res. Lett.*, 34:L06309, doi:10.1029/2006GL028939.

Michaud, F., Royer, J.-Y., Bourgois, J., Dyment, J., Calmus, T., Bandy, W., Sosson, M., Mortera-Gutirrez, C., Sichler, B., Rebolledo-Viera, M., and Pontoise, B. (2006). Oceanic–ridge subduction vs. slab break–off: plate tectonic evolution along the Baja California Sur continental margin since 15 Ma. *Geology*, 34:13–16.

Montagner, J.-P. (1998). Where can seismic anisotropy be detected in the Earth's mantle? *Pure Appl. Geophys.*, 151:223–256.

Montagner, J.-P. (2002). Upper mantle low anisotropy channels below the Pacific Plate. *Earth planet. Sci. Lett.*, 202:263–274.

Montagner, J.-P. and Nataf, H.-C. (1986). A simple method for inverting the azimuthal anisotropy of surface waves. *J. Geophys. Res.*, 91:511–520.

Nagy, E. A. and Stock, J. M. (2000). Structural controls on the Continent–Ocean Transition in the Northern Gulf of California. *J. Geophys. Res.*, 105:B7, 16,251–16,269.

Nettles, M. and Dziewonski, A. M. (2008). Radially anisotropic shear velocity structure of the upper mantle globally and beneath North America. *J. Geophys. Res.*, 113:B02303,

doi:10.1029/2006JB004819.

Nicholson, C., Sorlien, C. C., Atwater, T., Crowell, J. C., and Luyendyk, B. P. (1994). Microplate capture, rotation of the western Transverse Ranges, and initiation of the San Andreas transform as a low angle fault system. *Geology*, 22:491–495.

Nicolas, A. and Christensen, N. L. (1987). Formation of anistropy in upper mantle peridotite. In Fuchs, K. and Froidevaux, C., editors, *Composition, Structure and Dynamics of the Lithosphere-Asthenosphere System*, pages 111–123. Am. Geophys. Union, Washington, DC.

Nolet, G. (1990). Partitioned waveform inversion and two-dimensional structure under the Network of Autonomously Recording Seismographs. *J. Geophys. Res.*, 95:8499–8512.

Obrebski, M. and Castro, R. R. (2008). Seismic anisotropy in northern and central Gulf of California region, Mexico, from teleseismic receiver functions and new evidence of possible plate capture. *J. Geophys. Res.*, 113:B03301, doi:10.1029/2007JB005156.

Obrebski, M., Castro, R. R., Valenzuela, R. W., van Benthem, S., and Rebollar, C. J. (2006). Shear–wave splitting observations at the regions of northern Baja California and southern Basin and Range in Mexico. *Geophys. Res. Lett.*, 33:L05302, doi:10.1029/2005GL024720.

Oskin, M. and Stock, J. (2003). Miocene to Recent Pacific–North America plate motion and opening of the Upper Delfín Basin, northern Gulf of California, Mexico. *Geol. Soc. Amer. Bull.*, 115:1173–1190.

Paige, C. and Saunders, M. (1982). LSQR: An algorithm for sparse linear equations and sparse least squares. *ACM Trans Math Softw*, 8:43–71.

Pallares, C., Maury, R. C., Bellon, H., Royer, J.-Y., Calmus, T., Aguillón-Robles, A., Cotten, J., Benoit, M., Michaud, F., and Bourgois, J. (2007). Slab–tearing following ridge–trench collision: Evidence from Miocene volcanism in Baja California, Mxico. *J. Volcanol. Geotherm. Res.*, 161:95–117, doi:10.1016/j.jvolgeores.2006.11.002.

Panning, M. P. and Romanowicz, B. A. (2006). A three-dimensional radially anisotropic model of shear velocity in the whole mantle. *Geophys. J. Int.*, 167:361–379.

Pedersen, H. A. (2006). Impacts of non-plane waves on two-station measurements of phase velocities. *Geophys. J. Int.*, 165:279–287, doi:10.1111/j.1365–246X.2006.02893.x.

Persaud, P., Pérez-Campos, X., and Clayton, R. W. (2007). Crustal thickness variations in the margins of the Gulf of California from receiver functions. *Geophys. J. Int.*, 170:687–669, doi:10.1111/j.1365–246X.2007.03412.x.

Persaud, P., Stock, J. M., Steckler, M. S., Martin-Barajas, A., Diebold, J. B., González-Fernández, A., and Mountain, G. S. (2003). Active deformation and shallow structure of the Wagner, Consag, and Delfín Basins, northern Gulf of California, Mexico. *J. Geophys. Res.*, 108:B7, 2355, doi:10.1029/2002JB001937.

Plattner, C., Malservisi, R., Dixon, T., Sella, G., Lafemina, P., Fletcher, J., and Suarez-Vidal, F. (2007). New constraints on relative motion between the Pacific plate and Baja California microplate (Mexico) from GPS

measurements. *Geophys. J. Int.*, pages 1373–1380, doi:10.1111/j.1365–246X.2007.03494.x.

Polet, J. and Kanamori, H. (2002). Anisotropy beneath California: SKS splitting measurements using a dense, broadband array. *Geophys. J. Int.*, 149:13–327.

Prindle, K. and Tanimoto, T. (2006). Teleseismic surface wave study for S–wave velocity structure under an array: Southern California. *Geophys. J. Int.*, 166:601–621, doi: 10.1111/j.1365–246X.2006.02947.x.

Sato, Y. (1955). Analysis of dispersed surface wave by means of Fourier Transform: Part 1. *Bull. Earthquake Res. Tokyo Univ.*, 33:33–47.

Sawlan, M. G. (1991). Magmatic evolution of the Gulf of California rift. In Dauphin, J. P. and Simoneit, B. R. T., editors, *The Gulf and Peninsular Province of the Californias*, volume Memoir 47, pages 301–370. The American Association of Petroleum Geologists, Tulsa, OK.

Sawlan, M. G. and Smith, J. G. (1984). Petrologic characteristics, age and tectonic setting of Neogene volcanic rocks in northern Baja California Sur, Mexico. In Frizell, V. A., editor, *Geology of the Baja California Peninsula: Pacific section*, volume 39, pages 237–251. Soc. Eco. Pal. and Min., Los Angeles, California.

Schlue, J. W. and Knopoff, L. (1978). Inversion of surface-wave phase velocities for an anisotropic structure. *Geophys. J. Int.*, 54:697–702.

Sebai, A., Stutzmann, E., Montagner, J.-P., Sicilia, D., and Beucler, E. (2002). Structure of the African upper mantle from Rayleigh and Love wave tomography. *Phys. Earth Planet.*, 155:48–62.

Severinghaus, J. and Atwater, T. M. (1990). Cenozoic geometry and thermal state of the subducting slabs beneath North America. In Wernicke, B. P., editor, *Basin and Range extensional tectonics near the latitude of Las Vegas, Nevada*, volume 176 of *Geol. Soc. Amer. Memoir*, pages 1–22. AGU.

Sieminski, A., Paulssen, H., Trampert, J., and Tromp, J. (2008). Finite-frequency SKS splitting: Measurement and sensitivity kernels. *Bull. Seis. Soc. Am.*, 98:1797–1810.

Smith, M. L. and Dahlen, F. A. (1973). The azimuthal dependence of Love and Rayleigh wave propagation in a slightly anisotropic medium. *J. Geophys. Res.*, 78:3321–3333.

Snieder, R. and Trampert, J. (1999). Inverse problems in geophysics. In Wirgin, A., editor, *Wavefield inversion*, pages 119–190. Springer Verlag, New York.

Spencer, J. and Normark, W. (1989). Neogene plate–tectonic evolution of the Baja California Sur continental margin and the southern Gulf of California, Mexico. In Winterer, E., Hussong, D., and Decker, R., editors, *The Geology of North America*, volume N of *The Eastern Pacific Ocean and Hawaii*, pages 489–497. Geological Society of America, Boulder, Colorado.

Stock, J. M. and Hodges, K. V. (1989). Pre–Pliocene extension around the Gulf of California and the transfer of Baja California to the Pacific Plate. *Tectonics*, 8(1):99–115.

Stock, J. M. and Lee, J. (1994). Do microplates in subduction zones leave a geological record? *Tectonics*, 13(6):1472–1487.

Süss, M. Peter and Shaw, John H. (2003). P wave seismic velocity structure derived from sonic logs and industry reflec-

tion data in the Los Angeles basin, California. *J. Geophys. Res.*, 108:B32170, doi:10.1029/2001JB001628.

Tarantola, A. (1987). *Inverse Problem Theory: Methods for Data Fitting and Model Parameter Estimation*. Elsevier, Amsterdam.

Trampert, J., A. van Wettum, J. R., Clayton, R., Castro, R., Rebollar, C., and Perez-Vertti, A. (2003). New Array Monitors Seismic Activity near the Gulf of California in Mexico. *Eos Trans. AGU*, 84(4):29–32.

Trampert, J. and Lévêque, J.-J. (1990). Simultaneous iterative reconstruction technique: physical interpretation based on the generalized least square solution. *J. geophys. Res.*, 95:12553–12559.

van Benthem, S. A. C., Valenzuela, R. W., Obrebski, M., and Castro, R. R. (2008). Measurements of upper mantle shear wave anisotropy from stations around the southern Gulf of California. *Geofísica Internacional*, 47:127–144.

van der Lee, S. and Frederiksen, A. (2005). Surface Wave Tomography applied to the North American upper mantle. In Nolet, G. and Levander, A., editors, *Seismic Data Analysis and Imaging With Global and Local Arrays*, volume 157 of *Geophys. Monogr. Ser.*, pages 67–80. AGU, Washington, D.C.

Visser, K., Lebedeva, S., Trampert, J., and Kennett, B. L. N. (2008). Probability of radial anisotropy in the deep mantle. *Earth planet. Sci. Lett.*, 270:241–250, doi:10.1016/j.epsl.2008.03.041.

Walck, M. C. (1984). The P-wave upper mantle structure beneath an active spreading centre: The Gulf of California. *Geophys. J. R. Astr. Soc.*, 76:697–723.

Webb, S. C. and Forsyth, D. W. (1998). Structure of the upper mantle under the EPR from waveform inversion of regional events. *Science*, 280:1227–1229, doi:10.1126/science.280.5367.1227.

Yang, Y. and Forsyth, D. W. (2006). Rayleigh wave phase velocities, small-scale convection, and azimuthal anisotropy beneath southern California. *J. Geophys. Res.*, 111:B07306, doi:10.1029/2005JB004180.

Zhang, J. J., Walter, W. R., Lay, T., and Wu, R. S. (2003). Time–domain pure–state polarization analysis of surface waves traversing California. *Pure Appl. Geophys.*, 160:1447–1478.

Zhang, X., Paulssen, H., Lebedev, S., and Meier, T. (2007). Surface wave tomography of the Gulf of California. *Geophys. Res. Lett.*, 34:L15305, doi:10.1029/2007GL030631.

Zhu, L. and Kanamori, H. (2000). Moho depth variation in southern California from teleseismic receiver functions. *J. Geophys. Res.*, 105:2969–2980.

Appendix A

Station list

Network	Station	Longitude(°N)	Latitude(°W)	Elevation(m)
NR	NE70	32.4210	115.2608	23
NR	NE71	31.6897	115.9053	1155
NR	NE72	30.8484	116.0586	17
NR	NE73	30.0651	115.3485	489
NR	NE74	28.0075	114.0138	21
NR	NE75	27.2933	112.8565	137
NR	NE76	26.8890	111.9991	35
NR	NE77	26.0158	111.3613	40
NR	NE78	24.3982	111.1064	82
NR	NE79	23.1194	109.7561	225
NR	NE80	30.5000	112.3199	225
NR	NE81	28.9183	109.6363	295
NR	NE82	26.9157	109.2308	183
NR	NE83	24.7309	107.7393	28
RB	BAHB	28.9440	113.5620	40
RB	CHXB	31.4720	115.0512	20
RB	GUYB	27.8987	110.8727	30
RB	PPXB	31.3350	113.6320	5
RB	TOPB	25.6100	109.0509	35
CI	ADO	34.5505	117.4339	908
CI	BAK	35.3444	119.1045	116
CI	BAR	32.6801	116.6722	529
CI	BC3	33.6552	115.4532	1137

CI	BCC	33.5751	117.2612	391
CI	BEL	34.0006	115.9982	1388
CI	CWC	36.4399	118.0802	1595
CI	DAN	34.6375	115.3812	428
CI	DVT	32.6592	116.1006	881
CI	FMP	33.7126	118.2938	89
CI	FUR	36.4670	116.8632	-37
CI	GRA	36.9961	117.3662	689
CI	GSC	35.3018	116.8057	1000
CI	IRM	34.1574	115.1451	567
CI	LGU	34.1082	119.0659	416
CI	LRL	35.4795	117.6821	1340
CI	MLAC	37.6302	118.8361	2162
CI	MPM	36.0580	117.4890	1839
CI	NEE	34.8249	114.5994	170
CI	OSI	34.6145	118.7235	718
CI	RCT	36.3052	119.2438	107
CI	RPV	33.7435	118.4041	107
CI	SDD	33.5526	117.6617	120
CI	SHO	35.8995	116.2753	451
CI	SLA	35.8910	117.2833	1174
CI	SMM	35.3142	119.9958	599
CI	SVD	34.1065	117.0982	605
CI	SWS	32.9408	115.7958	140
CI	TIN	37.0542	118.2301	1197
CI	TOV	34.1561	118.8204	298
CI	TUQ	35.4358	115.9239	1350
CI	USC	34.0192	118.2863	58
CI	VES	35.8409	119.0847	154
CI	WER	35.0605	119.0271	130
II	PFO	33.6092	116.4553	1280
IU	ANMO	34.9459	106.4572	1754
IU	TUC	32.3096	110.7846	873
LB	DAC	36.2770	117.5937	1813
TA	109C	32.8889	117.1051	150
TA	T06C	37.0069	119.7089	216

TA	Y12C	33.7503	114.5238	196
TA	Y22C	34.0741	106.9211	1436
US	AMTX	34.8837	101.6808	1010
US	LTX	29.3339	103.6669	1013
US	MNTX	31.6985	105.3821	405

Table A.0.1: Stations used in this study

Curriculum vitae

Jan 1, 1974	Born in Ningxia, China
1992-1997	BSc in Geophysics, Geophysics Department, Peking University, Beijing, China
1997-2000	MSc in Geophysics, Institute of Geophysics, China Earthquake Administration, Beijing, China
2000-2004	Research Assistant, Engineering Seismology and Urban Earthquake Disaster Mitigation Division, Institute of Geophysics, China Earthquake Administration (CEA). Beijing, China.
2004-2008	PhD student at Utrecht University, Utrecht, The Netherlands